AIRBORNE RADAR FOR HIGH-RESOLUTION MAPPING OF INTERNAL LAYERS IN GLACIAL ICE TO ESTIMATE ACCUMULATION RATE

by

Pannirselvam Kanagaratnam

B.S.E.E., University of Kansas, 1993

M.S.E.E. (With Honors), University of Kansas, 1995

Submitted to the Department of Electrical Engineering and Computer Science and the Faculty of the Graduate School of The University of Kansas in partial fulfillment of the requirements for the degree of Doctor of Philosophy.

Dissertation Committee:

_____

Sivaprasad Gogineni: Chairperson

_____

Christopher Allen

_____

Swapan Chakrabarti

_____

James Stiles

_____

David Braaten

Date Defended: February 27, 2002

To my Gurus

ACKNOWLEDGEMENTS

I am deeply indebted to my mentor, Dr. Sivaprasad Gogineni, for giving me the opportunity to pursue a Ph.D. degree in electrical engineering. When I first started my undergraduate study I did not even dream about pursuing graduate school, let alone a doctorate. Because of his encouragement I was inspired to pursue a doctoral degree. He not only looks after his students' academic needs but also their well being outside of the classroom.

I would like to thank Dr. Chris Allen, Dr. James Stiles, Dr. Swapan Chakrabarti and Dr. David Braaten for serving on my committee. I would like to thank Dr. Robert Thomas, Dr. Ken Jezek and Dr. Waleed Abdalati for their help and encouragement during the course of my research. I am also grateful to Mr. William Krabill, Mr. Doug Young and the rest of the support crew at the NASA flight facility at Wallops Island for all of their help.

I am grateful to Mr. Niels Gundestrup and Mr. Lars Larsen for the enormous support they provided during our surface-based experiments at the North Greenland Ice core Camp (NGRIP). I would like to thank Dr. Justin Legarsky, Dr. Carl Leuschen and Mr. Shane Haas for helping to conduct experiments at NGRIP Also I am grateful to Sverrir Hilmarrson for the antenna mounts and to Björk Hardarsdottir for going out of her way to prepare vegetarian meals for me.

TABLE OF CONTENTS

vi

LIST OF FIGURES

LIST OF TABLES

ABSTRACT

Global climate change is currently a major environmental and political issue. The rise in sea level has been strongly correlated with global climate change. Now there is considerable uncertainty in the present-day and future roles played by polar ice sheets in sea level rise. An accurate determination of the mass balance of polar ice sheets is essential to quantify their role in sea level rise. Snow accumulation rate is an important parameter in mass balance computation of polar ice sheets. Currently this is determined by dating ice cores and analyzing stratigraphy of snow pits. Retrieving and analyzing ice cores and digging snow pits are, however, time-consuming, expensive and tedious. In addition, the sparse sampling of ice cores and snow pits has resulted in uncertainty of about 24% in the accumulation rate maps. This dissertation explores the possibility of conducting high-resolution mapping of near-surface isochronous layers in the ice sheet with aircraft radar to estimate long-term accumulation rate.

Our approach to the development of an operational airborne radar system was five fold. We first obtained the physical and electrical properties of an ice core and modeled it using the transmission line method. We performed a simple electromagnetic simulation to determine the optimum radar parameters for a ground-based system. Second, we developed an ultra-wideband Frequency-Modulated-Continuous-Wave (FM-CW) radar to operate over the frequency range from 170 to 2000 MHz. We tested the radar at the North Greenland Ice Core Project (NGRIP)

camp and successfully mapped the internal layers for the top 300 m of the ice sheet. We analyzed the frequency response of the internal reflections from these measurements to determine the optimum frequency of operation for an airborne radar system. Third, we used surface- and volume-scattering models to determine the effects of clutter on the return from internal layers. Our modeling results indicated that we should be able to detect the near-surface inter-annual layers from an aircraft. We then developed a 600-900 MHz prototype airborne radar system and tested it over the Greenland ice sheet. Our results show that it is indeed possible to map the internal layers with high resolution from an aircraft. Finally, we addressed the problems associated with the prototype system and used a CAD tool to optimize the radar performance. We also developed a target simulator to test and calibrate the radar. The system is now ready for routine measurement of internal layers over the polar ice sheets.

Chapter 1

INTRODUCTION

1.1 Why Study Glacial Ice?

The rise of sea level has been proposed as a significant indicator of global climate change [Etkins and Epstein, 1982]. Over the last century sea levels rose by about 15 cm. The Intergovernmental Panel of Climate Change (IPCC) [2001] has projected a sea level rise of 5 mm/yr over the next 100 years. This magnitude of sea level rise would lead to a host of devastating problems such as dislocation of people in coastal regions, coastal erosion, loss of land and property, increased risk of storm surges, increased vulnerability of coastal ecosystems, saltwater intrusion into freshwater resources, and high costs associated with adapting and responding to these changes [IPCC, 2001]. The Institute of Electrical and Electronic Engineers recently examined nine critical challenges facing the engineering community. One of the challenges is the use of technology to anticipate and mitigate the effects of climate change [Perry, 2002].

About 50% of the current sea level rise is attributed to thermal expansion of the ocean and the melt of mountain glaciers [Dyurgerov and Meier, 1997]. The increase in glacier melting has, in turn, been positively correlated with the increase in land-surface temperature, especially in the Northern Hemisphere [IPCC, 2001]. There is considerable uncertainty about the present and future roles played by polar ice

sheets in the rise of sea levels. An accurate determination of their role is essential to quantify present and future contributions of polar ice sheets to sea level rise [Thomas, 1991; van der Veen, 2002].

To assess the role of the Antarctic and Greenland ice sheets in sea level rise, an improved knowledge of the mass balance of these ice sheets is required. There are two methods to determine the mass balance of an ice sheet [Patterson, 1998]. The first is the flux method in which a comparison is made between the (net) long-term average input (net accumulation) and the output (ice flow) fluxes. The second is the volumetric method in which changes in surface elevation are measured. For the flux method, ice velocities, ice thickness, surface temperature and topography, ablation measurements, and an accurate knowledge of the accumulation rate are needed. For the volumetric method, inter-annual variability of snowfall is needed to interpret results. [van der Veen and Bolzan, 1999; McConnell et al., 2001; Davis et al., 2000].

1.2 Raison d'etre for Remote Mapping of Internal Layers

Accumulation information is currently determined from ice cores and pits [Patterson, 1998]. For the Greenland ice sheet, Ohmura and Reeh [1991] generated an accumulation map using data on 251 pits and cores and precipitation measurements from 35 meteorological stations located in coastal regions. The accuracy of this map is a function of the spatial location of the data points. Ohmura and Reeh [1991] also reported that an inherent accumulation rate uncertainty of 20% in their map was due to the inconsistency between meteorologically determined precipitation and

glaciologically determined accumulation. In addition, more than 75 different cores from 50 distinct locations were obtained in the NASA PARCA (Program for Arctic Regional Climate Assessment) program. Information from these cores was used to generate an updated map of accumulation over the Greenland ice sheet. Bales et al. [2001a, 2001b] report that the uncertainty in accumulation is in the order of 24% at certain areas. Figure 1.1 shows the kriging variance in the current accumulation map. The black spots on the map indicate the locations of the ice cores that were used to create the accumulation map. The darker shades on the map indicate greater uncertainty in the accumulation rate estimates. We can clearly see a correlation between the core locations and the uncertainty in the map. Areas with a large number of ice core samples have lower uncertainty in the accumulation rate estimates. Figure 1.2 shows the elevation change measured with a laser altimeter [Krabill et al., 2000]. The altimeter measurements indicate rapid thinning in areas close to the coast, especially in the southwest region. The accumulation rate estimates in this region are, however, highly uncertain due to the sparse sampling of ice cores here. To accurately interpret the results we need a more accurate estimate of the accumulation rate. A long-term history of the accumulation rate will indicate to us whether this is a recent phenomenon or a historically high-melt area. Collecting icecores in this area is, however, a daunting task since there are many deep crevasses in this region. The only practical method of obtaining an accumulation profile in this region is by remote sensing.
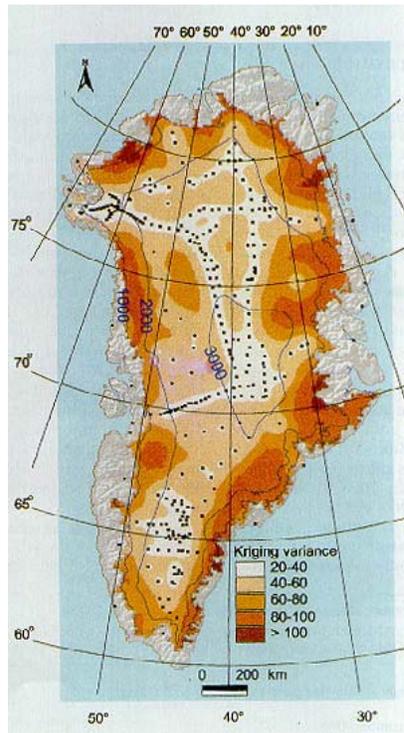
Figure 1.1. Uncertainty in accumulation rate [Bales et al., 2001a].
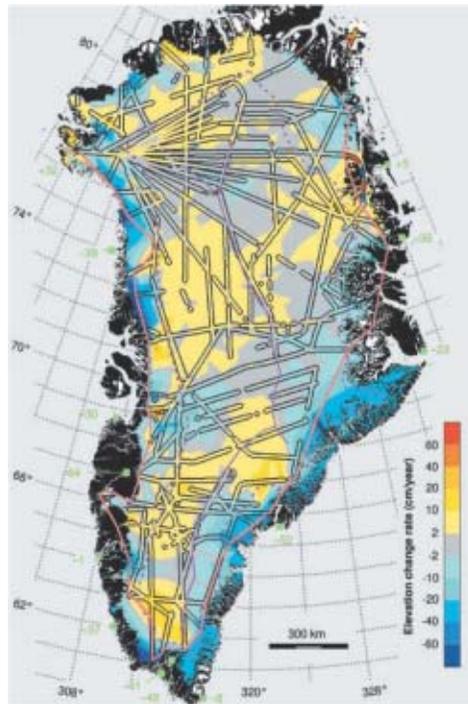
Figure 1.2. Change in elevation [Krabill et al., 2000].

4

Furthermore, the ice cores provide only point estimates. They do not account for local variations that are known to occur within short distances. Figure 1.3 illustrates this point. Note how undulations are overlooked when the sampling is too far apart.
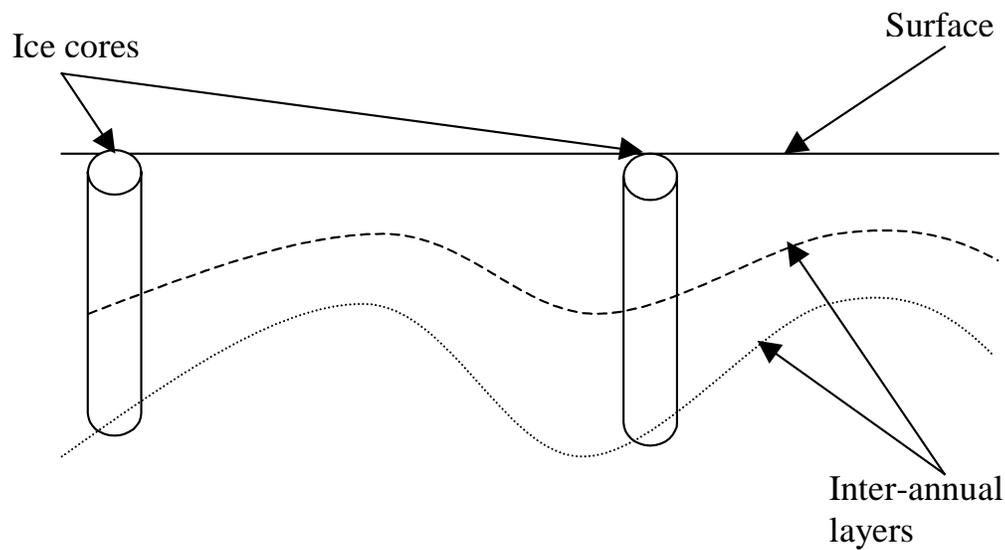
Figure 1.3. Limitation of ice cores in sampling local variability in snow distribution.

To provide improved spatial and temporal coverage, the development of remote sensing methods to estimate the accumulation rate is required. An accurate estimate of the long-term accumulation rate can be obtained by mapping a continuous profile of the dated layers in the ice sheet. The dated layers here refer to inter-annual layers, volcanic and melt events. Annual accumulation and melt events register a change in the density, whereas volcanic events are marked by a change in conductivity [Hammer, 1980]. Reflection profiles from ice-sounding radar systems

show many internal ice reflections between the bedrock and the surface. The internal layers observed over the first few hundred meters have been attributed to density contrast between annual layers [Robin, et al., 1969; Paren & Robin, 1975], whereas the reflections from deeper layers where there is no discernable density contrast are attributed to changes in conductivity and crystal orientation [Hammer, 1980; Millar, 1981; Fujita et al., 2000]. By mapping shallow internal layers, we will be able to identify the inter-annual layers and melt and volcanic events; this information, combined with published data on density and thickness, can be used to estimate the accumulation rate over periods of time. We can also reduce the errors due to local variability and study the effect of such local variability by collecting data from the near-surface layers over distances greater than several ice thicknesses.

There are several types of airborne radar systems that can measure the thickness of the ice sheet. To the best of my knowledge, however, there is no airborne system capable of achieving less than 1 m vertical resolution to 100 m depth. This is needed to map the near-surface internal layers for accumulation estimation.

1.3 Objective and Approach

The primary objective of this project is to develop an airborne radar system to map the internal layers in the Greenland ice sheet with a resolution of 1 m up to a depth of 100 m. This corresponds to snow accumulations over the past 200 to 500 years, depending on location.

To determine optimum radar parameters, we performed simulations on an electromagnetic model of the ice sheet. The electrical conductivity measurements of ice cores and the published real value of permittivity were used to model the electrical properties of the ice sheet. An electronic design automation software, EEsof® [Agilent Technologies], was then used to model the ice sheet using the Transmission Line Method [Cheng, 1989]. A simple simulation was then performed to determine the optimum radar parameters by simulating the scattering response of the ice sheet due to radar sounding. We then developed an ultra-wideband Frequency-Modulated-Continuous-Wave (FM-CW) [Saunders, 1990; Stove, 1992] radar system to operate over a frequency range of 170 to 2000 MHz to image the top 200 to 300 m of ice with a high vertical resolution of about 0.5 m. Using this system we performed shallow radar-sounding experiments at the North Greenland Ice core Project (NGRIP) site (75.1^o N, 42.3^o W) during June and July of 1998, and in August of 1999. We collected data over a 2-km and a 10-km traverse with the radar mounted on a tracked vehicle. We successfully mapped the internal layers to within $\pm$ 2 m of that in an ice core for the top 300 m of the ice sheet.

We analyzed the frequency response of the internal reflections from surface-based measurements to determine the optimum frequency of operation for an airborne radar system. Based on this analysis, and, taking into account the frequencies used for communication on the aircraft, we developed a 600-900 MHz airborne prototype. We tested this system during the May 2001 field season over the Greenland ice sheet. The results from this experiment prove that it is indeed, possible to map the internal layers

remotely from an aircraft with a resolution of 1 m or better for the top 150 m of the firn. The problems encountered with the system during the May 2001 field season were identified to develop an improved system.

We developed an improved radar for routine measurements starting in the 2002 field season. We used EEsof® to optimize the system performance before construction. We designed a Gaussian high-pass filter with fast settling time to minimize ringing in the Intermediate Frequency (IF) section. We constructed boxes to shield the transmit, receive and IF sections adequately. The front end of the transmitter and receiver were placed in a second box close to the bomb bay to shorten the path length between the two. This served to push the antenna feed-through signal further into the stop band of the high-pass filter. In addition, we developed a target simulator using Radio Frequency (RF)/optical transceivers and fiber optic delay lines to optimize radar performance further. It simulates a signal coupled between the transmit and receive antenna, strong reflection from air-snow interface and reflections from internal layers that are spaced 50 cm apart. The target simulator is a useful tool for laboratory characterization of the system. This is because it is difficult to test the system outdoors due to interference from wireless communication devices that operate in our frequency band of interest.

1.4 Organization

This dissertation is divided into 8 chapters. Chapter 2 presents a brief history of glacial ice sounding and previous shallow snow sounding systems. Chapter 3

describes an electromagnetic model of the ice sheet model. The use of the transmission line method to model the layers in the ice sheet is discussed in this section. Chapter 4 describes the application of surface and volume scattering models to compute the signal-to-clutter ratio and hence, to determine the possibility of detecting internal layers from an aircraft. Chapter 5 describes the radar system developed for the surface-based experiments at NGRIP and their results. The optimum frequency for airborne operation is determined from these experiments. Uncertainty in the accumulation rate computation is also presented in this section. Chapter 6 describes the design and development of an airborne radar system and the results of the field experiment. Chapter 7 provides details of further improvements in the radar system for future airborne missions. Chapter 8 concludes this dissertation with a summary and recommendations.

Chapter 2

BACKGROUND

Efforts to study the physical properties of snow using microwave techniques began as early as the 1950s [Saxton, 1950; Cumming, 1952]. Theoretical developments of radar methods in glaciology began with the express purpose of measuring the thickness of glacial ice in 1955 [Bogorodsky et al., 1983]. The capability of a Radar Echo Sounder (RES) in measuring ice thickness was first demonstrated experimentally by Amory Waite in 1957, when he observed a return from the bottom of the Ross Ice Shelf in Antarctica [Waite, 1959]. Since then, there has been a rapid development of radar systems to map the thickness of ice sheets. A short discussion on the evolution of RES can be found in Gogineni et al. [1998].

A brief summary of previous research on characterizing internal layers with RES systems is given here. A more detailed discussion can be found in Robin [1983]. The detection of internal layers in glacial ice by RES was first reported by Bailey, Evans and Robin [1964]. A number of researchers have since written papers on the phenomena of layer reflections from within the ice sheet [Robin, et al., 1970; Harrison, 1973; Gudmansen, 1975]. Researchers attributed the reflections from the first few hundred meters to density contrast between depositional layers [Robin, et al., 1969; Paren and Robin, 1975]. However, internal layering was also observed at depths where the density difference is believed to be non-existent. Paren and Robin

[1975] suggested that changes in conductivity between layers could be contributing to reflections from deeper depths. The conductivity was attributed to impurities in the snowfall. However, Hammer (1977) showed that the impurities in the ice sheet are due to acidity from major volcanic eruptions. A thorough discussion of the nature of dielectric discontinuities in glacial ice and their implications to ice sounding can be found in [Fujita et al., 2000]. Internally reflecting layers at large depths provide a measure of the deformation undergone by the ice sheets and reveal information about the ice flow dynamics.

Concerted efforts to sound the stratigraphy of snowpack began in the 1970s. In 1972, Vickers and Rose [1972] made high-resolution measurement of snowpack using a short-pulse radar to measure the thickness, density and stratigraphy. A FM-CW system was used by Ellerbruch and Boyne [1980] to correlate radar signature with density, hardness, stratigraphy and moisture content of the snowpack. These parameters were then used to determine the water equivalence of the snowpack. Sounding of shallow snow layers in the polar ice sheets to measure accumulation rate was performed in 1982 by a Russian team [Bogorodsky et al., 1982; Lebedev et al., 1990]. An X-band radar was developed at the University of Kansas in 1990 to demonstrate that a less expensive and simpler FM-CW radar system could be used to map the inter-annual layers [Forster et al., 1991]. Since then, a number of systems have been developed to map the near-surface internal layer in the polar icesheet. Table 1 summarizes some of the systems that have been used to map the thickness of annual snow accumulation. However all these systems are ground based and do not

provide the coverage that is required by scientists to interpolate the variation in layer

thickness between ice cores. The research reported in this dissertation is aimed at

developing an airborne radar system to obtain wide-area coverage.

Table 1. Surface-based radar systems to map near-surface internal layers.

Year	Radar Type	Operating Frequency (GHz)	Resolution in free space (cm)	Max. Depth (m)	Reference
1982	Pulse	10	15	11.5	Bogorodsky, et al., 1982 Lebedev, et al., 1990
1990	FM-CW	10-12	7.5	6	Forster, et al., 1991
1993	Step-Frequency	0.8-2.3	10	11.5	Richardson, et al., 1997
1996	Impulse	0.5	25	10	Kohler, et al. 1997
1998	FM-CW	0.17-2	8.2	300	Kanagaratnam, et al., 2001

Chapter 3

ELECTROMAGNETIC PROPERTIES OF ICE SHEET

3.1 Introduction

The internal layers seen in a radar echogram of an ice sheet are due to the reflections from dielectric discontinuities within the ice. In this chapter, a brief review of physical properties of firn that influence dielectric characteristics is provided. Use of a transmission line method of modeling radar response is discussed and simulation results obtained with a transmission line model of the ice sheet are presented.

3.2 Theory

A transmitted radar signal will reflect from the interfaces between layers of differing permittivity. For a monochromatic wave, the reflection coefficient for a three-layer media, Γ, at the firn-air interface of an embedded layer is given by [Paren and Robin, 1975]:

$$\Gamma = \frac{\sqrt{\varepsilon_{r2}} - \sqrt{\varepsilon_{r1}}}{\sqrt{\varepsilon_{r2}} + \sqrt{\varepsilon_{r1}}} 2 \sin\left(\frac{2\pi l}{\lambda_m}\right) \tag{3.1}$$

where ε_{r1} is the complex permittivity of layer 1 and layer 3, ε_{r2} is the complex permittivity of layer 2, l is the thickness of layer 2 and λ_m is the wavelength in layer 2. The magnitude of the reflection coefficient increases as the dielectric contrast

increases, but it is modulated by a sinusoidal term related to layer thickness and wavelength. The maximum value of the reflection coefficient occurs whenever layer thickness is an odd integer multiple of $\lambda_m/4$. The complex permittivity of the ice sheet is a function of crystal orientation fabrics, density, impurities (acidity concentration), and temperature [Fujita et al., 2000]. For the near-surface layer mapping, the three factors that influence reflected signals are density, impurities and temperature.

3.3 Density

Density changes are caused by melt events that normally occur in the percolation zone. The formation of a high-density melt layer occurs when a layer of snow or near-surface firn melts during the summer and the drainage forms a layer that subsequently refreezes. In between the winter and summer seasons a new layer of snow accumulates over the melt layer. Hence, the melt layer is sandwiched between two layers of low-density snow or firn. Density changes seen in the dry snow zone are primarily due to the pressure exerted by accumulation of snow above a layer. Depth hoar layers are also found in the dry snow region. Depth hoar layers are formed by large crystals due to sublimation and subsequent deposition of water vapor. Although depth hoar layers cause more abrupt change in density, their spatial continuity across spatial scales greater > 100 m is unknown [Forster et al., 1999]. The real part of the complex permittivity of firn, which consists of a mixture of air and ice, has been described by Looyenga [1965] using the following equation:

$$\varepsilon_r = \left[\left(\varepsilon_2^{1/3} - \varepsilon_1^{1/3}\right)v + \varepsilon_1^{1/3}\right]^3 \tag{3.2}$$

14

where ε_2 is the dielectric constant of ice (i.e., 3.15), ε_1 is the dielectric constant of air (i.e., 1), and v is the volume fraction of ice in the firn given by:

$$v = \rho_s / \rho_i \qquad (3.3)$$

where ρ_s is the density of the firn and ρ_i is the density of pure ice (i.e., 918 kg/m^3).

The reflection coefficient due to changes in the density can be computed by substituting the permittivity computed in (3.2) into (3.1). The real part of the complex permittivity does not vary as a function of frequency and has negligible temperature dependence for temperatures less than -2.5°C [Fujita et al., 2000].

3.4 Conductivity

Variations in conductivity have also been shown to be sources of internal reflections [Hammer, 1980; Fujita and Mae, 1994]. These variations are due to the acidic impurities embedded in the ice during volcanic eruptions. We derive below the reflection coefficient due to a change in conductivity.

The permittivity of the background and acidic layer can be expressed as:

$$\varepsilon_{r1} = \varepsilon'_{r1} - j\varepsilon''_{r1} \qquad (3.4)$$

$$\varepsilon_{r2} = \varepsilon'_{r2} - j\varepsilon''_{r2} \qquad (3.5)$$

where ε_{r1} is the dielectric constant of the background and ε_{r2} is the dielectric constant of the acidic layer.

Let us assume that $\dfrac{\varepsilon_r^{''}}{\varepsilon_r^{'}} \ll 1$ and $\varepsilon_{r1}^{'} = \varepsilon_{r2}^{'}$

The square-root of (3.5) is:

$$\sqrt{\varepsilon_{r2}} = \sqrt{\varepsilon_{r2}^{'} - j\varepsilon_{r2}^{''}} \tag{3.6}$$

Using the above assumptions allows us to expand (3.6) using the Taylor series expansion:

$$\sqrt{\varepsilon_{r2}} \approx \sqrt{\varepsilon_{r2}^{'}} - \dfrac{j\varepsilon_{r2}^{''}}{2\sqrt{\varepsilon_{r2}^{'}}} \tag{3.7}$$

Similarly,

$$\sqrt{\varepsilon_{r1}} \approx \sqrt{\varepsilon_{r1}^{'}} - \dfrac{j\varepsilon_{r1}^{''}}{2\sqrt{\varepsilon_{r1}^{'}}} \tag{3.8}$$

Equation 3.1 can then be simplified to:

$$\Gamma \approx \left| \dfrac{\left(\varepsilon_{r1}^{''} - \varepsilon_{r2}^{''} \right)}{4\varepsilon_{r2}^{'}} \right| \exp\left(j\dfrac{\pi}{2} \right) 2\sin\left(\dfrac{2\pi d}{\lambda_m} \right) \tag{3.9}$$

The equation above shows that the reflection coefficient due to a conductive change can be approximated with an imaginary quantity. However, Fujita et al. [2000] have shown that the phase delay of the reflection coefficient drops below $\pi/2$ with increasing frequency for temperatures above the eutectic point of the acid. Thus,

16

there is a contribution from the real part of the dielectric constant as well for temperatures above the eutectic point. The contribution to the real part of the reflection coefficient is probably due to the presence of liquid associated with impurities in the volcanic layer [Fujita et al., 2000] that may be present at temperatures above -40° C.

3.5 Crystal Orientation Fabrics

Discontinuities in the crystal orientation fabric are due to shear strain along the isochrones. Robin and Millar [1982] suggest that acidic impurities in the ice may change the mechanical properties in ice and thus cause an easy glide plane and, hence, a different fabric from its enclosing layers. The discontinuity in the orientation of the crystal fabric is quantified by the dielectric anisotropy of ice, which is the difference between permittivity parallel, $\varepsilon_{\|c}$, and perpendicular, $\varepsilon_{\perp c}$, to the c-axis, which is perpendicular to the basal plane of the ice crystal. Figure 3.1 shows the ice crystal structure. The circles in the figure are H_2O molecules. The hexagonal plane refers to the basal plane and the direction perpendicular to this plane is the c-axis.
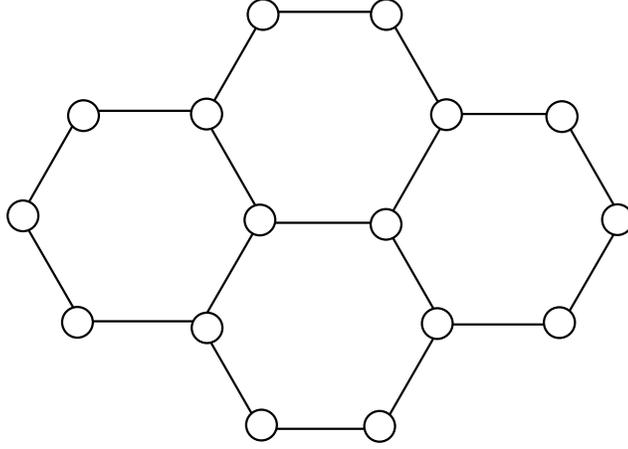
Figure 3.1. Structure of an ice crystal.

The dielectric anisotropy, $\Delta\varepsilon^{'}$, was found to be [Fujita and Mae, 1994]:

$$\Delta\varepsilon^{'} = 0.037 \pm 0.007 \tag{3.10}$$

The dielectric permittivity tensor of polycrystalline ice was given as [Fujita and Mae, 1994]:

$$\varepsilon^{'} = \varepsilon^{'}_{\perp c} + \Delta\varepsilon' \, D_a \tag{3.11}$$

where D_a is a factor which accounts for the contribution of $\Delta\varepsilon^{'}$ to the dielectric permittivity tensor and is given as

$$D_a = \frac{1}{N}\sum_{j=1}^{N}\cos\theta_j \tag{3.12}$$

where N is the number of crystal grains and θ_j is the angle between the c-axis of the jth grain and the incident wave. The orientations of the crystals are measured using

18

optical techniques, a description of which can be found in Paterson [1998]. The reflection coefficient due to changes in the crystal orientation fabric is expressed as:

$$\Gamma = \left| \frac{\Delta\varepsilon^{'}\delta D_a}{4\varepsilon^{'}} \right| 2\sin\left(\frac{2\pi l}{\lambda_m}\right) \tag{3.13}$$

The amplitude of the reflection coefficient caused by changes in the crystal orientation fabric is independent of ice temperature and frequency [Fujita et al., 2000]. Reflections due to changes in the crystal orientation fabric have only been found at depths where there are no density changes. In the analyses that are to follow, the orientations of the crystal fabrics will not be considered as we are currently interested in the near-surface reflections only.

3.6 Transmission Line Method

The density and conductivity data of an ice core can be used to model the ice sheet using the transmission line method. The wave characteristics on a transmission line are analogous to uniform plane waves in lossy media. The propagation of a plane wave through a medium is given by:

$$E(z) = E_o \exp(-\gamma z) \tag{3.14}$$

where E_o is the field strength of the transmitted signal, $E(z)$ is the field strength at distance z into the media, γ is the propagation constant given by:

$$\gamma = \alpha + j\beta = j\omega\sqrt{\mu_o \varepsilon_c} \tag{3.15}$$

19

where α is the attenuation constant (Np/m), β is the phase constant (rad/m), ω is the frequency of the signal, μ_o is the permeability constant in free space, ε_o is the permittivity constant in free space and ε_c is the complex permittivity of the media in which the wave is propagating. The complex permittivity, ε_c, is given by:

$$\begin{aligned} \varepsilon_c &= \varepsilon' - j\varepsilon'' \\ &= \varepsilon_o \varepsilon_r - j\frac{\sigma}{\varpi} \end{aligned}$$

(3.16)

where ε' is the lossless part of the complex permittivity, ε_r is the relative permittivity, ε'' is the dielectric loss of the media, and σ is the conductivity.

The relationships between the physical parameters, density and electrical conductivity, measured from the ice cores and the complex permittivity have been approximated by equations. The relationship between the density and the permittivity has been described by (3.2).

The conductivity of the ice sheet is determined using the dielectric profiling (DEP) method [Moore and Paren, 1987]. The DEP system is used to measure the capacitance and the conductance of ice. The capacitance of the ice determines the relative permittivity of the ice whereas the conductance determines the imaginary part of the ice. The conductivity is determined by the following equation [Gross et al., 1980]:

$$\sigma_{firn} = \frac{\varepsilon_o G_{ice}}{C_{air}}$$

(3.17)

where G_{ice} is the measured conductance of the firn and C_{air} is the measured capacitance without the firn. The conductivity thus computed is substituted in (3.16) to determine the imaginary part of the permittivity.

Several ice cores have been collected at the GRIP and NGRIP sites. The density and conductivity for some of these ice cores have been determined. We can divide these ice cores into layers of length h m and determine the impedance of each layer from the complex permittivity profile of the ice core. In an electromagnetic simulation this will be analogous to cascading transmission lines of length h and characteristic impedances corresponding to the layers' impedance. A similar procedure was described by Moore [1988]. The relationship between the impedance and the complex permittivity is given as:

$$Z = \frac{j\mu_o\varpi}{\gamma} \tag{3.18}$$

$$Z = \sqrt{\frac{\mu_o}{\varepsilon_o\left(\varepsilon^{'} - j\varepsilon^{''}\right)}} \tag{3.19}$$

The transmission line model of the ice core can be used in an electromagnetic simulator to observe the effects of changes in complex permittivity on the incident wave. The concept will be illustrated using Agilent EEsof®'s Advanced Design Systems (ADS) simulator [2001]. EEsof® is a powerful electromagnetic simulator that has many features that will enable the radar designer to optimize the design before construction. Some of the salient features of EEsof® are:

21

1) Seamless interface with test equipment. This feature allows the designer to measure the S-Parameter of components using a network analyzer and use them for simulations.

2) Integrated test environment. Circuits and system models can be easily interfaced for simulations. The medium of propagation can be modeled using the transmission line elements. The system and propagation models can thus be combined and simulated to determine the radar response to a particular medium.

Figure 3.2 shows the transmission line model available in EEsof® to define the complex permittivity of layers in the ice sheet.

TLINP
TL1
Z=35.0 Ohm
L=10 meter
K=2
F=fsc
TanD=2.64e-4
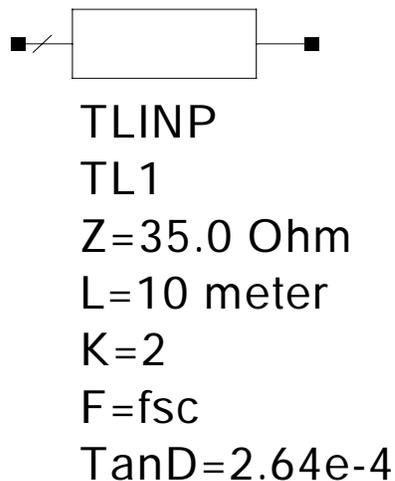
Figure 3.2. Transmission line model in EEsof®.

The various parameters of the transmission line shown above are described herein. Z is the characteristic impedance of the transmission line. EEsof® will allow

22

one to specify only the real part of the impedance for the characteristic impedance, Z. The imaginary part of the impedance will be factored in the TanD parameter. The characteristic impedance will govern the reflection due to changes in the real part of the complex permittivity. In our simulations, the characteristic impedances were normalized with respect to a 50Ω system and not with the conventional 377Ω system in free space. This was done to match the radar system's components that were included in the overall simulation. In practice, the 50Ω system was matched to the free space impedance of 377Ω with a horn antenna. The parameter, L, defines the layer thickness. K is the effective dielectric constant. The effective dielectric constant reduces the free space velocity of waves in a particular layer by a factor of its square root; i.e. $\sqrt{K}$. It does not influence the computation of the reflection coefficient. The parameter, F, is the frequency at which the loss tangent parameter, TanD, is computed. The loss tangent is given as:

$$\text{TanD} = \frac{\varepsilon^{''}}{\varepsilon^{'}} = \frac{\sigma}{\varepsilon^{'} \varepsilon_{o} \varpi} \tag{3.20}$$

The loss tangent governs the dielectric loss of the propagating wave in ice. This parameter will allow us to model the changes in the imaginary part of the ice sheet and observe its effect on the incident wave. A simple four-layer model is presented first to illustrate the concept (Figure 3.3).

23

The first layer is 500 m of free space to simulate the height of the aircraft above the ice sheet. The free space was modeled using a time delay of 1.67 μs. The second and fourth layers form the ice sheet. A relative permittivity of 2 and a conductivity of 17 μS/m were assumed for these layers. The third layer, a volcanic ash layer embedded in the ice sheet, was modeled as a layer with a relative permittivity of 2 and a conductivity of 40 μS/m at 10 m below the air-firn interface. The relative permittivity values as well as the conductivity values were substituted in (3.19) and (3.20) to compute the real part of the impedance and the loss tangent. A S-parameter simulation was performed from 600 MHz to 900 MHz in steps of 187.5 kHz. This measurement is analogous to a step-frequency radar measurement using a vector network analyzer whereby the inverse Fourier Transform (IFT) of the S_{11} measurement will yield the reflection profile.

Figure 3.4 shows the result of this simulation. The first reflection is about –15 dBm, which is the expected level for the given impedance mismatch. The second reflection is about –79 dBm. It was also observed that the pulse width of the second reflection is about 1.4 times the pulse width of the first reflection. The loss of resolution is due to the greater attenuation of the high-frequency components as the wave propagates through the lossy media.
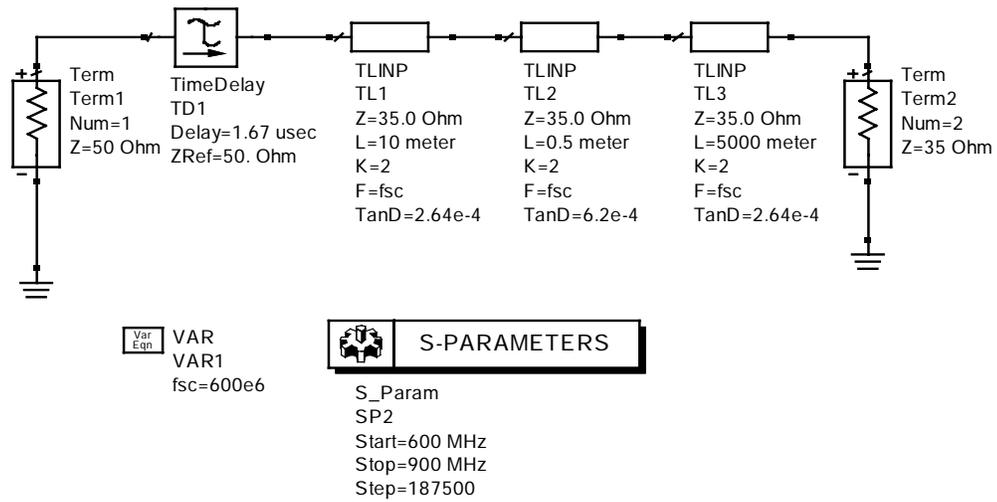
Figure 3.3. Setup on EEsof® to simulate pulse response to layered media.
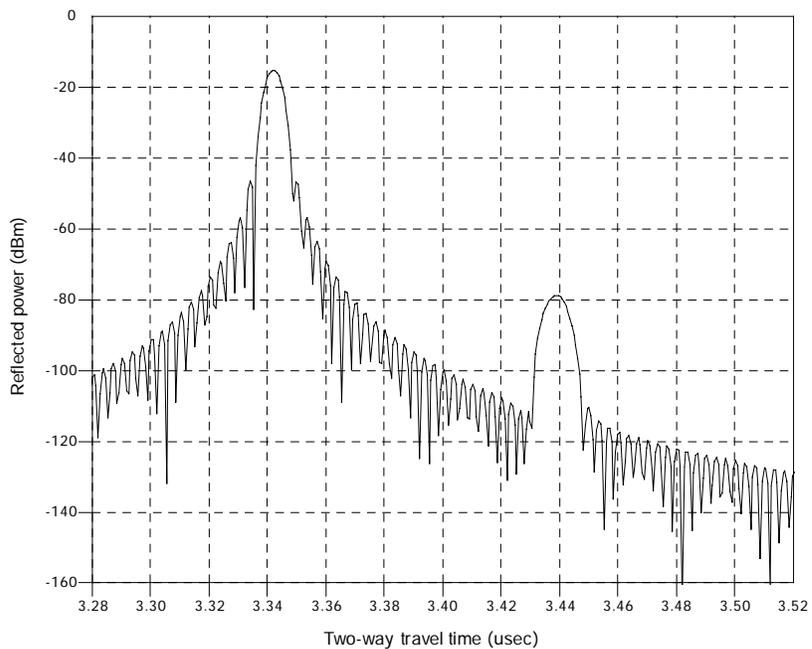
Figure 3.4. Reflection profile of EEsof® simulation. The pulse width of the second reflection is about 1.4 times the reflection from the first interface.

3.7 Summary

In this chapter we provided a brief review of the physical properties of firn and showed how these physical properties can be used to construct an electromagnetic model for simulating radar response using a CAD package. These simulations are useful for studying the trade-off of radar characteristics when mapping near-surface layers.

Chapter 4

SURFACE AND VOLUME CLUTTER

4.1 Introduction

Because of the finite beamwidth, reflections from internal layers may be masked by off-nadir backscatter from the surface and volume scatter. A long antenna can be synthesized by taking advantage of the forward aircraft motion to reduce beamwidth in the along-track direction. It is possible to install a large-array antenna to obtain narrow beamwidth in the cross-track direction under the wing of a P-3 aircraft. However, the hardpoints needed to install such an antenna are used for the coherent radar depth sounder. Because the wideband accumulation radar antennas have to be installed in the limited space available in the bomb bay of P-3 aircraft, we used a TEM horn with an aperture of 1 meter with beamwidth of 45 degrees. In this chapter, limitations resulting from off-nadir surface and volume clutter are investigated.

4.2 Problem

The off-nadir clutter may mask some of the reflections from deeper layers as illustrated in Figure 4.1. The effect of clutter on the received signal will be examined in this section.
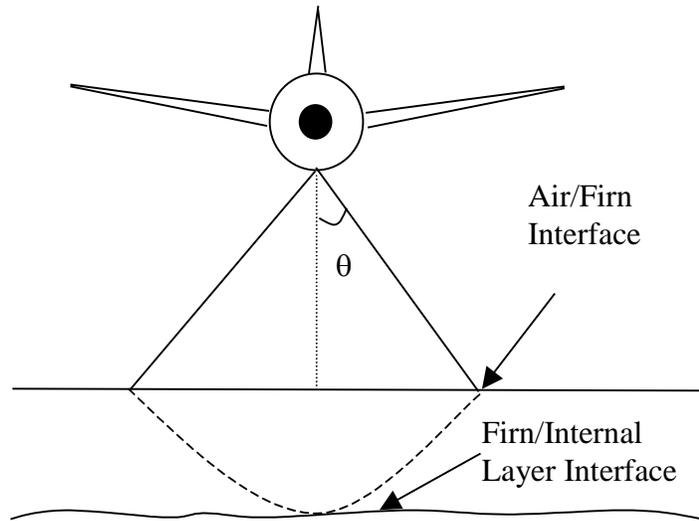
Figure 4.1. Clutter problem in airborne systems. Off-angle surface clutter may mask
reflections from deeper layers.

The return power, S, from a perfectly flat surface is given as:

$$S = \frac{P_t \lambda^2 G^2 \Gamma^2}{(4\pi)^2 (2R)^2} \qquad (4.1)$$

where P_t is the transmitted power, λ is the wavelength, G is the antenna gain, Γ is the

reflection coefficient at the air/snow interface or between two internal layers and R is

the range to the interface.

The above equation can be used to approximate the received power from the

internal layers. The internal layers can be successfully detected only if their reflected

power is higher than that due to surface and volume scattering from the firn. The

return power, C, from a distributed target is given as

$$C = \frac{P_t \lambda^2 G^2 \sigma^o A}{(4\pi)^3 R^4} \qquad (4.2)$$

where A is the illuminated area and σ^o is the backscattering coefficient of the incident medium. To obtain signal-to-clutter ratio greater than one, the following inequality needs to be satisfied:

$$S > C \qquad (4.3)$$

$$\frac{P_t \lambda^2 G^2 \Gamma^2}{(4\pi)^2 (2R)^2} > \frac{P_t \lambda^2 G^2 \sigma^o A}{(4\pi)^3 R^4} \qquad (4.4)$$

$$\Gamma^2 > \frac{\sigma^o A}{\pi R^2} \qquad (4.5)$$

The following sections will be devoted to the computation of the illuminated area and the backscattering coefficient due to surface and volume scattering. This will determine if the above inequality is satisfied for the dry snow region of the Greenland ice sheet.

4.3 Area of Illumination

The horn antennas that are to be used in our experiments have beamwidths of 45° at 600 MHz and 30° at 900 MHz. The footprints covered by these beamwidths are much larger than those due to the range resolution of the radar system. Therefore, the illuminated area has to be computed for the pulse-limited case. The shaded areas in Figure 4.2 and Figure 4.3 show the illuminated area for the pulse-limited case [Ridley

and Partington, 1988]. Figure 4.2 illustrates the illuminated area of the first range cell. The illuminated areas for subsequent range cells are rings, as shown in Figure 4.3. The diameter of the circle in Figure 4.2 is computed as follows:

$$\left(\frac{d_1}{2}\right)^2 = \left(H + \Delta R\right)^2 - H^2 \qquad (4.6)$$

$$d_1 = 2\sqrt{\left(H + \Delta R\right)^2 - H^2} \qquad (4.7)$$

The illuminated area is thus:

$$Aill_1 = \pi\left(\frac{d_1}{2}\right)^2 \qquad (4.8)$$
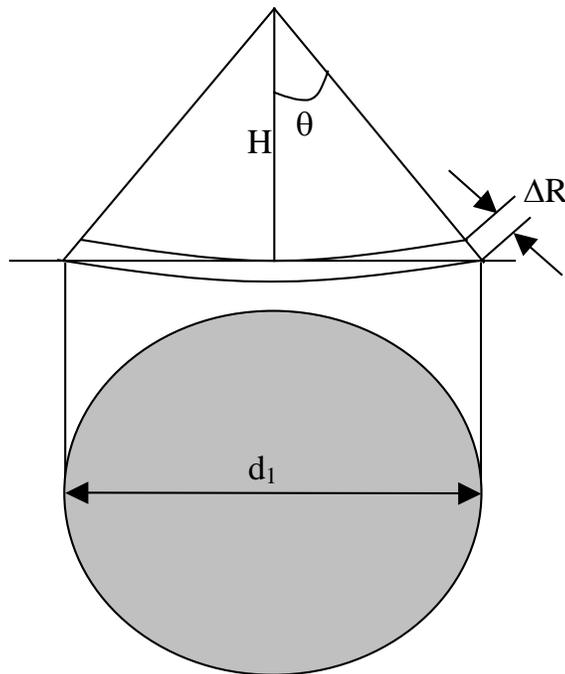
Figure 4.2. Illuminated area of first range cell.

The width of the first ring, r_2, in Figure 4.3 is computed as follows:

$$\left(\frac{d_1}{2} + r_2\right)^2 = (H + 2\Delta R)^2 - H^2 \tag{4.9}$$

$$r_2 = \sqrt{(H + 2\Delta R)^2 - H^2} - \frac{d_1}{2} \tag{4.10}$$

The area of the ring is computed as follows:

$$Aill_2 = \pi\left(\frac{d_1}{2} + r_2\right)^2 - Aill_1 \tag{4.11}$$

Subsequent rings can be computed in a similar fashion until the summation of the diameter of the circle and ring widths is equal to the diameter due to the beamwidth of the antenna, d_{BW}; i.e.,

$$d_1 + 2r_2 + 2r_3 + \ldots + 2r_n = d_{BW} \tag{4.12}$$

where
$$d_{BW} = 2H\tan(BW) \tag{4.13}$$

The horn antennas placed at a height of 500 m with a beamwidth of 45° would yield a diameter of 1000 m.
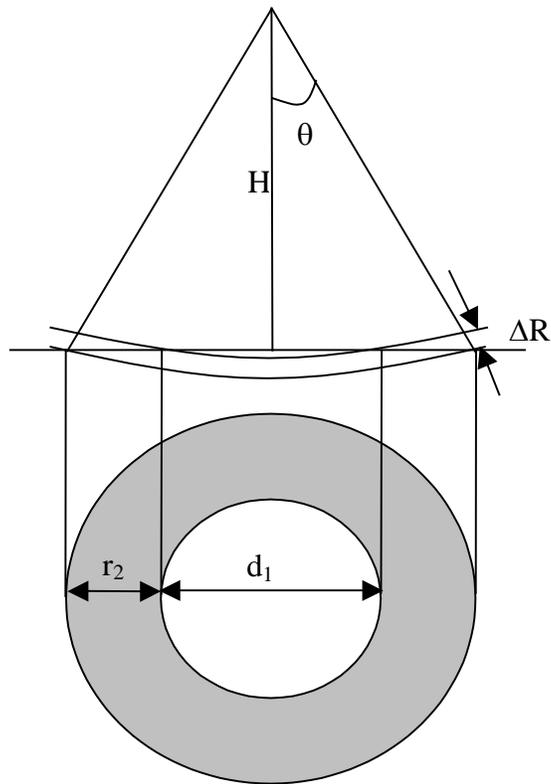
Figure 4.3. Illuminated area of second range cell.

4.4 Surface Scattering

Figure 4.4 below illustrates the nature of surface scattering. When an electromagnetic wave impinges on the boundary layer between two media of differing permittivity, a portion of this wave's energy is reflected and the rest is transmitted into the second medium. The reflection of an electromagnetic wave from a smooth surface is called the specular or coherent component and the direction of reflection is called the specular direction. As the roughness of the surface increases, the reflection in the specular direction begins to decrease as the incident wave's energy is redistributed in

other directions. These scattered components are called the incoherent components. Theoretically, a monostatic radar should not be able to receive the return power from a smooth surface at incidence angles other than nadir. The primary component seen at incidence angles greater than zero is the incoherent component, whose magnitude is typically larger when the surface is rougher. However, incoherent components may also be observed at nadir if the antenna beamwidth is large. These incoherent components may fall at later range bins and mask the weaker coherent components from subsequent interfaces. The roughness of a surface seen by the radar is dependent on the wavelength. The smaller the wavelength, the rougher the surface seen by the radar.
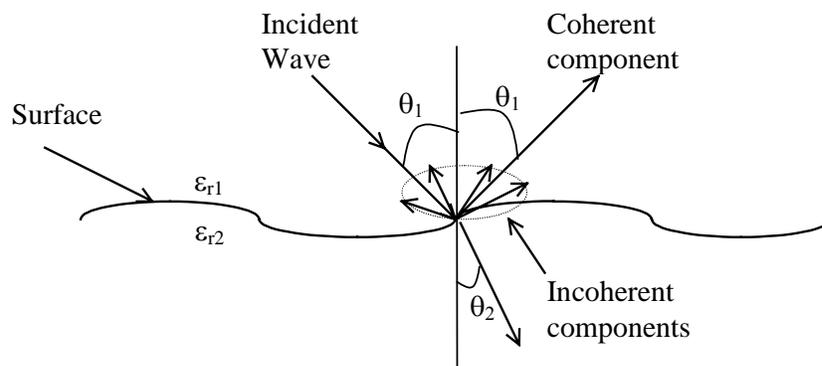
Figure 4.4. Nature of surface scattering.

4.4.1 Coherent Scattering

The specular reflection from a small rms (root-mean-square) surface roughness superimposed on a smooth surface is given as [Fung and Eom, 1983; Fetterer et al., 1992]:

$$\sigma_{\text{coh}}^{\text{o}} = \frac{|\Gamma(\theta)|^2}{\beta^2} \exp\left(-4k^2\sigma^2 - \frac{\theta^2}{\beta^2}\right) \tag{4.14}$$

where Γ is the Fresnel reflection coefficient, β is the one-sided pulse-limited beam width, k is the wavenumber and σ is the rms height of the surface. The one-sided pulse-limited beam width is equivalent to θ in Figure 4.2. As such, we can determine β as follows:

$$\begin{aligned}
\tan(\beta) &= \frac{d_1}{2H} \\
&= \frac{\sqrt{(H + \Delta R)^2 - H^2}}{h} \\
&= \frac{\sqrt{H^2 + 2\Delta RH + \Delta R^2 - H^2}}{h} \\
&= \frac{\sqrt{2\Delta RH + \Delta R^2}}{H}
\end{aligned} \tag{4.15}$$

Since $H \gg \Delta R$, the above equation reduces to:

$$\begin{aligned}
\tan(\beta) &\approx \frac{\sqrt{2\Delta RH}}{H} \\
&\approx \sqrt{\frac{2\Delta R}{H}}
\end{aligned} \tag{4.16}$$

For small angles, $\tan(\beta) \approx \beta$, thus:

$$\beta^2 \approx \frac{2\Delta R}{H} \tag{4.17}$$

Substituting (4.17) into (4.14), we obtain:

34

$$\sigma_{coh}^{o} = \frac{|\Gamma(\theta)|^2 \, H}{2\Delta R} \exp\left(-4k^2\sigma^2 - \frac{\theta^2 H}{2\Delta R} \right)$$
(4.18)

The following parameters, obtained from the dry snow region [Long and Drinkwater, 1994], were used to compute the backscatter using the model described above: σ=6.1 mm and ε_r=1.6. Figure 4.5 shows the coherent backscattering coefficient. The backscattering coefficients were plotted as a function of equivalent range to simplify comparison with expected reflections from internal layers. The equivalent range is related to the incidence angle, θ_1, as follows:

$$R = \frac{H}{\cos(\theta_1)}$$
(4.19)

where H is the height of the antenna above the incident plane. The NASA P-3 aircraft flies about 500 m above the surface and we used this height to compute the equivalent range. The figure shows a rapid falloff of the coherent component with increasing range (incidence angle). In the next section, the result of this computation will be combined with the effects of incoherent scattering and compared to the specular reflection from the internal layers.
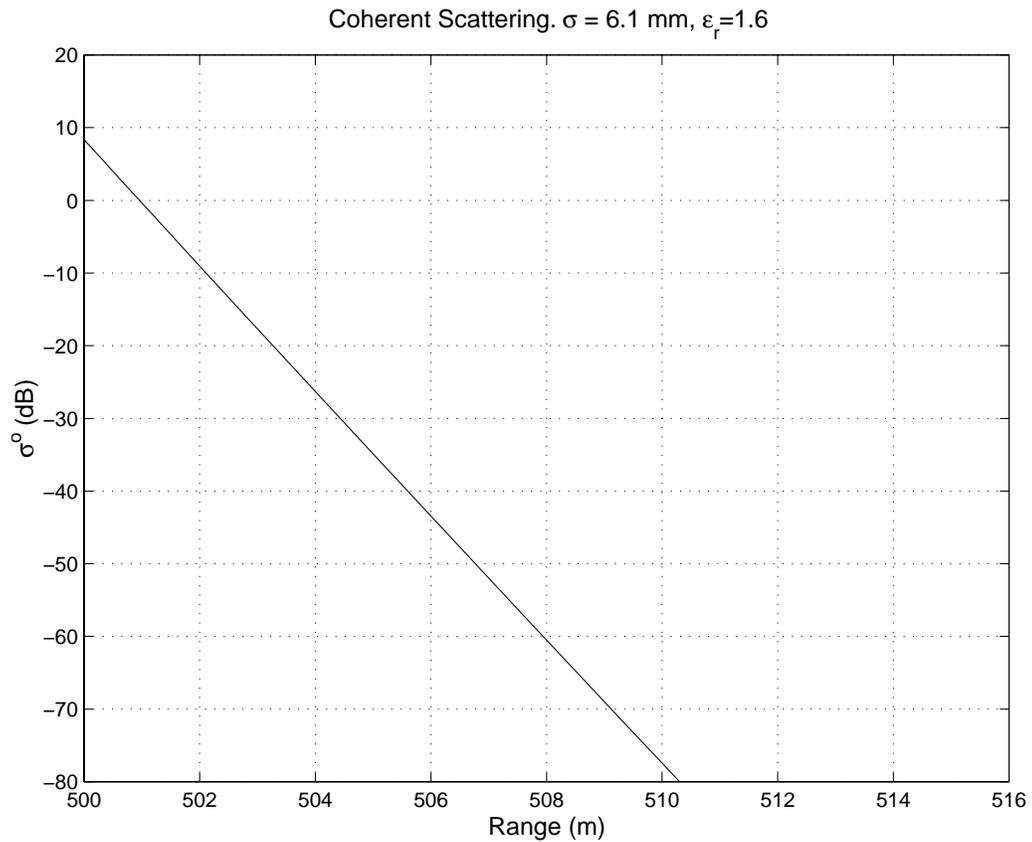
Figure 4.5. Coherent backscattering versus equivalent range to surface.

4.4.2 Incoherent Scattering

The Integral Equation Method (IEM) [Fung, A.K., 1994] was developed to model the backscatter due to surface roughness. This model will be used to compute the backscatter due to surface roughness in the dry snow region of the Greenland ice sheet. A special case of the IEM was derived for surfaces of small and medium roughness. For surfaces with a Gaussian correlation function, the required condition was given as:

$$(\text{k}\sigma)(\text{kL}) < 1.2\sqrt{\varepsilon_r} \tag{4.20}$$

where k is the wave number ($2\pi/\lambda$), σ is the rms height, L is the correlation length and ε_r is the relative permittivity of the incident surface. A rms height of 6.1 mm and correlation length of 9 cm are typical roughness parameters of the dry snow region in Greenland [Long and Drinkwater, 1994]. The permittivity of the surface is given as 1.6. The highest frequency of our radar system is 900 MHz. Substituting these parameters into (4.20) yields 0.1951 for the left side and 1.52 for the right side. The inequality is thus satisfied and we can proceed to use the modified IEM, which is given as:

$$\sigma^o_{pp} = \frac{\text{k}^2}{2} \exp\left(-2\text{k}_z^2\sigma^2\right) \sum_{n=1}^{\infty} |\text{I}^n_{pp}|^2 \frac{\text{W}^{(n)}(-2\text{k}_x,0)}{n!} \tag{4.21}$$

where $\text{k}_z=\text{k}\cos\theta_1$, $\text{k}_x=\text{k}\sin\theta_1$, θ_1 is the incidence angle, and pp = vv or hh polarization,

$$\text{I}^n_{pp} = (2\text{k}_z\sigma)^n \text{f}_{pp} \exp\left(-\text{k}_z^2\sigma^2\right) + \frac{(\text{k}_z\sigma)^n\left[\text{F}_{pp}(-\text{k}_x,0)+\text{F}_{pp}(\text{k}_x,0)\right]}{2} \tag{4.22}$$

$$\text{f}_{vv} = \frac{2\text{R}_{\|}}{\cos\theta_1} \tag{4.23}$$

$$
\begin{aligned}
&\text{F}_{vv}(-\text{k}_x,0)+\text{F}_{vv}(\text{k}_x,0) \\
&= \frac{2\sin^2\theta_1\left(1+\Gamma_{\|}\right)^2}{\cos\theta_1}\left[\left(1-\frac{1}{\varepsilon_r}\right)+\frac{\mu_r\varepsilon_r-\sin^2\theta_1-\varepsilon_r\cos^2\theta_1}{\varepsilon_r^2\cos^2\theta_1}\right]
\end{aligned} \tag{4.24}
$$

where $\Gamma_\parallel$ is the Fresnel reflection coefficient for the vertically polarized case and is given as:

$$\Gamma_\parallel = \frac{\sqrt{\varepsilon_{r2}}\cos\theta_1 - \sqrt{\varepsilon_{r1}}\cos\theta_2}{\sqrt{\varepsilon_{r2}}\cos\theta_1 + \sqrt{\varepsilon_{r1}}\cos\theta_2} \qquad (4.25)$$

where ε_{r1} is the relative permittivity of the first medium and ε_{r2} is the relative permittivity of the second medium. The angles θ_1 and θ_2 are illustrated in Figure 4.4 and they satisfy Snell's law:

$$k_1\sin\theta_1 = k_2\sin\theta_2 \qquad (4.26)$$

where k_1 and k_2 are the wave numbers of media one and two, respectively.

The roughness spectrum corresponding to a Gaussian correlation is:

$$W(K) = \frac{L^2}{2}\exp\left[-\left(\frac{KL}{2}\right)^2\right] \qquad (4.27)$$

and the Fourier transform of the nth power of the correlation function is:

$$W^{(n)}(K) = \frac{L^2}{2n}\exp\left[-\frac{(KL)^2}{4n}\right] \qquad (4.28)$$

The following parameters were used to compute the backscatter using the IEM described above: $\sigma=6.1$ mm, L=9 cm, $\varepsilon_r=1.6$. Figure 4.6 shows the computed backscattering coefficient for frequencies ranging from 600 MHz to 900 MHz.
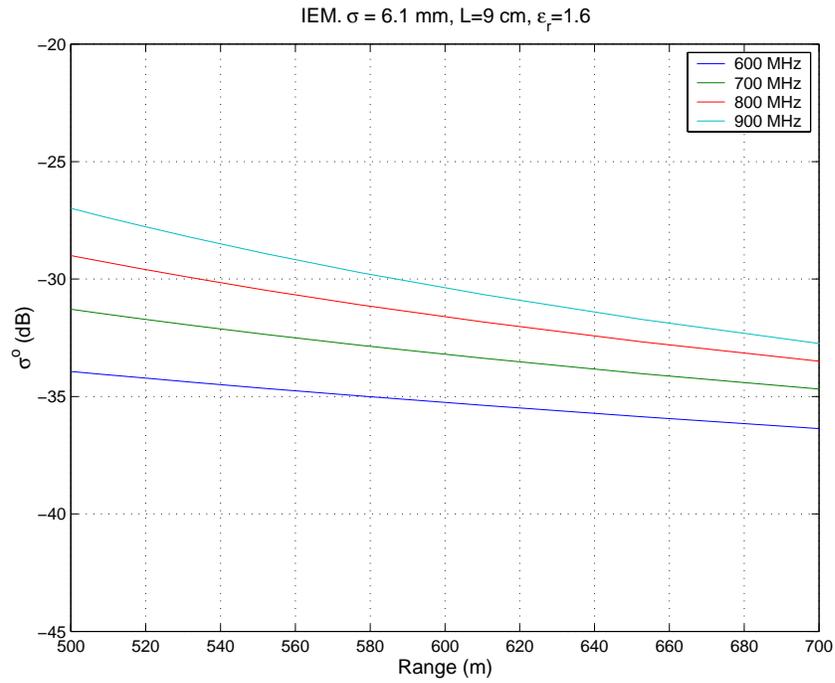
Figure 4.6. Backscattering coefficient due to surface roughness.

The coherent backscattering coefficient and incoherent backscattering at 600 MHz and 900 MHz were summed and substituted into (4.5) for comparison with the power reflection coefficient computed from the ice core at NGRIP. Figure 4.7 and Figure 4.8 show that the specular reflection beyond the first reflection is consistently higher than the surface clutter by about 10 to 15 dB and 5 to 10 dB for the first 50 m at 600 MHz and 900 MHz, respectively.
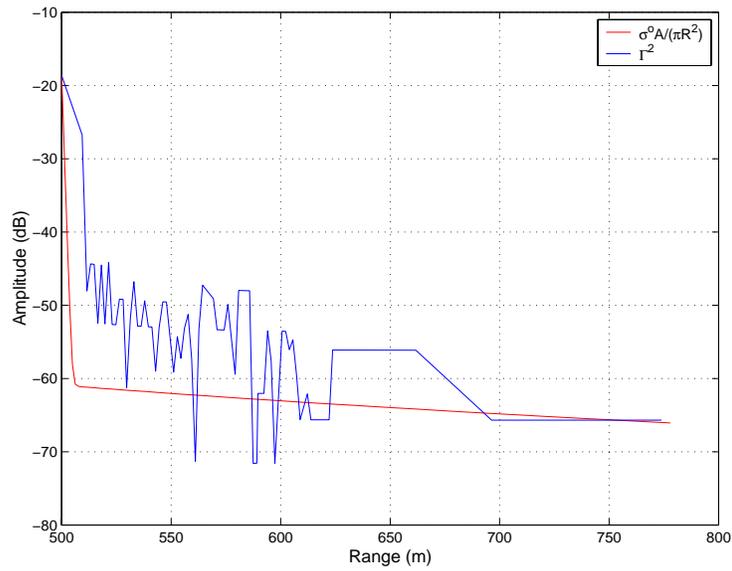
Figure 4.7. Comparison between reflection coefficient of internal layers and surface scattering. Frequency=600 MHz.
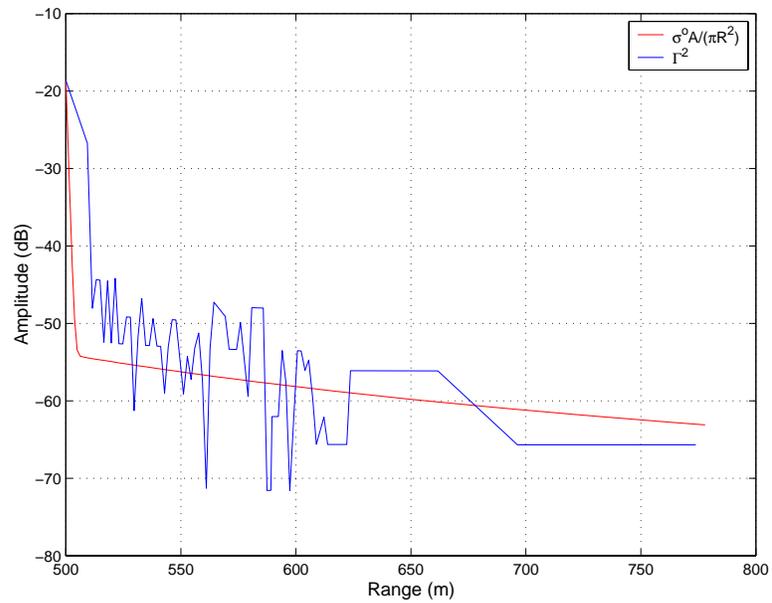
Figure 4.8. Comparison between reflection coefficient of internal layers and surface scattering. Frequency=900 MHz.

4.5 Volume Scattering
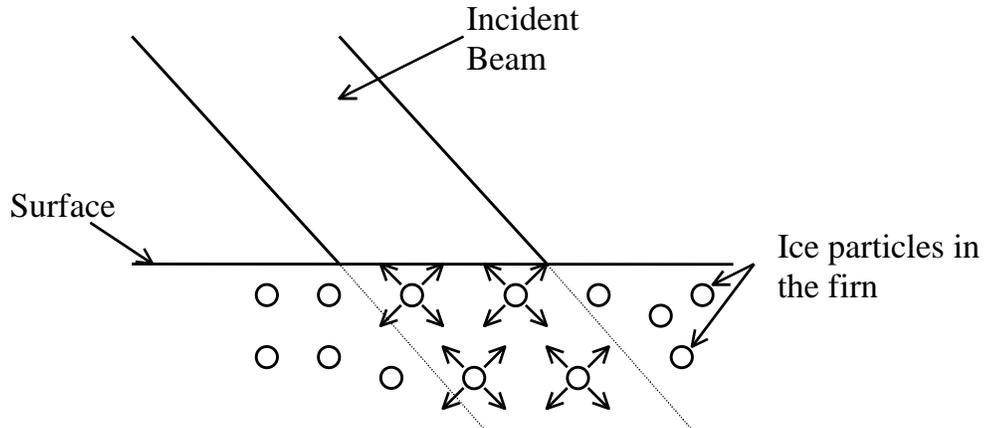
Figure 4.9. Typical scattering pattern from within the firn.

Figure 4.9 illustrates the nature of volume scattering wherein the ice particles in the firn scatter the incident wave. The magnitude of the scattered energy is highly dependent on the size of the ice particle relative to the wavelength of the incident signal. The smaller the wavelength of the transmitted signal, the more energy is scattered when incident upon an ice particle. The Rayleigh volume scattering model introduced by Ulaby et al. [1986] and adapted by Forester et al. [1999] for modeling the dry snow zone in Greenland will be used to determine the scattering from the firn. The backscatter for a single annual layer from the firn is given by:

$$\sigma_{layer}^{o} = \gamma^2(\theta_1)\left[\sigma_{ds}^{o}(\theta_2) + \frac{\sigma_{s}^{o}(\theta_2)}{L^2(\theta_2)}\right] \tag{4.29}$$

where γ is the transmitivity, θ is the incidence angle, σ_s^o is the surface backscatter from the interface between annual layers, and σ_{ds}^o is the normalized radar cross section from the dry snow volume given by:

$$\sigma_{ds}^o = \frac{N\sigma_b \cos(\theta')}{2\kappa_e}\left(1 - \frac{1}{L^2(\theta')}\right) \tag{4.30}$$

where N is the number of scatterers per volume, κ_e is the extinction coefficient, L is the one-way loss factor given by:

$$L^2(\theta') = \exp[\kappa_e h \sec(\theta')] \tag{4.31}$$

where h is the annual layer thickness, and σ_b is the backscattering cross section for a single snow grain given by:

$$\sigma_b = \frac{8}{3}\pi\kappa_b'^4 r_e^6 \left|\frac{\varepsilon_s - \varepsilon_b}{\varepsilon_s + 2\varepsilon_b}\right|^2 \tag{4.32}$$

where κ_b' is the wave number in the background medium (air), ε_s is the permittivity of the scatterer (ice), ε_b is the permittivity of the background (air), and r_e is the optically equivalent snow grain radius given by:

$$r_e = (1.2 + v - 2v^2)r \tag{4.33}$$

where r is the physical radius of the grain and v is the volume fraction of the ice, which is the ratio of the density of the firn, ρ_s, to the density of pure ice, ρ_i.

The extinction coefficient, κ_e, in (4.30) and (4.31) is the summation of both the volume absorption (κ_a) and scattering coefficients (κ_s); i.e.,

$$\kappa_e = \kappa_s + \kappa_a \tag{4.34}$$

The volume scattering coefficient is given as:

$$\kappa_s = NQ_s \tag{4.35}$$

where Q_s is the scattering cross section of the sphere of radius r, m^2. The scattering cross section is given as:

$$Q_s = \frac{2\lambda^2}{3\pi} \chi^6 \, | \, K \, |^2 \tag{4.36}$$

where χ is given as:

$$\chi = \frac{2\pi r}{\lambda_b} = \frac{2\pi r}{\lambda_o} \sqrt{\varepsilon_b} \tag{4.37}$$

and K is given as:

$$K = \frac{\varepsilon_s - \varepsilon_b}{\varepsilon_s + 2\varepsilon_b} \tag{4.38}$$

The number of scatterers per volume is computed as:

$$N = \frac{\rho_s}{\rho_i \left(\dfrac{4}{3} \pi r^3 \right)} \tag{4.39}$$

The volume absorption coefficient is given as:

$$\kappa_a = \kappa_{ai} + \kappa_{ab} \tag{4.40}$$

where κ_{ai} accounts for the absorption by the ice spheres whereas κ_{ab} accounts for the absorption by the background. κ_{ai} is given by:

$$\kappa_{ai} = NQ_a \tag{4.41}$$

where Q_a is the absorption cross section of the sphere of radius r, m^2. The absorption cross section is given as:

$$Q_a = \frac{\lambda^2}{\pi} \chi^3 \, \text{Im}\{-K\} \tag{4.42}$$

The absorption coefficient due to the background is given as:

$$\kappa_{ab} = 2k_o(1-v)\text{Im}\left\{\sqrt{\varepsilon_b}\right\} \tag{4.43}$$

where k_o is the wavenumber in free space.

The absorption coefficients are dependent on the imaginary component of the dielectric constant. In the dry snow region this is very small and hence we can neglect it for our computations. The absorption factor becomes significant only when one moves to the percolation and wet snow zones where the wetness increases the imaginary component of the dielectric constant.

The surface backscatter from the interface between the annual layers, σ_s^o, in (4.29) is assumed to be negligible since the surface characteristics for these layers [Long and Drinkwater, 1994] are smooth relative to the wavelengths in the 600 MHz to 900 MHz frequency range according to the Rayleigh criteria [Ulaby et al., 1986]. Equation 4.29 then reduces to:

$$\sigma_{layer}^o = \gamma^2(\theta)\sigma_{ds}^o(\theta')$$ (4.44)

The total backscatter from multiple annual-layers from the firn is given by:

$$\sigma_{firn}^o = \sum_{n=1}^{M}\frac{\gamma^2(\theta'_{n-1})\sigma_{ds_n}^o(\theta'_n)}{L_{(n-1)!}^2}$$ (4.45)

where n is the annual layer number, M is the last layer contributing to the total backscatter, θ'_n is the refracted angle in the nth annual layer for $n \geq 1$, and θ'_o is the look angle when n = 1.

The thickness of the annual layers is required to determine the loss through the medium. The depth of the annual layers for a region with a given accumulation rate were computed using the firn-densification model developed by Heron and Langway [1980]. They have showed that densification occurs in two distinct stages. The first stage occurs for densities less than 0.55 x 10^6 g m^{-3}. In this region the rate of densification is proportional to accumulation rate times the difference between the densities in this region and pure ice. The depth, h_1, for a given density in this region is given as:

45

$$h_1(\rho_s) = \frac{1}{\rho_i K_o} \left[\ln\left(\frac{\rho_s}{\rho_i - \rho_s}\right) - \ln\left(\frac{\rho_o}{\rho_i - \rho_o}\right) \right] \tag{4.46}$$

where ρ_o is the zero depth density, K_o is the rate constant and is given as:

$$K_o = 11\exp\left[-\frac{10,160}{GT}\right] \tag{4.47}$$

where G is the gas constant (8.314 $JK^{-1}mol^{-1}$) and T is the temperature in Kelvins. The age in years, t_1, for this depth is:

$$t_1(\rho_s) = \frac{1}{K_o A} \ln\left[\frac{\rho_i - \rho_o}{\rho_i - \rho_s}\right] \tag{4.48}$$

Thus we can solve for ρ_s for each annual layer and substitute the same in (4.46) to determine its depth.

The second stage of firn densification occurs at densities greater than 0.55×10^6 g m^{-3}. In this region the rate of densification differs from stage one in that it is now dependent on the square root of the accumulation rate. The depth corresponding to a given density in this region is:

$$h_2(\rho_s) = \frac{\sqrt{A}}{\rho_i K_1} \left[\ln\left(\frac{\rho_s}{\rho_i - \rho_s}\right) - \ln\left(\frac{0.55}{\rho_i - 0.55}\right) \right] + h_1(0.55) \tag{4.49}$$

where K_1 is the rate constant in this stage and is given as:

$$K_1 = 575\exp\left[-\frac{21,400}{GT}\right] \qquad (4.50)$$

The age of firn corresponding to densities at this depth is

$$t_2(\rho_s) = \frac{1}{K_1\sqrt{A}}\ln\left(\frac{\rho_i - 0.55}{\rho_i - \rho_s}\right) + t_1(0.55) \qquad (4.51)$$

The annual layer depth is determined in a similar fashion to that of stage one.
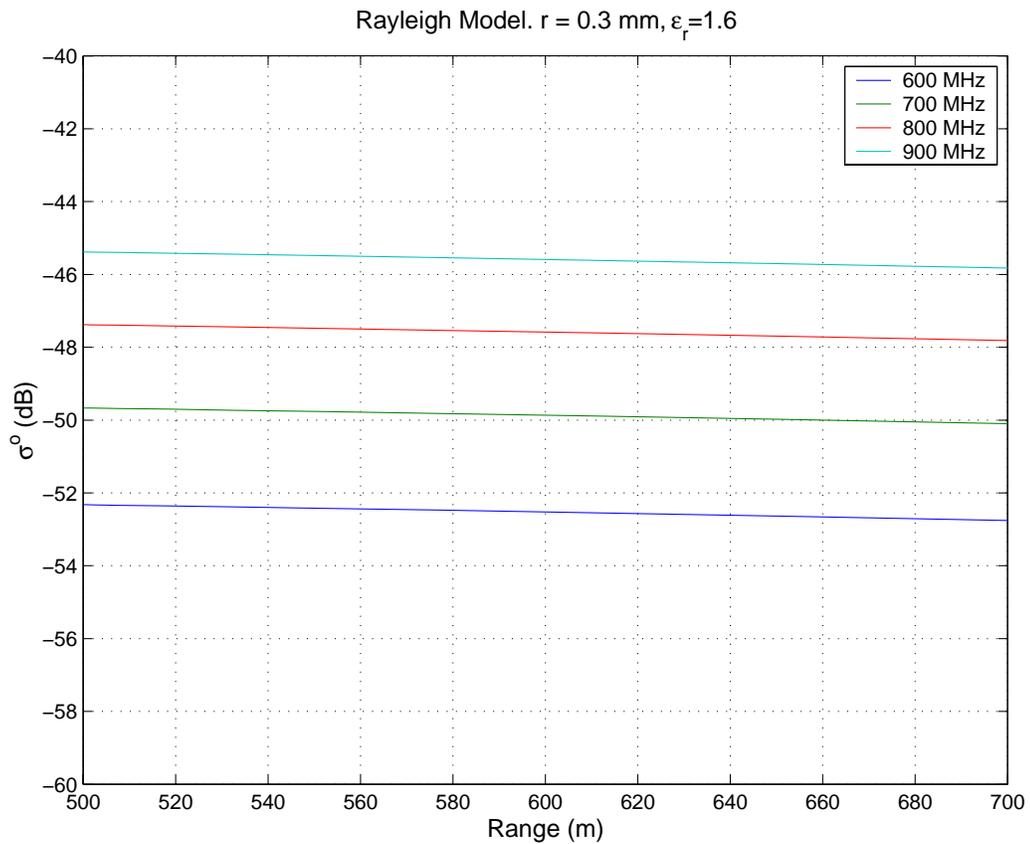
Figure 4.10. Backscattering coefficient due to snow grains.

The volume scattering contribution due to a snow grain size of 0.3 mm is shown above. The backscattering coefficient due to the snow volume is more than 15 dB below that due to surface scattering at 900 MHz. These simulations show that the volume scattering is negligible in computing the return power.

The modeling results indicate that only off-angle surface scattering has the potential of masking returns from internal layers in areas where the surface roughness is significantly larger. Rougher surfaces can be expected when one moves from the dry snow regions to the percolation and wet snow regions. However, the dielectric contrast between layers resulting from melt events is large, which compensates for increased backscatter.

4.6 Summary

In this chapter, we examined the effects of clutter, due to surface and volume scattering, on the return from internal layers. This is a problem particular to antennas with large beamwidth since they have the potential of masking the returns from the internal layers. We obtained the physical parameters of the ice sheet and computed the surface and volume scattering coefficients and compared them to the specular reflection due to density changes. Our results showed that the reflections from the internal layer were about 10 to 15 dB and 5 to 10 dB above the surface clutter at 600 MHz and 900 MHz, respectively. The volume scattering was 15 dB below that due to surface scattering and thus has little effect on the return from internal layers.

Chapter 5

SURFACE-BASED SYSTEM AND EXPERIMENTS

For high-resolution mapping of internal layers in the top 200 m of ice, we developed an ultra-wideband Frequency-Modulated-Continuous-Wave (FM-CW) radar system [Saunders, 1990; Stove, 1992] operating over the frequency range from 170 to 2000 MHz. Using this system we performed shallow radar-sounding experiments at the North Greenland Ice core Project (NGRIP) site (75.1^{o} N, 42.3^{o} W) during June and July of 1998, and in August of 1999. We used these experiments to demonstrate that near-surface internal layers can be mapped with high resolution and analyzed these data to determine optimum parameters for an airborne system.

This chapter presents the theory of FM-CW radar, the system description, experiments conducted at NGRIP, signal processing and the discussion of results and error analysis.

5.1 Theory of Linear FM-CW Radar

A simple FM-CW radar transmits a continuous waveform for which carrier frequency increases linearly with time. The modulation bandwidth, which determines range resolution, is the difference between the start and stop frequencies of the transmitted signal. In a FM-CW radar a sample of transmitted signal is mixed with the received signal to generate a beat signal. The frequency of transmit and received

signals will be different because of time delay, which is directly proportional to the range, associated with signal propagation to the target and back. The beat signal contains the range, amplitude and phase information of the target. Figure 5.1 shows a typical transmit and receive signals from a point target.
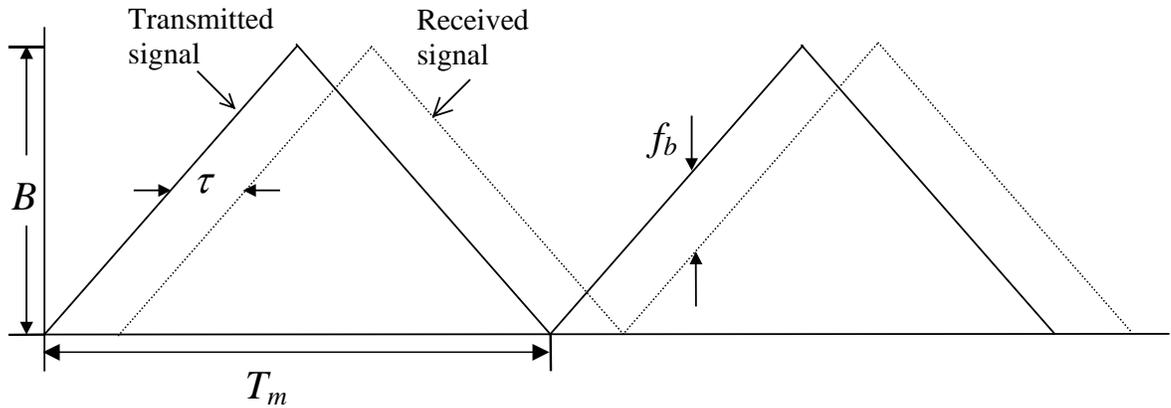
Figure 5.1. Transmit and receive signals from a point target for an FM-CW radar. B is the bandwidth of the signal, τ is the two-way travel time from the radar system to the target, T_m is the modulation period and f_b is the beat frequency.

The time, τ, for the signal to travel the two-way distance between the target and the radar is:

$$\tau = \frac{2R}{c} \tag{5.1}$$

where R is the range to the target and c is the velocity of light in free space. From the geometry of the transmit and receive waveforms a relationship can be derived between the beat frequency, f_b, and the range, R. For the triangular modulation the beat frequency is:

$$f_b = 2\tau B f_m$$
$$= \frac{4RBf_m}{c} \tag{5.2}$$

where f_m ($1/T_m$) is the modulation frequency.

For multiple targets, the beat signal will be a summation of several signals with frequencies proportional to their range. By Fourier transforming the beat signal to determine received signal frequencies, we can determine range to each target. The minimum separation between targets, τ_{min}, that can be seen by the radar is:

$$\tau_{min} = \frac{1}{B} \tag{5.3}$$

Substituting (5.3) into (5.1) gives the range resolution, ΔR, for the radar:

$$\Delta R = \frac{c}{2B} \tag{5.4}$$

In the derivation that follows, an expression for the beat signal will be determined. The transmitted signal voltage, $v_t(t)$, is given as:

$$v_t(t) = A\cos(2\pi f_o t + 2\pi B f_m t^2 + \theta_o) \tag{5.5}$$

where f_o is the initial sweep frequency, θ_o is the initial phase of the sweep source, and t is time. A portion of the transmitted signal is reflected back when it impinges on a dielectric interface. At the receive antenna, the reflected signal from a target located at range with time delay of t s can be expressed as:

$$v_r(t) = A^{'} \left| \Gamma[f(t)] \right| \cos \left\{ 2\pi f_o(t-\tau) + 2\pi B f_m(t-\tau)^2 + \theta_o + \phi[f(t)] \right\} \qquad (5.6)$$

where $|\Gamma[f(t)]|$ is the magnitude of the reflection coefficient at the dielectric interface and $\phi[f(t)]$ is the phase of the reflection coefficient. The reflection coefficient is a function of the transmit signal frequency, $f(t)$, which, as indicated, is a function of time.

The IF signal is obtained by mixing the received signal with a portion of the transmit signal and filtering out the higher-order terms. This process results in the following expression:

$$v_{IF}(t) = A^{'} \Gamma[f(t)] \cos \left\{ 2\pi f_o \tau + 2\pi B f_m (2\tau t - \tau^2) - \phi[f(t)] \right\} \qquad (5.7)$$

The above equation can be rewritten in terms of the beat frequency, f_b. Substituting (5.2) into (5.7) gives:

$$v_{IF}(t) = A^{'} \Gamma[f(t)] \cos \left\{ 2\pi f_b t + 2\pi f_o \tau - \pi f_b \tau - \phi[f(t)] \right\} \qquad (5.8)$$

The amplitude and phase of the target's reflection coefficient can be determined by means of the Hilbert Transform (HT) of the IF signal above. The HT of the IF signal will give us a complex signal in the following form:

$$v_{IF}(t) = A^{'} \Gamma[f(t)] \exp \left(j \left\{ 2\pi f_b t + 2\pi f_o \tau - \pi f_b \tau - \phi[f(t)] \right\} \right) \qquad (5.9)$$

We can obtain the phase response of the target by computing the phase term in (5.9), removing the range contribution in the phase term and then calibrating it with a

target of known phase. The amplitude response can be similarly obtained by computing the magnitude of the complex signal and calibrating it with a target of known amplitude.

5.2 System Description

The current section is divided into several sub-sections dealing with the specifications for the system, transmitter, receiver and IF sections of the radar system.

5.2.1 System Specifications

There are several parameters that need to be determined before deciding on the transmit power level and receiver gain. These parameters include the A/D dynamic range, noise figure of the system and the expected return power from the target.

The A/D that is available for our use is a 12-bit digitizer [Akins, 1999]. It is able to digitize signals with levels between –0.5 V and +0.5 V. The maximum signal-to-noise ratio (SNR) of an A/D converter is given as:

$$\text{SNR} = \frac{3Q^2}{2} \qquad\qquad (5.10)$$

where Q is the number of quantization levels. For a N-bit digitizer, the number of quantization levels is 2^N. Thus the maximum SNR for a 12-bit A/D is 74 dB. The maximum signal level that can be digitized with this A/D in a 50 Ω system is:

$$P_{max} = \frac{V_p^2}{2R} = \frac{0.5^2}{2 \times 50} = 0.0025\,\text{W} \approx 4\,\text{dBm} \tag{5.11}$$

The A/D noise floor is the difference between P_{max} and the SNR. Hence the noise floor of the A/D is –70 dBm.

The noise floor of the radar system, N, determines the minimum signal level that can be detected. This is given as:

$$N = kTBF \tag{5.12}$$

where k is the Boltzman constant (1.38 x 10^{-23} J/K), T is the room temperature (290 K), B is the bandwidth of a range bin in FM-CW radar systems and F is the noise figure of the receiver.

The bandwidth of a range bin is simply the sampling rate divided by the number of DFT (discrete Fourier transform) points before zero padding. The sampling rate for our ground-based system is 1 MHz and the number of DFT points is 57500. The bandwidth is thus 17.4 Hz.

The noise figure, F, is given by the Friis formula:

$$F = F_1 + \frac{F_2 - 1}{G_1} + \frac{F_3 - 1}{G_1 G_2} + ... = 1 + \sum_{i=1}^{n} \frac{(F_i - 1)}{\prod_{j=0}^{i-1} G_j} \tag{5.13}$$

The subscript of F denotes the component number subsequent to the receive antenna. G is the gain of the component. The table below lists the first three components of our radar system and their respective noise figures and gains.

Table 2. Gain and noise figure of components used in the front end of the receiver.

Component	Gain (dB)/(Linear)	F (dB)/(Linear)
1. Attenuator	-3 / 0.5	3 / 2
2. Amplifier	23 / 200	5.5 / 3.55
3. Attenuator	-3 / 0.5	3 / 2

Substituting the above values into (5.13) yields a noise figure of 8.5 dB. The minimum detectable signal from (5.12) is thus –153 dBm.

The simulations carried out in Chapter 3 on some typical parameters from the ice sheet show that the power reflected for the air/firn interface is about 15 dB below the transmit power of 0 dBm and for the volcanic layer embedded within the ice the reflected power is about -80 dBm at 600 MHz. Substituting these parameters into the radar equation in (4.1) we can compute the expected return power. Equation 4.1 can be rewritten in logarithmic form as:

$$S = P_t + 2\lambda + 2G + 10\log_{10}|\Gamma|^2 - 20\log_{10}(4\pi) - 20\log_{10}(2R) \qquad (5.14)$$

55

The above equation does not account for the scattering and absorption loss in the ice sheet. To get a better estimate of the reflected power we shall also include the losses due to scattering and absorption. The extinction coefficient given in (4.34) describes the loss through the medium. The two-way loss through the medium, α, is simply:

$$\alpha = \exp(-2R\kappa_e) \tag{5.15}$$

where R is the range to the target. Equation 5.14 then becomes

$$S = P_t + 2\lambda + 2G + 10\log_{10}|\Gamma|^2 - 20\log_{10}(4\pi) - 20\log_{10}(2R) - 20R\kappa_e\log_{10}(\exp(1)) \tag{5.16}$$

A grain size of 0.3 mm, which is the value reported by Forester et al. [1999] in the dry snow region, will be used for the computation of the scattering as well as absorption loss. We used a dielectric of 3.15-j0.001 for the dielectric constant of the snow particles. Figure 5.2 shows the attenuation through the ice sheet. The loss is mainly due to absorption. This is expected at these frequencies since the wavelengths are much larger than the particle size and, hence, a negligible amount of scattering loss is expected.

As explained in Chapter 3, the power reflection coefficient (PRC) for the volcanic layer will vary as a function of frequency, while the power reflection coefficient from the air/firn interface will remain constant. The constants that will be used in (5.14) are $P_t = 0$ dBm and $R = 2$ m for the air/firn interface and $R = 150$ m for the volcanic layer. The expected return power for these two interfaces at various

frequencies are tabulated in tables 3 and 4. Table 3 shows the expected return power from the air/firn interface and Table 4 shows the expected return power from the volcanic layer.
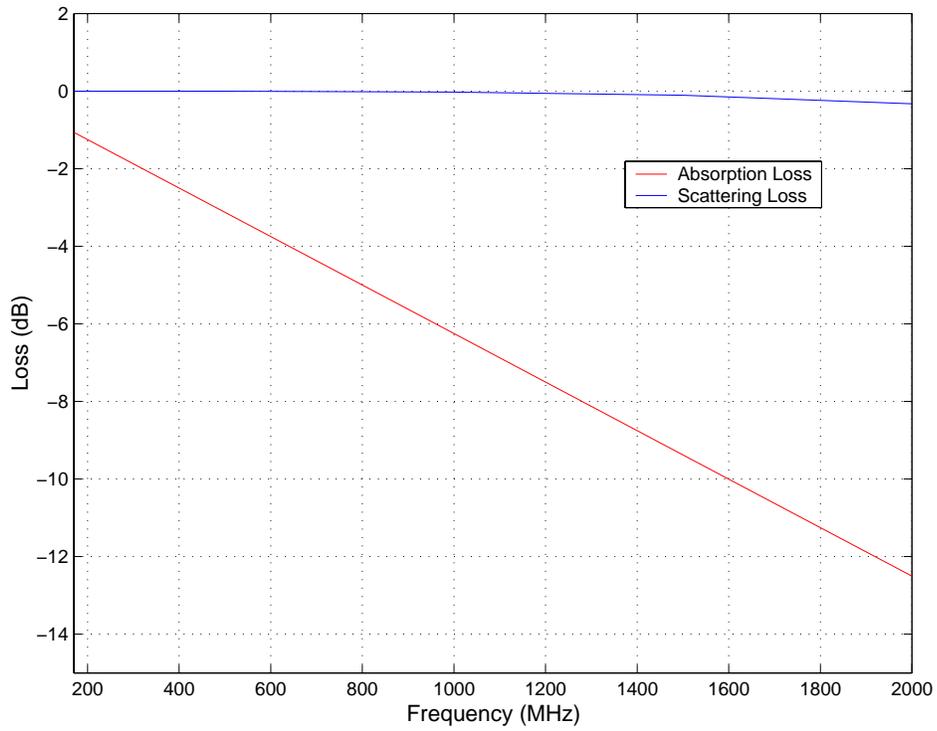
Figure 5.2. Propagation loss through the ice sheet for a distance of 150 m.

Table 3. Expected return from air/firn interface.

Frequency (MHz)	λ (cm)/(dB)	Gain (dB)	PRC (dB) (air/firn)	S (dBm)
170	176.5 / 2.5	-0.4	-15	-79
500	60 / -2.2	7.5	-15	-73
1000	30 / -5.2	7.0	-15	-80
1500	20 / -7.0	8.4	-15	-80.5
2000	15 / -8.2	3.0	-15	-94

Table 4. Expected return from volcanic layer.

Frequency (MHz)	λ (cm)/(dB)	Gain (dB)	PRC (dB) (volcanic layer)	α (dB)	S (dBm)
170	176.5 / 2.5	-0.4	-70	-1	-135
500	60 / -2.2	7.5	-79	-3	-140
1000	30 / -5.2	7.0	-85	-6	-156
1500	20 / -7.0	8.4	-89	-9	-163
2000	15 / -8.2	3.0	-92	-13	-183

The expected return power from the volcanic layer can be detected by our system for frequencies less than 1000 MHz if 0 dBm of power is transmitted. We chose an amplifier with 23 dBm of output power. The effective transmit power is 20 dBm since we had a 3 dB pad at the output of the amplifier. This output level should enable us to detect the volcanic layer for frequencies less than 1500 MHz. We did not

transmit additional power to detect the reflection at 2 GHz, since we felt it was not economical for our purposes; viz., to test the concept and determine the optimum frequency for airborne application. In airborne applications, we would need to transmit more power at 2 GHz to overcome the additional free-space loss, making the cost prohibitive.

Given the transmit power, A/D dynamic range and the noise figure of the system, we should now be able to derive the gain required in the receiver. We want the gain of the receiver such that there is greater than 10 dB signal-to-noise ratio at the A/D after coherent integration. In terms of an equation this translates to:

$$S + P_t + \text{Int. Gain} + G_{rcvr} > \text{A/D noise floor} + \text{SNR} \qquad (5.17)$$

$$-163 + 20 + 9 + G_{rcvr.} > -70+10$$

$$G_{rcvr.} > 74 \text{ dB}$$

We used a 23 dB gain amplifier on the front end and a 63 dB IF amplifier to obtain a gain of 86 dB. We chose a gain that is higher than 74 dB to offset the losses due to the mixer (conversion loss), attenuators and filters (insertion loss). We performed eight coherent integrations to obtain a 9 dB gain in signal-to-noise ratio. This large receiver gain, however, will cause the A/D to saturate when stronger reflections from the surface are received. To alleviate this problem we used a high-pass filter to attenuate the stronger signals to less than the A/D's maximum input of 4 dBm. The high-pass filter attenuates the surface reflection and the strong near-surface

reflections that occur at lower beat frequencies and passes the weaker reflections from deeper within the ice that occur at higher beat frequencies.

5.2.2 Transmitter
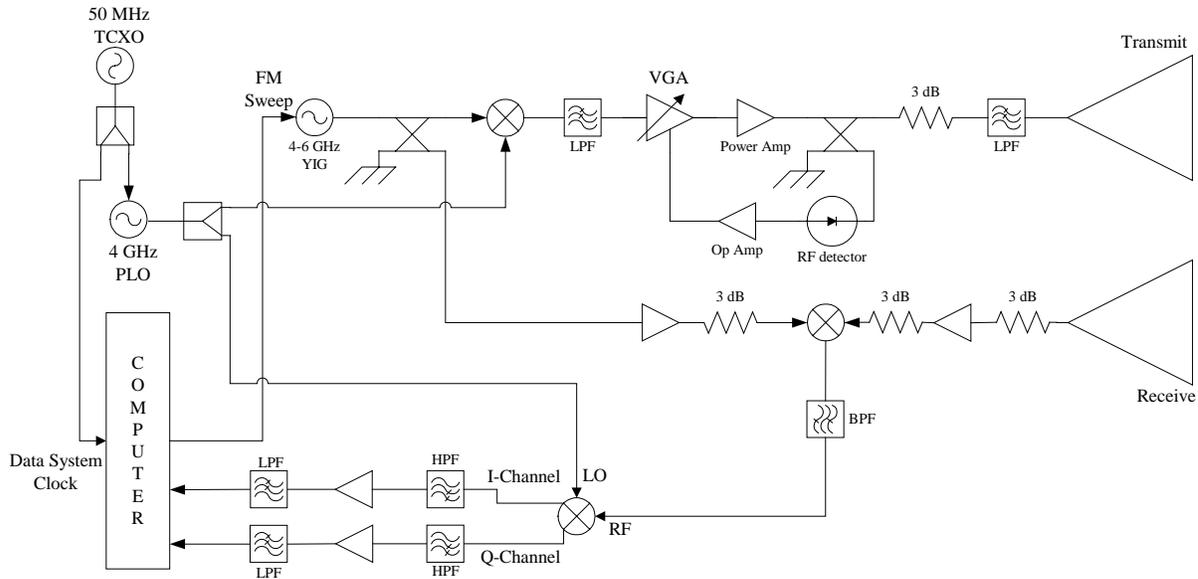
Figure 5.3. Block diagram of the prototype wideband FM-CW radar system for surface-based mapping of internal layers.

The wideband FM-CW radar system that we developed for mapping the near-surface internal layers is shown in Figure 5.3. The triangular modulation waveform is digitally generated and converted to an analog signal on a PCI card [Akins, 1999] in the host computer. This voltage is applied at the control port of a YIG oscillator to generate a transmit signal whose frequency is directly proportional to the input voltage. As indicated, the YIG oscillator can produce a 4 to 6 GHz chirp. The frequency of operation can be chosen within this bandwidth via the computer. Our

60

system was operated from 170 MHz to 2 GHz since the antenna's cutoff frequency at the lower end is 170 MHz. This frequency range is obtained by down converting the 4.17 to 6 GHz chirp using a 4 GHz signal at the LO (local oscillator) port of the mixer and low-pass filtering the output of the mixer. The 4 GHz signal is generated with a phase-locked oscillator (PLO), which is referenced to a stable 50 MHz temperature-compensated crystal oscillator (TCXO). The 50 MHz clock also serves as a reference for the data-acquisition and integration systems. This ensures that all the system clocks are synchronized for coherent integration.

Before down converting the 4.17 to 6 GHz chirp, a portion of this signal is sampled using a coupler to serve as a local oscillator for the receiver's I/Q mixer. An automatic gain control circuitry was designed to set the output power of the transmitted signal to a constant level. The variable gain amplifier's (VGA) output is further amplified to 23 dBm by a power amplifier, and a portion of this signal is coupled to a feedback loop to monitor the fluctuation in transmit power. A RF detector is used in the feedback loop to detect the power level. The RF detector has a linear relationship between the log of the input power and output voltage. The output of the RF detector is amplified using an operational amplifier to provide the appropriate voltage levels for the VGA and thus compensate for the fluctuations in the power levels. The attenuator minimizes multiple reflections between the power amplifier output and the low-pass filter. The low-pass filter suppresses any harmonics produced by the amplifier and ensures only the desired frequencies are transmitted. The transmit and receive antennas are horn antennas that could be operated from 170

MHz to 3 GHz. The mouth of the antenna measures 94 cm by 68.6 cm and the height is 93.3 cm. The antennas are shown in Figure 5.4.

Figure 5.4. Horn antennas mounted on either side of the Trackmaster.

5.2.3 Receiver

The receive antenna collects the reflected signal from the target. This signal is supplied to a mixer through an amplifier padded with attenuators both at the input and output ports because the Voltage Standing Wave Ratio (VSWR) of the wideband amplifier approaches values close to 2 at certain frequencies. The received signal is

upconverted to 4 GHz by taking the difference between the 4.17 to 6 GHz chirp and the 0.17 to 2 GHz received signal. The 4 GHz signal is band-pass filtered to remove the upper sideband. In the I/Q mixer, an IF signal whose frequency is proportional to the range is obtained by mixing the 4 GHz signal with a sample of the 4 GHz signal from the PLO.

5.2.4 IF Section

An I/Q mixer is not a requirement for FM-CW radar systems since the IF signal has non-zero beat frequency. However, we developed the radar with the option of operating it in the step-frequency radar [Izuka et al., 1984] mode as well. As such, both I and Q channel sampling were required. In the FM-CW mode, only the I channel was sampled. The IF signal was passed through a high-pass filter to suppress the strong surface reflection. The antenna feed-through signal was not an issue in this experiment as the Trackmaster (a tracked vehicle) provided a good isolation between the transmit and receive antennas (see Figure 5.4). The IF signal was further amplified and filtered with an anti-aliasing low-pass filter. The IF signal was sampled at 1 MHz and digitized using a 12 bit A/D card [Akins, 1999]. An onboard integration card [Akins, 1999] was used to coherently integrate the traces before storage into the hard drive. The digitized signal was processed to generate a reflection profile as a function of range (depth). Table 5 summarizes the system parameters.

Table 5. Summary of radar parameters.

Frequency	170 – 2000 MHz
Sweep Time	125 ms
Transmit Power	0.1 Watt
Number of Coherent Integrations	8
Antennas	TEM Horn
A/D Dynamic Range	12-bit, 72 dB
Sampling Rate	1 MHz

5.3 Experiment

For mapping the near-surface internal layers of the Greenland icesheet at the NGRIP camp, we conducted surface-based experiments during June and July of 1998, and August of 1999. The NGRIP camp is located 3000 m above sea level in the middle of the Greenland ice cap at 75.1^o N, 42.3^o W (Figure 5.5). We housed the radar system and the computer in a Hardigg box (Figure 5.6) and mounted the box on the Trackmaster. We powered the systems with a portable generator that was hoisted on top of the Trackmaster and regulated generator output with an Uninterruptible Power Supply (UPS). Figure 5.4 shows the antennas mounted on either sides of the Trackmaster with their apertures about 2 m above the snow surface. We used our system to collect data over several transects. The longest transect during the 1998 experiments was for a distance of 2 km, whereas in 1999 the transect was 10 km long. We drove the Trackmaster at a speed of about 6.7 ms^{-1} (24 kph) during our measurements. We integrated eight traces coherently before storing the data on hard disk for further processing.
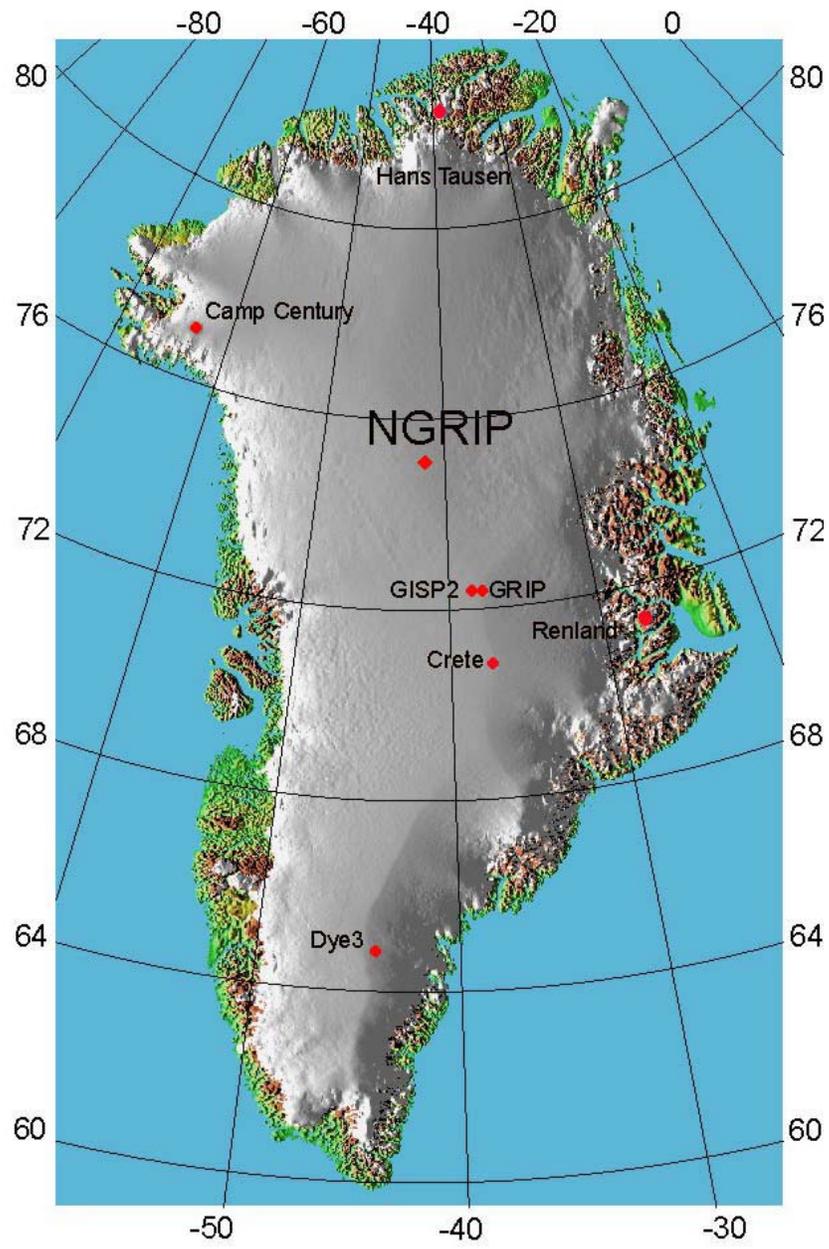
Figure 5.5. Location of the North Greenland Icecore Project (NGRIP) site (75.1° N, 42.3° W).

Figure 5.6. Radar system (top) and data-acquisition computer (bottom) mounted in a Hardigg box on the Trackmaster.

5.4 Signal Processing

The raw data from the field were processed to generate the reflection profiles. The signal processing included removing the DC offset in the time series data, applying a Hanning window to reduce the range sidelobes, and applying a Fourier transform on the windowed data to obtain the spectral response. We then designed a low-pass filter with a very low cut-off frequency for filtering the spectral data. The

66

low-pass filtered data give us an estimate of the amount of gain needed to correct for the $1/r^2$ power falloff with range, as well as the response of the high-pass filter in the IF section. The high-pass filter was used to attenuate the strong surface reflections to match the dynamic range of the received signal to the A/D converter. The original spectra were then multiplied with the inverse of the low-pass filter response to obtain the gain-corrected spectra. The gain correction was applied from a depth of about 10 m since the transition band of the high-pass filter occurs after this range. The gain correction could not be applied before this range since the stop band of the high-pass filter had attenuated the signals considerably, resulting in levels too low to invert accurately. All the spectra along the traverse were subsequently compiled to produce a reflection profile for the transect. Median filtering was applied along the layers to smooth the image.

5.5 Results and Discussion

Glacial ice and firn, particularly in the top 200 m, are stratified media. The density, and therefore the velocity of propagation, varies with depth. To determine the thickness of layers between two events from a measured range, we used the density data that was measured up to a depth of 275 m at the NGRIP site [Larsen, 1999]. The permittivity of the firn was computed using Looyenga's model [1965], which was given in Chapter 3, (3.6). We reproduce it here for convenience:

$$\varepsilon_r = \left[\left(\varepsilon_2^{1/3} - \varepsilon_1^{1/3}\right)v + \varepsilon_1^{1/3}\right]^3 \qquad (5.18)$$

where ε_2 is the dielectric constant of ice (i.e., 3.15), ε_1 is the dielectric constant of air (i.e., 1), and v is the volume fraction of ice in the firn given by:

$$v=\rho_s/\rho_i \qquad (5.19)$$

where ρ_s is the density of the firn and ρ_i is the density of pure ice (i.e., 918 kg/m^3).

Figure 5.7 shows the dielectric constant that was computed using (5.18), and Figure 5.8 shows the resulting velocity of propagation as a function of depth. We computed the range in the firn by integrating the velocity curve. The corresponding range was divided by two since the time on the scale is the two-way time.
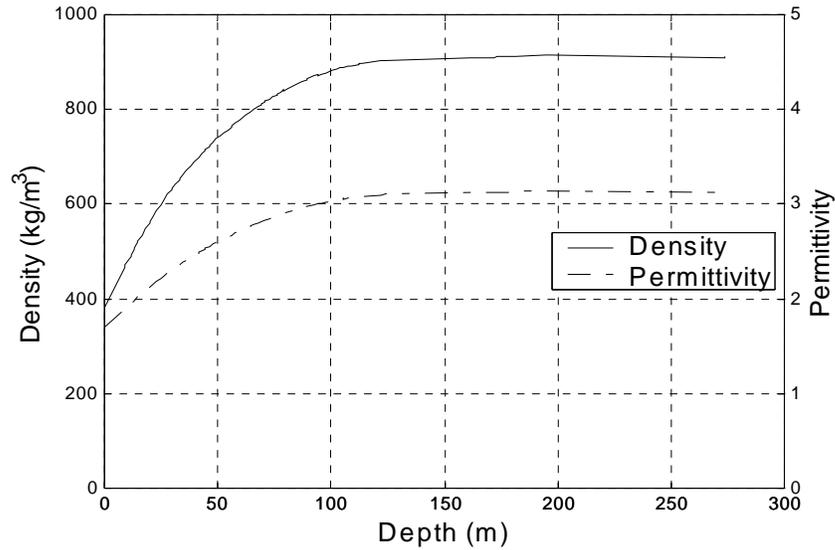
Figure 5.7. Density and permittivity of firn at NGRIP.
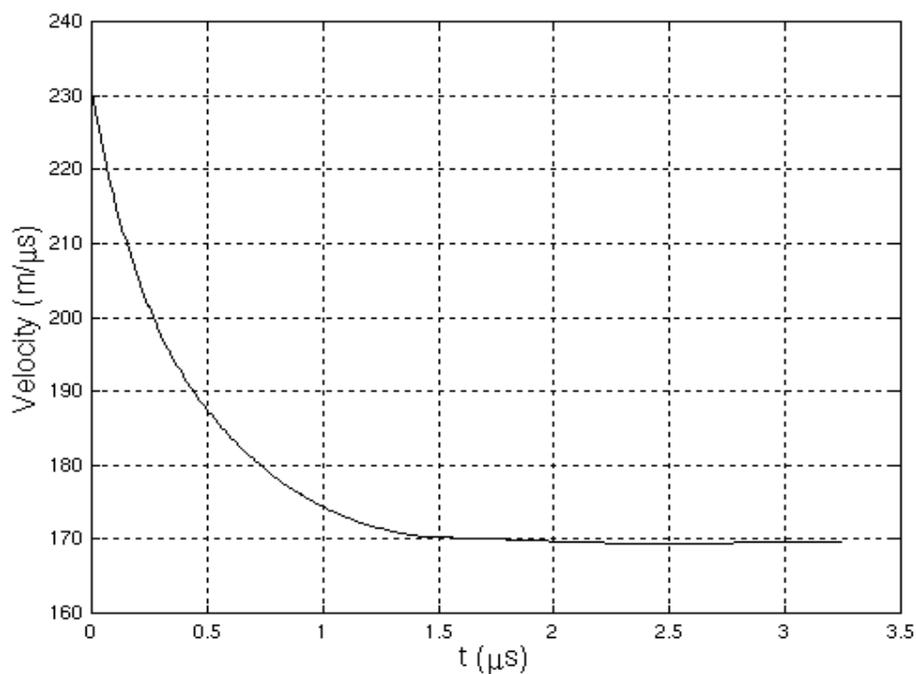
Figure 5.8. Speed of radio waves in the firn.

Figures 5.9 to 5.16 show radar reflection profiles of internal layers recorded at NGRIP. Figures 5.9, 5.11, 5.13 and 5.16 are for the 1998 field season, and figures 5.10, 5.12, 5.14 and 5.15 are for the 1999 field season. Data are plotted as a function of depth into the ice and distance traversed from the camp. We placed the electrical conductivity measurement (ECM) records to the right of the figures for comparison with the layers detected by the radar. The depths for the 1998 and 1999 data were plotted on the same scale for comparison. We currently do not have high-resolution density data for comparison with the reflection profile; hence we are unable to account for all the reflections. However, we do have a 1.7 m resolution density data for a rough comparison. This is illustrated in Figure 5.16. Some of the weaker ECM

peaks do not have a corresponding radar horizon, but the change in conductivity may be too low for the radar to detect. However, the multitude of radar horizons assures that one will always correspond with a major ECM peak.

Figure 5.9 and Figure 5.10 show layers detected from the surface to a depth of 45 m. In these figures there are two layers detected by our system that match impurities at 25 m deposited during the Katmai eruption in 1912, and a melt event in 1889 at 34 m. Figure 5.16 shows the comparison between the reflection due to density changes and the measured data. A correlation can be observed between the measured data and the profile on the right. The reflection at about 15 m and the melt layer at 34 m have a corresponding match in peak with the profile on the right. There is also a strong reflection from a depth of 40 m but this layer has yet to be identified.

Figure 5.11 and Figure 5.12 show layers detected from depths of 45 m to 105 m. Here we have another two layers that have been identified as those resulting from the Tambora volcanic event in 1816 at 55 m and the Laki volcanic event in 1783 at 60 m [Clausen, 1998].

Figure 5.13 and Figure 5.14 show layers at depths between 105 m and 165 m. According to the density profile (Figure 5.7), this depth range and below is well within the ice region where density contrasts should be minimal. These two layers we believe are due to an unknown volcanic event in 1514 at 113 m and the Mt. St. Helens volcanic event in 1479 at 118 m. Figure 5.15 shows layers that were detected between 165 m and 290 m during the 1999 experiment.

70
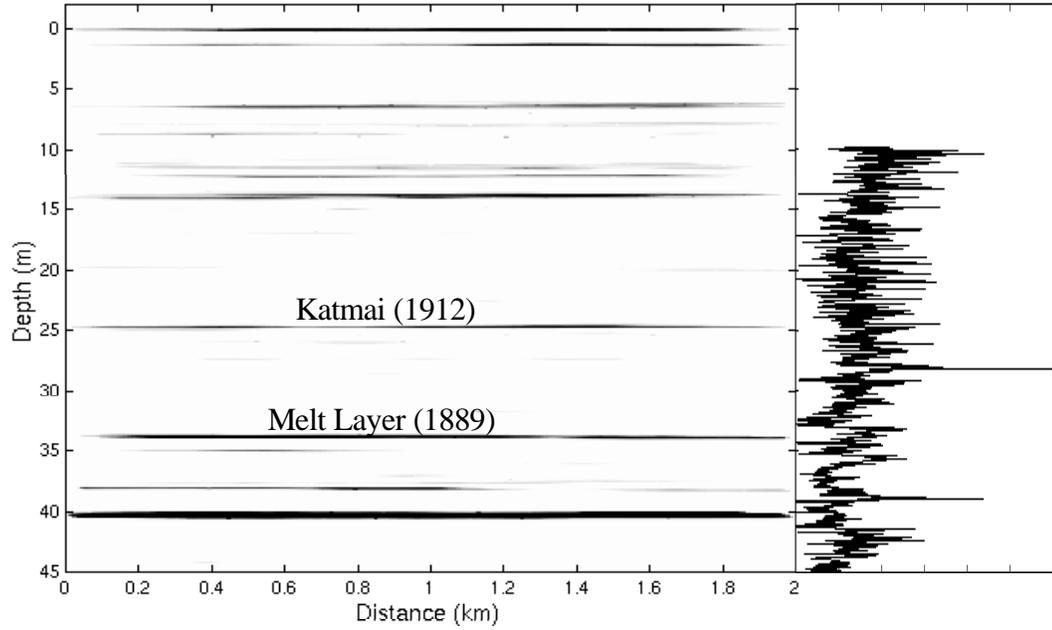
Figure 5.9. Internal layers observed along a 2 km transect in 1998 (0-45 m depth).
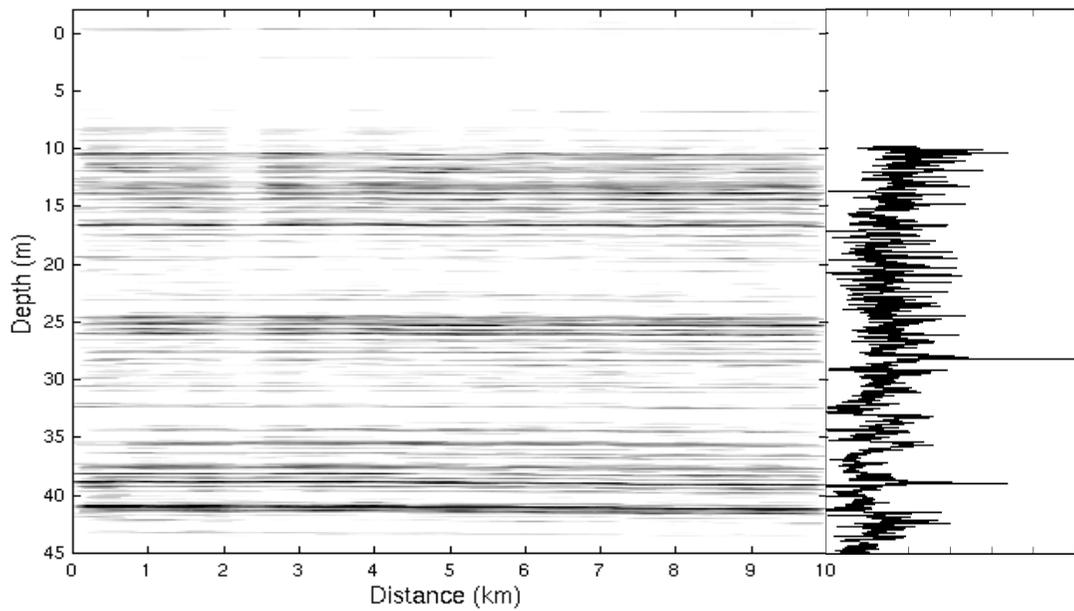
Figure 5.10. Internal layers observed along a 10 km transect in 1999 (0-45 m depth).

71
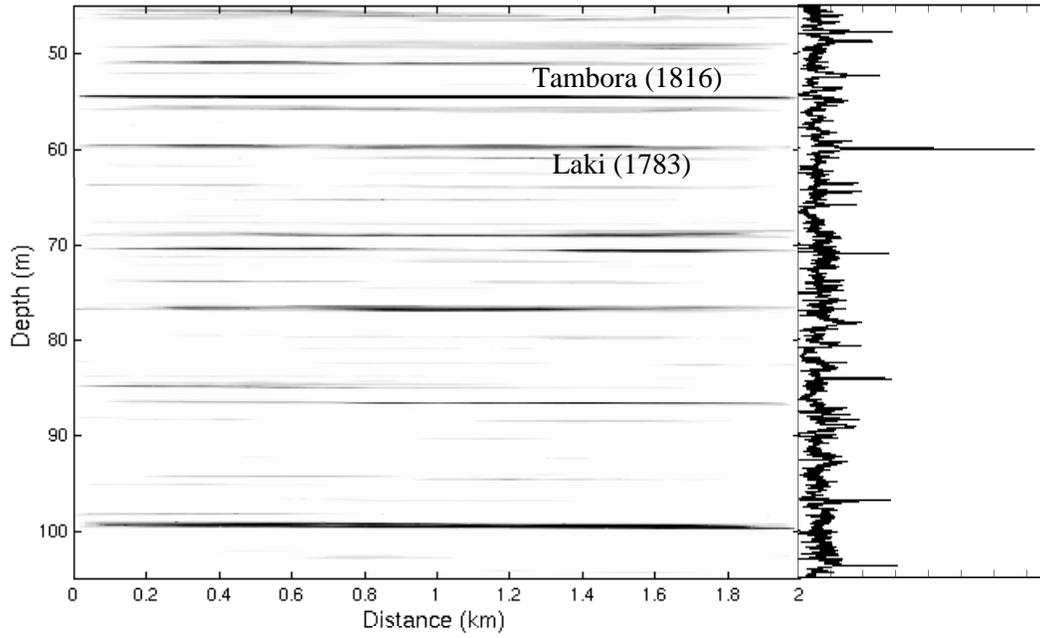
Figure 5.11. Internal layers observed along a 2 km transect in 1998 (45-105 m depth).
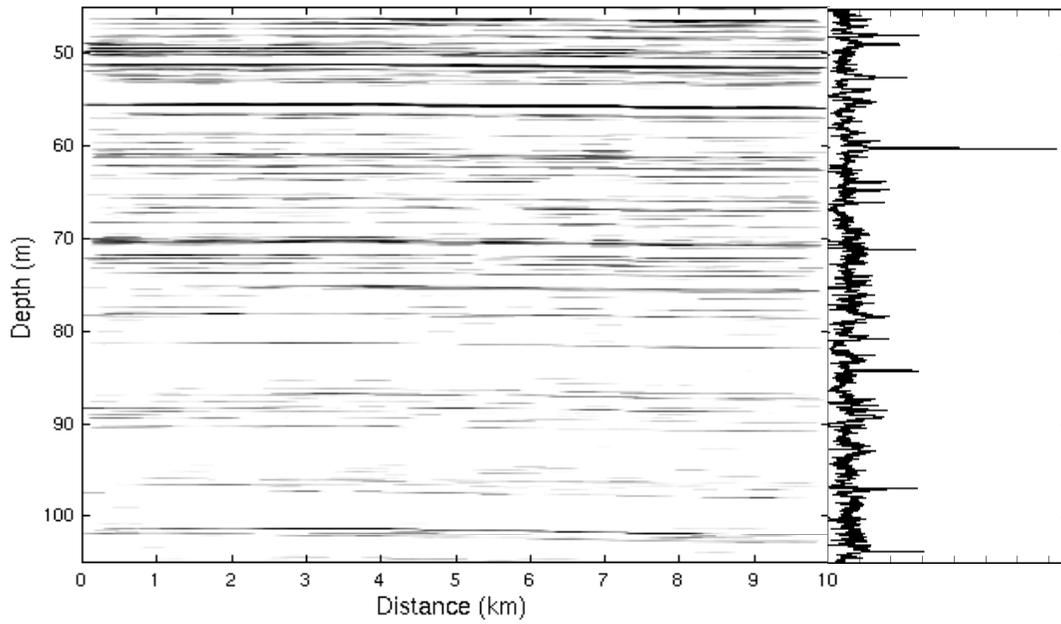
Figure 5.12. Internal layers observed along a 10 km transect in 1999 (45-105 m depth).
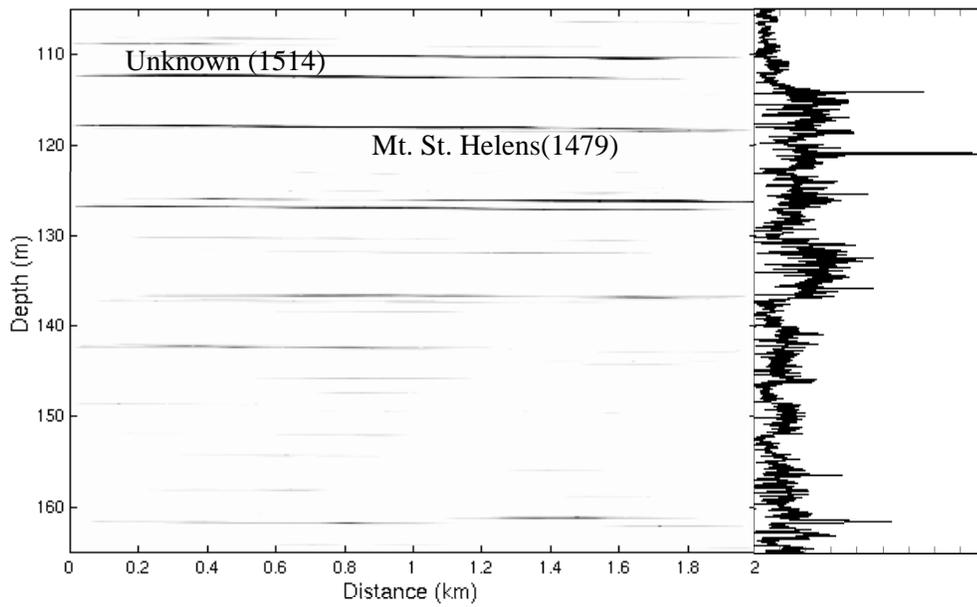
Figure 5.13. Internal layers observed along a 2 km transect in 1998 (105-165 m depth).
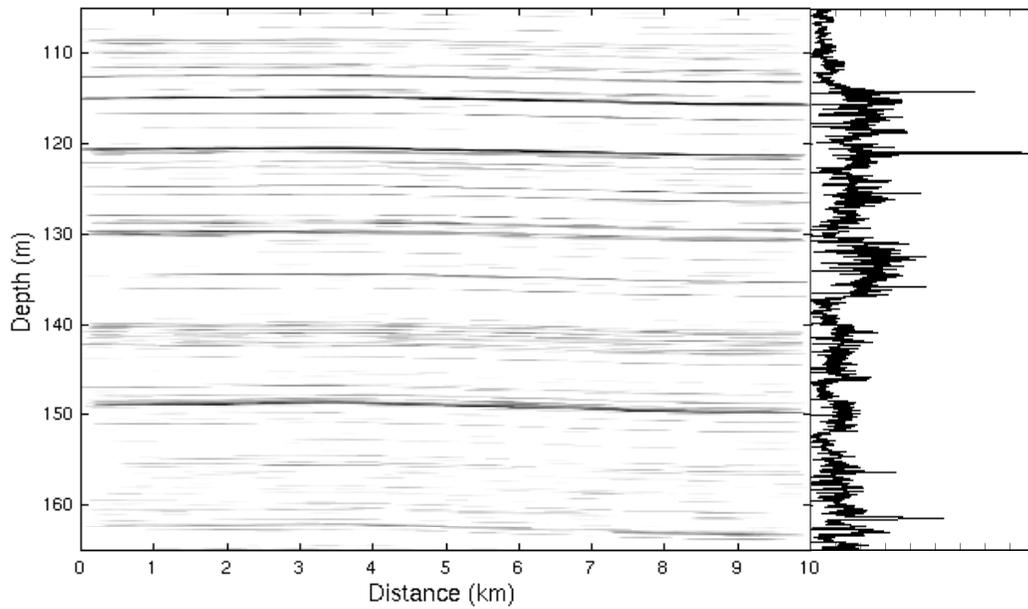
Figure 5.14. Internal layers observed along a 10 km transect in 1999 (105-165 m depth).

73
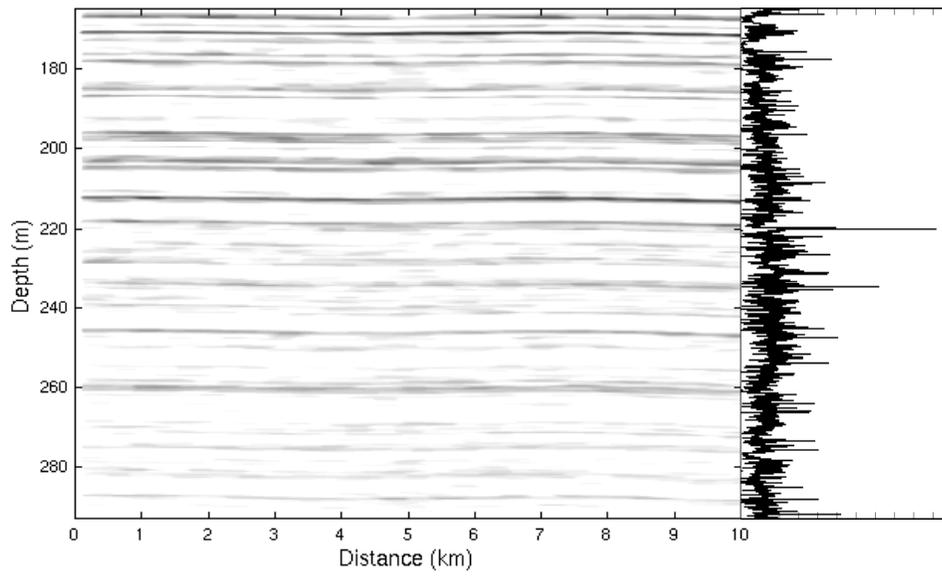
Figure 5.15. Internal layers observed along a 10 km transect in 1999 (165-290 m depth).
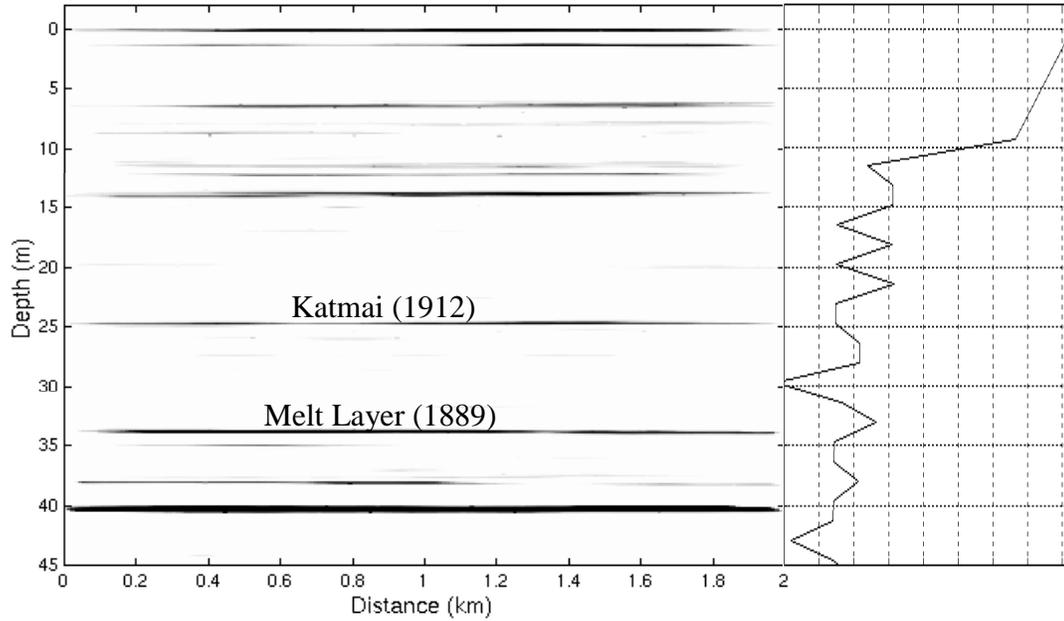
Figure 5.16. Internal layers observed in 1998 (0-45 m depth) compared with reflections due to density changes..

Table 6 shows the error between the radar-measured depths of major events and the depths determined from ice cores. This table shows that our errors are within ±2 m of the core-determined depths.

Table 6. Depth error between radar data and core data.

Event Year	Core Depth(m)	Radar Depth 1998 (m)	Error 1998 (m)	Radar Depth 1999 (m)	Error 1999 (m)
1912	27	25	-2	25	-2
1889	34	34	0	35	1
1816	53	55	2	55	2
1783	59	60	1	61	2
1601	102	100	-2	102	0
1514	114	113	-1	115	1
1479	120	118	-2	120	0
1259	162	163	1	163	1

It has been reported in a previous study [Fujita et al., 1999] that the reflections from the firn are due to the changes in the density. However in their study the data were obtained with systems that have resolution of about tens of meters. With a resolution of this magnitude it will be difficult to resolve the weak reflections due to conductivity changes from the reflections due to density changes. However, we believe we are able to resolve the reflections with our high-resolution system. We are awaiting high-resolution permittivity data to verify this. In addition, signal-processing techniques have been developed by Leuschen [2001] to recover weak reflections that have been masked by sidelobes of stronger reflections.

5.5.1 Computation of Accumulation Rate and Error Analysis

The following subsection will describe the computation of the accumulation rate based on the radar measurements and also derive the uncertainty associated with the computation. As mentioned in the previous section, the layer depths measured with our radar are within ± 2 m of the layers obtained from ice-core data. We did not adjust the density profile to match radar-determined depths with core data. Using the radar data from the 1998 and 1999 experiments and neglecting the effect of creep, we computed the average accumulation rate, A, from radar-determined depths and density data from the NGRIP core as:

$$A = \frac{dR}{dt} \frac{\rho_{layer}}{\rho_{water}}$$

(5.20)

where dR/dt is the change in thickness over time, ρ_{layer} is the average density between the two layers and ρ_{water} is the density of water.

To determine the error in our accumulation rate computation we will first have to compute the uncertainty in our range computation. The range is computed using the following equation:

$$R = \frac{c\tau}{2\sqrt{\varepsilon}}$$

(5.21)

The uncertainty in the range, σ_R, is related to the uncertainty in dielectric constant, σ_ε and is given by:

$$\sigma_R = \sigma_\varepsilon \frac{\partial R}{\partial \varepsilon} \tag{5.22}$$

$$\text{where } \frac{\partial R}{\partial \varepsilon} = -\frac{R}{2\varepsilon} \tag{5.23}$$

The uncertainty in the dielectric constant is related to the uncertainty in the density, σ_ρ, and is given by:

$$\sigma_\varepsilon = \sigma_\rho \frac{\partial \varepsilon}{\partial \rho} \tag{5.24}$$

where

$$\frac{\partial \varepsilon}{\partial \rho} = 3\left[\left(\varepsilon_2^{1/3} - \varepsilon_1^{1/3}\right)\frac{\rho}{\rho_i} + \varepsilon_1^{1/3}\right]^2 \left[\frac{\left(\varepsilon_2^{1/3} - \varepsilon_1^{1/3}\right)}{\rho_i}\right] \tag{5.25}$$

hence

$$\sigma_\varepsilon = \sigma_\rho 3\left[\left(\varepsilon_2^{1/3} - \varepsilon_1^{1/3}\right)\frac{\rho}{\rho_i} + \varepsilon_1^{1/3}\right]^2 \left[\frac{\left(\varepsilon_2^{1/3} - \varepsilon_1^{1/3}\right)}{\rho_i}\right] \tag{5.26}$$

Substituting (5.25) and (5.26) into (5.22) we obtain the error expression for our range computation as:

$$\sigma_R = \frac{-\sigma_\rho 3R\left[\frac{\left(\varepsilon_2^{1/3} - \varepsilon_1^{1/3}\right)}{\rho_i}\right]}{2\left[\left(\varepsilon_2^{1/3} - \varepsilon_1^{1/3}\right)\frac{\rho}{\rho_i} + \varepsilon_1^{1/3}\right]} \tag{5.27}$$

In addition to the error in the range due to uncertainty in the density, the range computation also depends on the resolution of the radar. Although we transmitted a 2 GHz-bandwidth signal, the frequency response of a typical reflection from the

internal layer (Figure 5.17) shows a 10 dB bandwidth of 500 MHz. This translates to a ±30 cm uncertainty in the range. Hence the overall uncertainty in the range computation would be

$$\sigma_R = \frac{-\sigma_\rho 3R\left[\dfrac{\left(\varepsilon_2^{1/3} - \varepsilon_1^{1/3}\right)}{\rho_i}\right]}{2\left[\left(\varepsilon_2^{1/3} - \varepsilon_1^{1/3}\right)\dfrac{\rho}{\rho_i} + \varepsilon_1^{1/3}\right]} \mp 0.3 \tag{5.28}$$

where σ_ρ, the uncertainty in the density measurement, is 5%. This result can then be used to compute the uncertainty in the accumulation rate. The uncertainty in accumulation rate, σ_A, is given by:

$$\sigma_A = \sqrt{\left(\sigma_R \frac{\partial A}{\partial R}\right)^2 + \left(\sigma_\rho \frac{\partial A}{\partial \rho_{layer}}\right)^2} \tag{5.29}$$

where
$$\frac{\partial A}{\partial R} = \frac{\rho_{layer}}{t\rho_{water}} \tag{5.30}$$

and
$$\frac{\partial A}{\partial \rho_{layer}} = \frac{R}{t\rho_{water}} \tag{5.31}$$

Equation 5.29 becomes:

$$\sigma_A = \sqrt{\left(\sigma_R \frac{\rho_{layer}}{t\rho_{water}}\right)^2 + \left(\sigma_\rho \frac{R}{t\rho_{water}}\right)^2} \tag{5.32}$$

Table 7 and Table 8 show the computed water-equivalent accumulation rate per year along with its uncertainty, over the periods indicated in column one. The average density was determined by averaging the density of firn over the indicated period. The accumulation rate over this period is then calculated using (5.20). The average accumulation rate between 1259 and 1997 was determined by taking a weighted sum of the accumulation rate for each of the periods indicated in column one and dividing it by the total number of years over this period. Equation 5.29 was used to determine the uncertainty in the accumulation rate. The uncertainty over the entire period was determined by taking the square root of the sum of the squares of the uncertainty of the accumulation spanning this period; i.e.,

$$\sigma_A = \sqrt{\sigma^2_{A_{layer1}} + \sigma^2_{A_{layer2}} + ... + \sigma^2_{A_{layerN}}}$$

(5.33)

The average yearly rate between 1259 and 1997 was computed to be 17.3 cm/yr with an uncertainty of about 4%. Dahl-Jensen et al. [1997] report that modeling results indicate that the average snow accumulation rate is about 19 cm/yr. However measurements at a location close to the NGRIP camp located at 75.0^o N, 42.0^o W, indicate an accumulation rate of 17.1 cm/yr [Kipfstuhl, 1998].

Table 7. Computed accumulation rate from 1998 radar data.

Year	Measured Thickness(m)	Avg. Density (g/cm^3)	cm/yr.	% Error
1912-1997	25	0.50	14.59	1.49
1889-1912	9	0.63	24.62	2.28
1816-1889	21	0.71	20.49	1.50
1783-1816	5	0.77	11.68	1.26
1601-1783	40	0.84	18.42	1.12
1514-1601	13	0.89	13.29	0.09
1479-1514	5	0.90	12.84	1.32
1259-1479	45	0.91	18.59	1.04
		Mean=	**17.3**	±4.01%

Table 8. Computed accumulation rate from 1999 radar data.

Year	Measured Thickness (m)	Avg. Density (g/cm^3)	cm/yr.	% Error
1912-1997	25	0.50	14.59	1.49
1889-1912	10	0.63	27.49	2.47
1816-1889	20	0.71	19.59	1.43
1783-1816	6	0.77	14.05	1.35
1601-1783	41	0.84	18.96	1.14
1514-1601	13	0.89	13.33	0.87
1479-1514	5	0.90	12.87	1.32
1259-1479	43	0.91	17.76	0.99
		Mean=	**17.3**	±4.12%

5.5.2 Determination of Optimum Frequency for Airborne Radar

We analyzed the data to determine the frequency response of the signal reflected by some of the layers. The frequency response of the layer was determined

by taking the IFFT of the filtered layer return and calibrating it with respect to the return from a metal plate. We used computed wave speed in the firn to estimate range to the layer. Figure 5.17 shows the frequency response of the reflection from the layer located at about 115 m and 148 m. This result indicates that most of the contribution to the layer reflection is due to the signal in the 500-1,000 MHz range. A somewhat odd-looking feature of Figure 5.17 is the decreasing amplitude with decreasing frequency which is counterintuitive to what we have seen so far in terms of propagation loss. The decreasing amplitude with respect to frequency is due to the finite layer thickness, which gives rise to a sinusoidal modulation of the reflection coefficient as seen in (3.1). To illustrate the effect of finite layer thickness, we simulated the response of a layer embedded at 148 m below the firn. The layer thickness is assumed to be of the order of the annual accumulation rate [Fujita and Mae, 1994]. Figure 5.18 shows the setup of the EEsof® simulation, which is similar to the setup shown in Figure 3.3. A layer of thickness 17 cm is assumed since the accumulation rate is 17 cm in the NGRIP region. The result of the EEsof® simulation is shown in Figure 5.19.
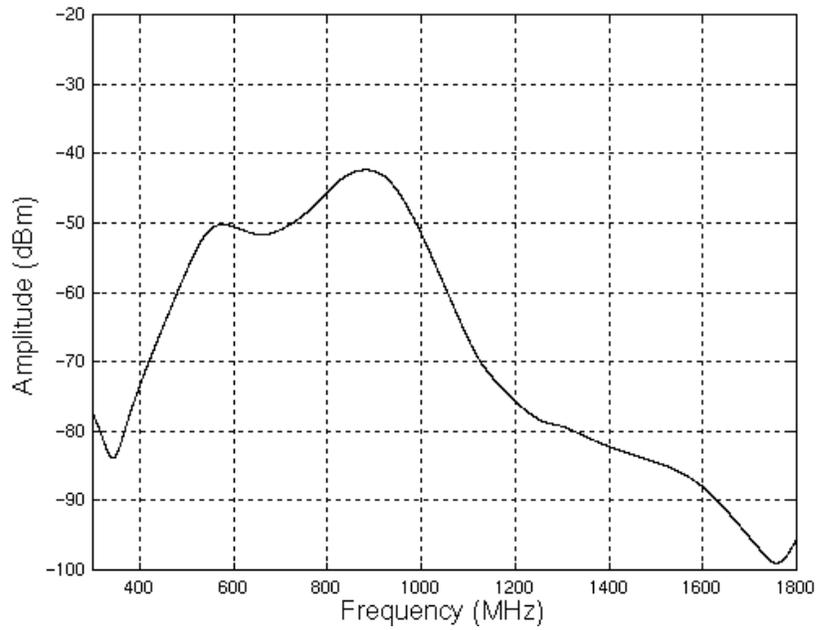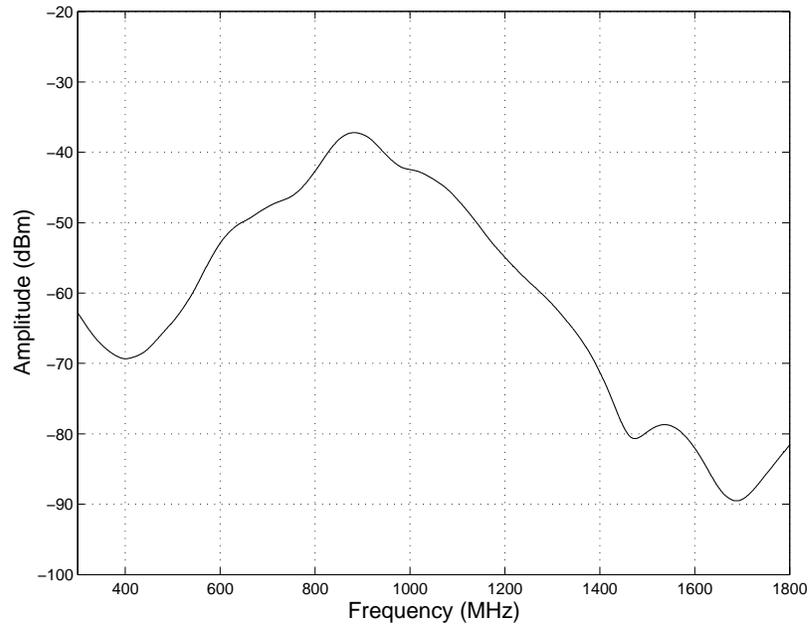
Figure 5.17. Frequency response of reflection from layer located at about 115 m (top) and 148 m (bottom).

TLINP
TL1
Z=50.0 Ohm
L=148 meter
K=3
F=fsc
TanD=0

TLINP
TL2
Z=35.0 Ohm
L=0.17 meter
K=3
F=fsc
TanD=0

TLINP
TL3
Z=50.0 Ohm
L=5000 meter
K=3
F=fsc
TanD=0

Term
Term1
Num=1
Z=50 Ohm

TimeDelay
TD1
Delay=1.67 usec
ZRef=50. Ohm

Term
Term2
Num=2
Z=50 Ohm

VAR
VAR1
fsc=600e6

S-PARAMETERS

S_Param
SP2
Start=170 MHz
Stop=2000 MHz
Step=1.02e6
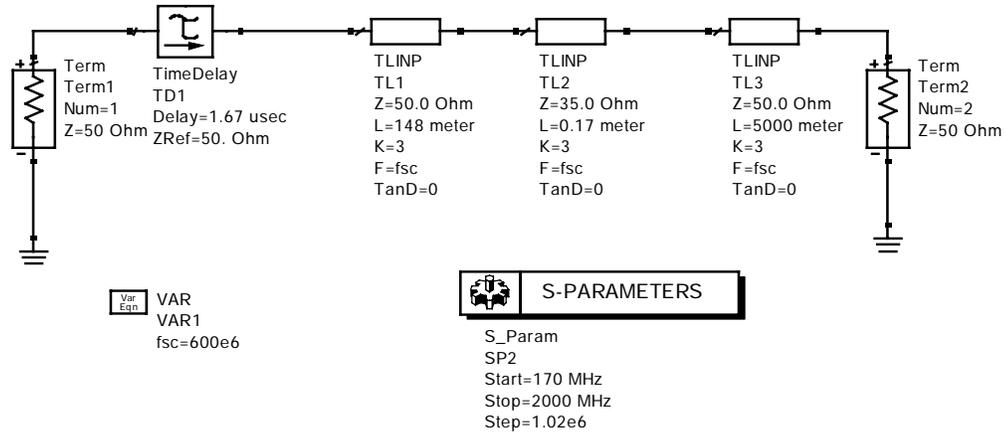
Figure 5.18. EEsof® setup to simulate the effects of finite layer thickness.
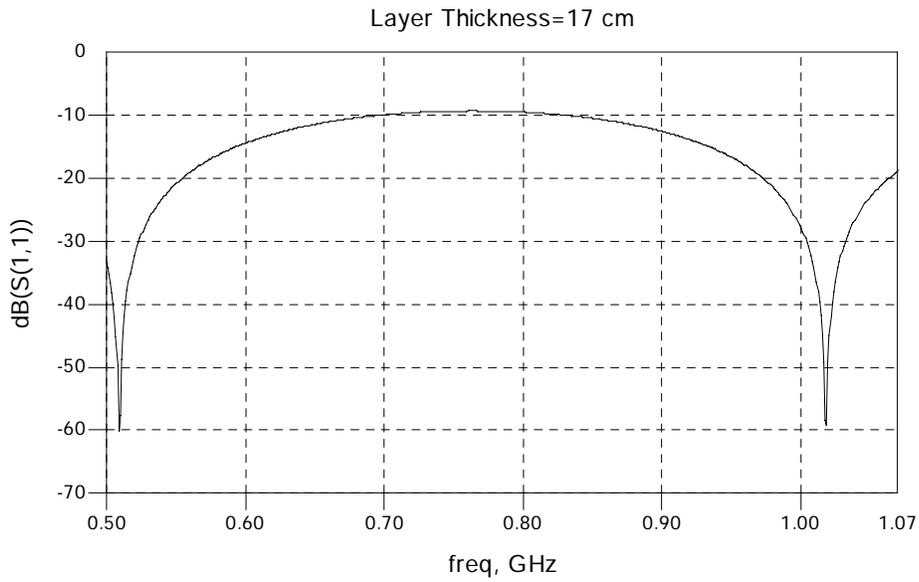
Figure 5.19. Simulated frequency response of reflection from a 17 cm layer.

83
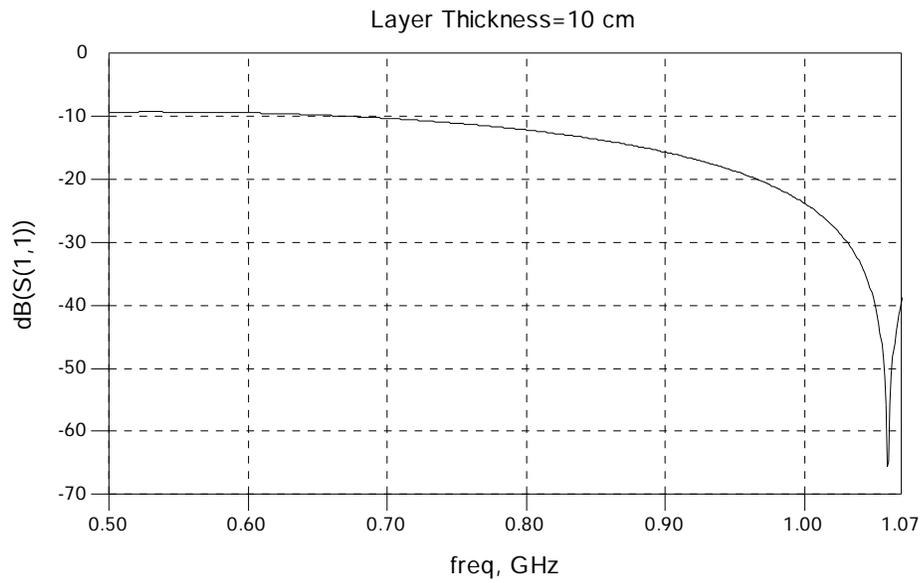
Figure 5.20. Simulated frequency response of reflection from a 10 cm layer.
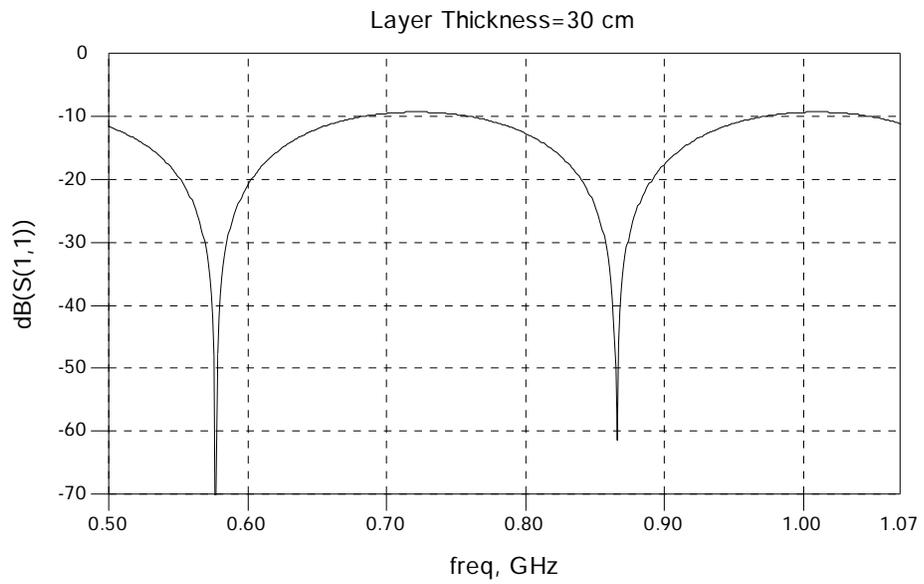
Figure 5.21. Simulated frequency response of reflection from a 30 cm layer.

The simulation result does not exactly match our measured response as we did not account for propagation and scattering losses. The general trend, however, can be observed to be in good agreement with the reflection coefficient of the return from the layer peaking between 600 and 1,000 MHz. We repeated the simulation for a layer thickness of 10 cm and 30 cm and noted that the oscillation of the reflection coefficient increases with increasing layer thickness. The sinusoidal property of the reflection coefficient can be used to determine the thickness of a layer if the resolution of the radar is greater than the annual accumulation rate.

5.6 Summary

In this chapter, we reviewed the concept of FM-CW radar and derived the required specifications for a FM-CW radar to detect internal layers in the dry snow region of the Greenland ice sheet. We described the system that was developed and the experiments that were carried out at the NGRIP campsite during the summers of 1998 and 1999. We presented the results that were obtained with our system and showed that the measurements were within ± 2 m of the layers obtained from ice-core data. We computed the uncertainty in the accumulation rate to be around 4% based on the radar measurements. We also determined the optimum frequency range of the measurements to be between 500 MHz to 1,000 MHz in the NGRIP area.

Chapter 6

PROTOTYPE AIRBORNE SYSTEM

Frequency analyses of the layer reflections from the surface-based experiment described in the previous chapter reveal that the reflections are strongest at the 500-1000 MHz frequency range. Based on this result and taking into consideration the frequencies used for communication in the P-3 aircraft, we developed a 600-900 MHz coherent airborne FM-CW radar for high-resolution mapping of the internal layers in the Greenland ice sheet. Airborne measurements were made with the prototype system over the Greenland ice sheet during the May 2001 field season. In this chapter, we will present detailed design of the airborne radar and the results from measurements made over the Greenland ice sheet.

6.1 System Design

The derivation of system specifications for the airborne system is similar to the surface-based system described in the previous chapter. The goal is to develop a system that can map internal layers in the upper 100 m of ice. This will be more than adequate for our current purpose since most of the ice cores that have been collected to create the latest accumulation map [Bales, et al., 2001a] were in the top 20 m of ice. Also the frequency of operation for the system must be selected to avoid interference with communication and navigation equipment aboard the NASA P-3 aircraft. Table 9 shows the frequency of instruments aboard the P-3.

Table 9. Frequency of equipment aboard NASA's P-3 aircraft.

Equipment	Frequency
ADF Receiver	190 – 2185 kHz
HF Comm.	2 – 30 MHz
Marker Beacon	75 MHz
VHF Nav. Receiver	108 – 118 MHz
VHF Comm.	30 – 88 MHz
VHF Comm.	118 – 174 MHz
UHF Comm.	225 – 400 MHz
DME/TACAN	960 – 1215 MHz
Transponder	1030 MHz
GPS Receiver	1575 MHz
Satcom Receiver	1525 – 1559 MHz
Satcom Transmitter	1626.5 – 1660.5 MHz
Radio Altimeter	4300 MHz
Weather Radar	9345 MHz

Based on the frequency analyses of layer data from surface-based experiments, where the optimum frequency range is found to be between 500 and 1000 MHz, and the available range of 400-960 MHz on the P-3 aircraft, we chose the frequency of operation of our system to be 600 – 900 MHz. This provides a range resolution of 0.5 m in free space. To prevent any leakage and to minimize the use of very high order filter a guard band of 100 MHz at the lower end and 60 MHz at the higher end were used.

As discussed in Chapter 3, changes in density are indicators of annual accumulation of snow. In Chapter 4, we showed that the reflection coefficient due to density changes is greater than -55 dB for the first 100 m. Our system will be designed to detect these changes. We will first determine the minimum detectable signal with the first three components being a 3-dB attenuator, band-pass filter and a low-noise amplifier.

Table 10. Noise figures of the front end of the receiver.

Component	Gain (dB)/(Linear)	F (dB)/(Linear)
1. Attenuator	-3 / 0.5	3 / 2
2. Band-pass Filter	-2 / 0.63	2 / 1.58
3. Amplifier	24 / 251.2	2.9 / 1.95

Substituting the above parameters into (5.13) yields an effective noise figure of 6.18 (7.9 dB). The bandwidth, B, of a range bin in our airborne system is:

$$B = \frac{Sampling\,Rate}{\#\,of\,DFT\,Points} = \frac{50\,MS/s}{5000} = 10\,kHz \qquad (6.1)$$

The minimum detectable signal, from (5.12) is thus –126 dBm.

The tables below tabulates the expected return power from the air/firn interface and dielectric discontinuities within the firn. The height of the aircraft is assumed to be 500 m above the firn surface and the annual layer of the firn that we wish to detect is assumed to be 100 m below the surface of the firn. We also assumed a transmit power of 0 dBm.

Table 11. Expected return from air/firn interface.

Frequency (MHz)	λ (cm)/(dB)	Gain (dB)	PRC (dB) (air/firn)	S (dBm)
600	50 / -3.0	8.2	-15	-87
700	43 / -3.7	9.1	-15	-86
800	38 / -4.3	9.7	-15	-86
900	33 / -4.7	9.4	-15	-88

Table 12. Expected return from annual layer at a depth of 100m.

Frequency (MHz)	λ (cm)/(dB)	Gain (dB)	PRC (dB) (annual layer)	α (dB)	S (dBm)
600	50 / -3.0	8.2	-55	-2.5	-131
700	43 / -3.7	9.1	-55	-2.9	-131
800	38 / -4.3	9.7	-55	-3.3	-131
900	33 / -4.7	9.4	-55	-3.8	-133

The expected returns from the annual layer are lower than the minimum detectable signal for the given transmit power. We chose a transmit power of 30 dBm, which will put the received signal power from the annual layers above the minimum detectable signal level by more than 20 dB, assuming that the S/N ratio is limited by thermal noise.

To determine the required number of coherent integrations, we first need to compute the maximum distance over which integration can be performed. For unfocused synthetic aperture radar, the maximum integration length, L_{max}, is given as [Wehner, 1995]:

$$L_{max} = 0.5\sqrt{R\lambda} \qquad (6.2)$$

where R is the height of the aircraft above the firn and λ is the wavelength. Obviously, the highest frequency of the system will determine the integration length since the wavelength is the smallest at the highest frequency. For a platform height of 500 m and frequency of 900 MHz the integration length turns out to be 6.5 m. The relationship between the integration length, PRF (pulse repetition frequency), number of integrations, N, and velocity of the aircraft, v, is:

$$L_{max} \geq \frac{vN}{PRF} \qquad (6.3)$$

The aircraft travels at an average ground speed of 130 ms^{-1}. Since the sweep time of source is 100 μs, the maximum PRF for the system is 10 kHz. We were, however, operating our system at only 2 kHz. We plan to operate it at a higher PRF during the next field season in 2002. With these parameters, the number of coherent integrations turns out to be 100. This will provide a 20 dB improvement in the SNR.

We now have all the required parameters to compute the receiver gain. We want the gain of the receiver such that there is a greater than 20 dB signal-to-noise

ratio at the A/D. We note however that since the minimum signal level we want to detect is 20 dB higher than the noise floor we are not going to gain any additional SNR unless there are other sources of non-coherent noise picked up by the receiver. As such, we modify (5.17) by omitting the integration gain term and express it as:

$$S + P_t + G_{rcvr} > A/D \text{ noise floor} + SNR \tag{6.4}$$

$$-133 + 30 + G_{rcvr.} > -70 + 20$$

$$G_{rcvr.} > 53 \text{ dB}$$

The receive chain was designed to have about 60 dB net gain to compensate for any errors.

6.1.1 Transmitter
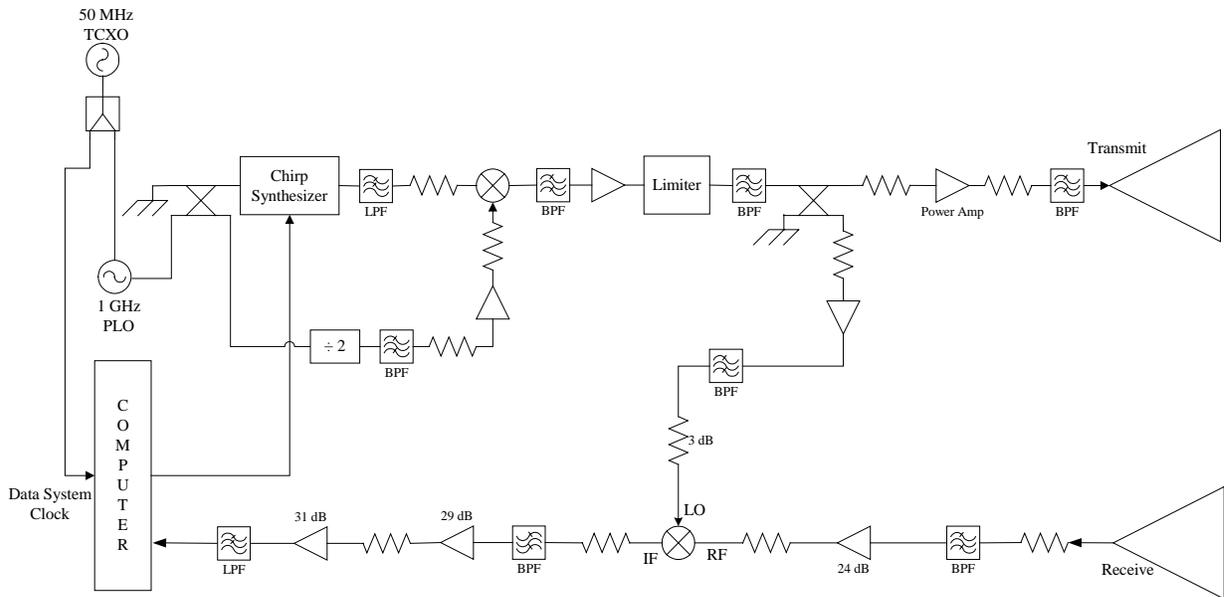
Figure 6.1. Block diagram of the prototype wideband FM-CW radar system for airborne mapping of internal layers.

Figure 6.1 shows the radar system we designed for airborne mapping of the internal layers over the Greenland ice sheet. The signal source is the STEL-9949 programmable digital chirp synthesizer (DCS). It can be operated with a maximum clock frequency of 1 GHz to generate a chirp signal between 1 MHz and 400 MHz. It can also be programmed to generate a single carrier frequency in this range. The DCS has a TTL level trigger input that is used to start the chirp and control its duration. The pulse width of the trigger input controls the duration by driving a switch at the output of the DCS. The switch is turned on when the trigger goes low. The pulse width of the trigger signal was set equal to a sweep time of 100 μs. Figure 6.2 shows

the output from the synthesizer. Besides the main chirp from 100-400 MHz, there is also a 600-900 MHz image signal and a 1 GHz clock signal. The image and clock signals were filtered out using a low-pass filter with cutoff frequency at 440 MHz. The 600 to 900 MHz chirp is generated by upconverting the 100 to 400 MHz chirp using a 500 MHz phase-locked signal. The 500 MHz signal is obtained by dividing the 1 GHz phase-locked oscillator (PLO) clock by 2. The 1 GHz PLO is referenced to a 50 MHz temperature-compensated crystal oscillator (TCXO). A sample of the 50 MHz signal is used as the input clock for the timing system. This ensures that all the signals are synchronized. The chirp signal is amplified and propagated through a limiter that sets the output power to a constant level. The signal is finally amplified to 2 W by a 40-dB gain amplifier and is passed through a 3 dB attenuator, a band-pass filter and coupled to a TEM horn antenna. The attenuator minimizes the effects of mismatch between the amplifier and the transmit antenna. The band-pass filter is used to suppress any spurious and harmonic signals. The TEM horn is the same as that used during the surface-based experiment and is shown in Chapter 5.
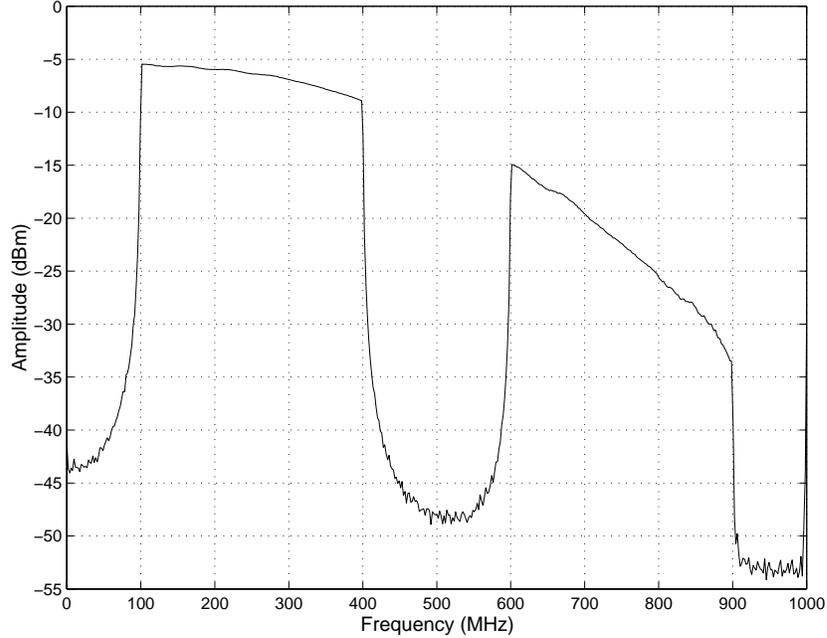
Figure 6.2. Synthesizer output.

6.1.2 Receiver

The signal is received with a TEM horn antenna and all out-of-band signals are rejected with a band-pass filter before being amplified. The amplified signal is mixed with a portion of the transmit signal to obtain the IF signal. This signal is high-pass filtered to suppress the antenna feed-through signal. The beat frequency of the signal from the firn surface is expected to be about 10 MHz since the aircraft is flying about 500 m. The high-pass filter was designed with a cut-off frequency of 10 MHz. We do not have to attenuate the surface return since our computations in Table 11 and Table 12 show that the difference between the surface and internal returns is about 50 dB, which is less than the dynamic range of the A/D. We only need to consider the

94

antenna feed through, which we did not know at the time of this design. Hence, a high-order band-pass filter was designed to ensure that the antenna feed through was rejected. The amplifier that we used after the band-pass filter had a low-pass roll-off after 900 MHz. This helped to further suppress the upper side-band signal that could otherwise saturate the amplifier which had a fairly high-gain of 29 dB. We had another amplifier with a gain of 31 dB to further amplify the IF signal. The IF signal is finally low-pass filtered to prevent the LO leakage and other out-of-band signals from being aliased into the IF band. One hundred traces were acquired and coherently integrated before storing it onto a hard drive. The A/D that was used to digitize the signal is the same one used during the surface-based experiment; i.e. 12 bits. The traces, however, were sampled at 50 MHz instead of 1 MHz. The table below summarizes the radar system's parameters:

Table 13. Operating parameters of airborne system.

Frequency	600 – 900 MHz
Sweep Time	100 μs
PRF	2 kHz
Transmit Power	1 W
Number of Coherent Integrations	100
Antennas	TEM Horn
A/D Dynamic Range	12 bit, 74 dB
Sampling Rate	50 MHz

6.2 Experiment

The University of Kansas, as a part of the NASA PARCA initiative, has been performing measurements from the NASA P-3 aircraft over the Greenland ice sheet for several years. We have been making ice thickness measurements using a coherent radar [Gogineni et al., 1998], while the NASA team has been conducting surface elevation measurements using a laser altimeter [Krabill et al., 1999]. During the May 2001 field mission we installed the wideband radar in the P-3 for mapping the internal layers along with the other systems. The installation of our system in the aircraft is shown in green in Figure 6.3. The radar system and computer were installed in a rack by the wing of the aircraft. The horn antennas were installed in the bomb bay of the aircraft. A low-loss RF cable was used to connect the transmitter and receiver to the antennas.

The primary purpose of the test flights was to show that it is possible to map the near-surface isochronous layers in the Greenland ice sheet using our high-resolution radar. The test flights were also important in helping to evaluate the performance of the radar system. Figure 6.4 shows the flight lines over which data were collected using the wideband radar.
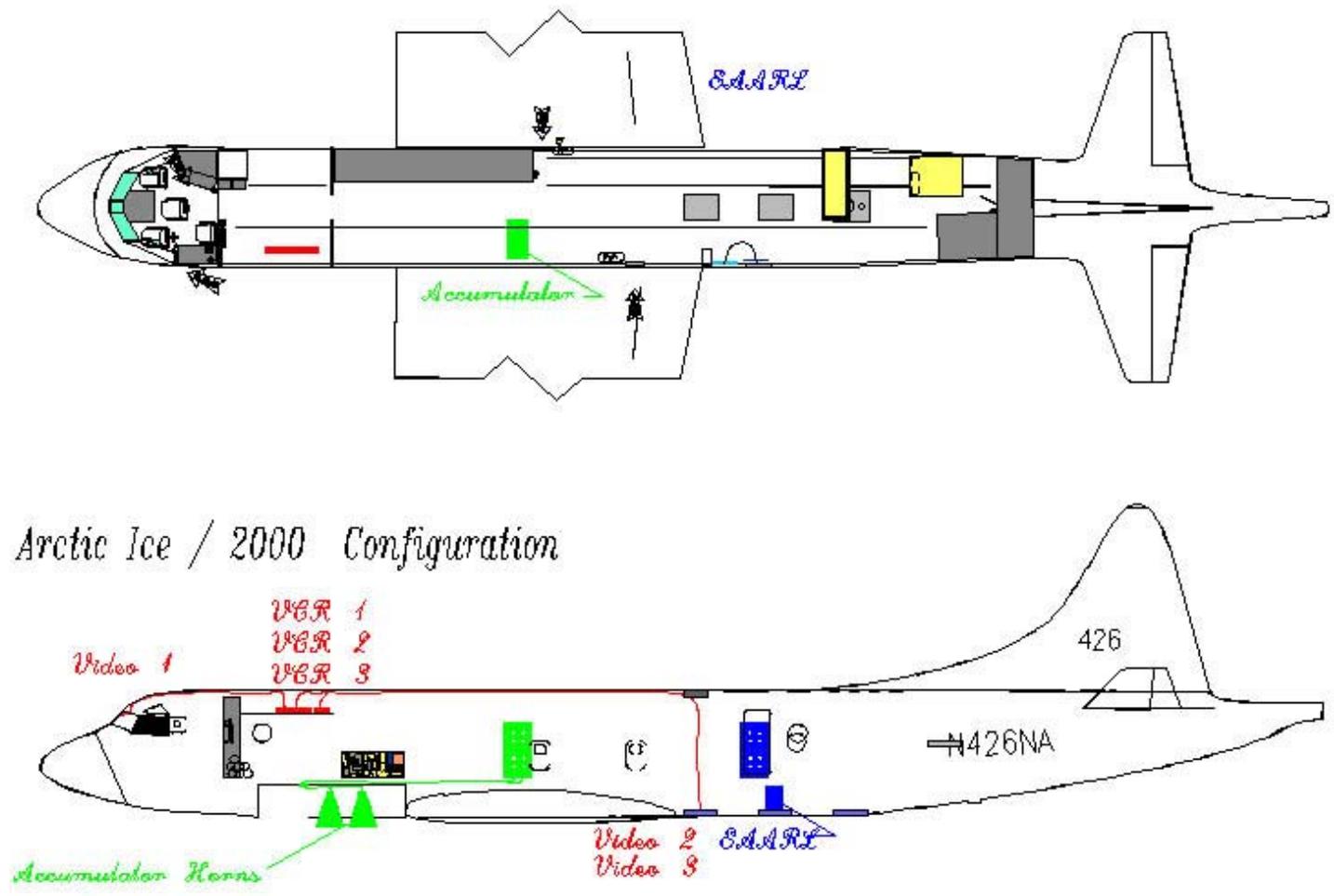
Figure 6.3. Location of accumulation radar and antennas marked in green on NASA's P-3 (courtesy of Doug Young, NASA Wallops).
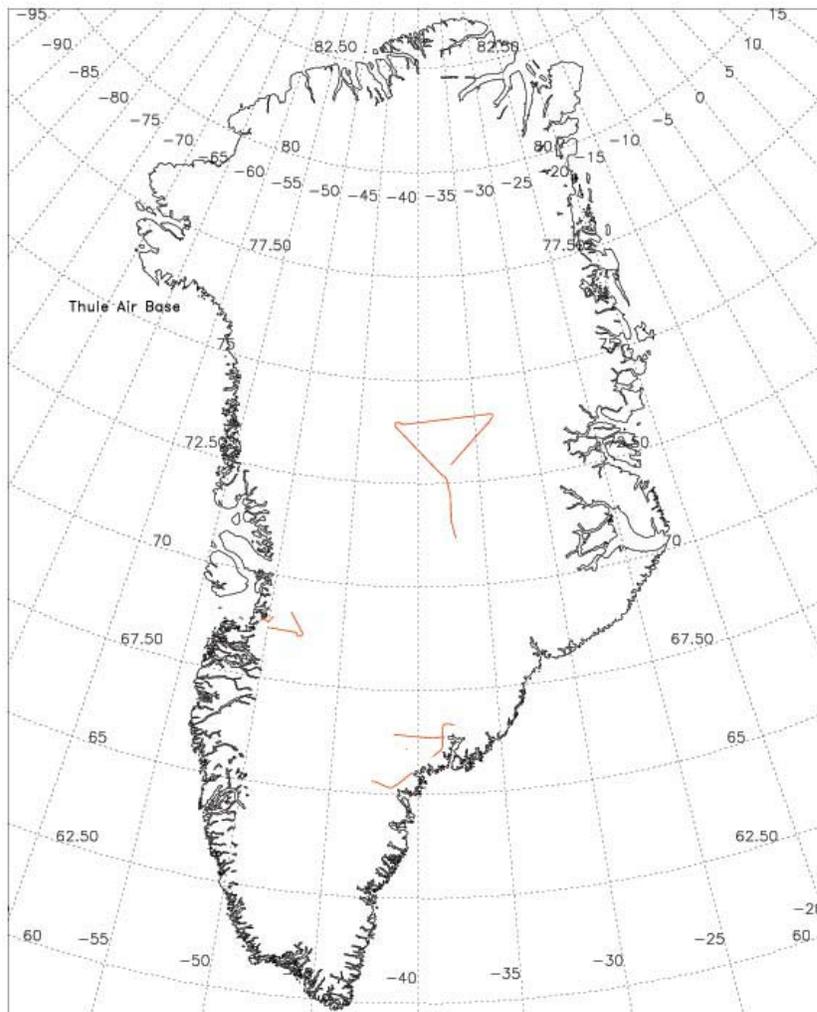
Figure 6.4. Lines over which data were collected with the accumulation radar during

the May 2001 field season.

6.3 Signal Processing and Results

The signal processing techniques for the airborne measurements are very similar to the processing techniques described in the previous chapter for the surface-

based data. However, we did not use median filtering in the airborne data. Median filtering in the horizontal direction of the layers worked well in the surface-based data since there was very little undulation of layers in the distance traversed. The airborne data contain relatively large number of undulations since we were traversing large distances. Inspection of the data revealed that smoothing in the horizontal direction was not required since the layers were well defined. To improve the display of the layers, we performed several operations on the data. As in the surface-based radar data, we low-pass filtered the spectral data to get an estimate of the $1/r^2$ power roll-off and other low-frequency variations in the data. The spectral data were then divided by this estimate to get a better use of the dynamic range of the display. Figure 6.5 shows the spectral response before and after the gain compensation. The first sample in the figure is the return from the surface. We can clearly see the large difference between the strong surface return and the weaker returns from within the ice in the top figure. However, in the bottom figure, after gain compensation, this variation cannot be observed. We further applied a difference operator in the vertical direction (into the ice) to detect the layers and remove the DC offset.
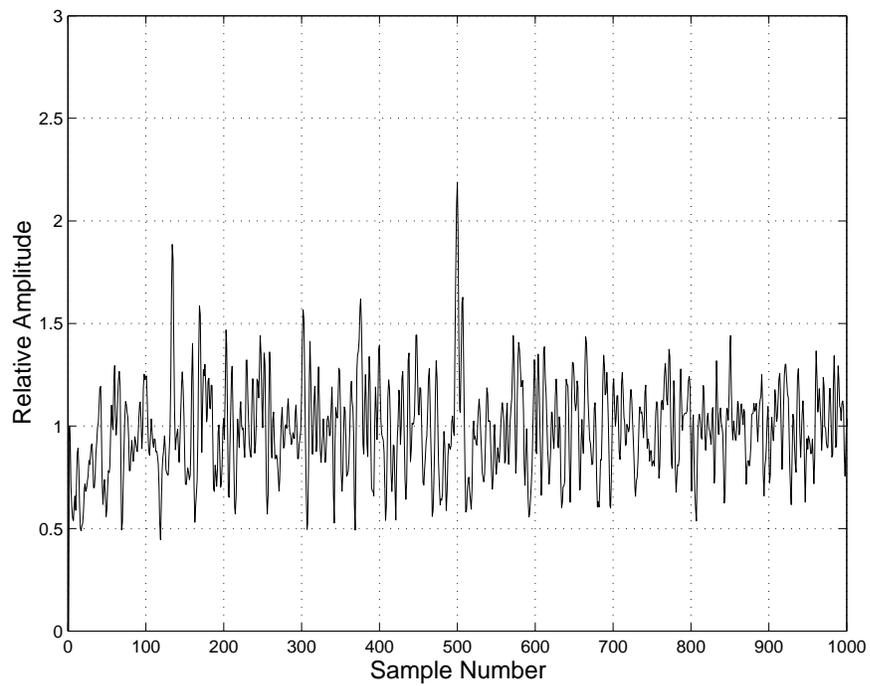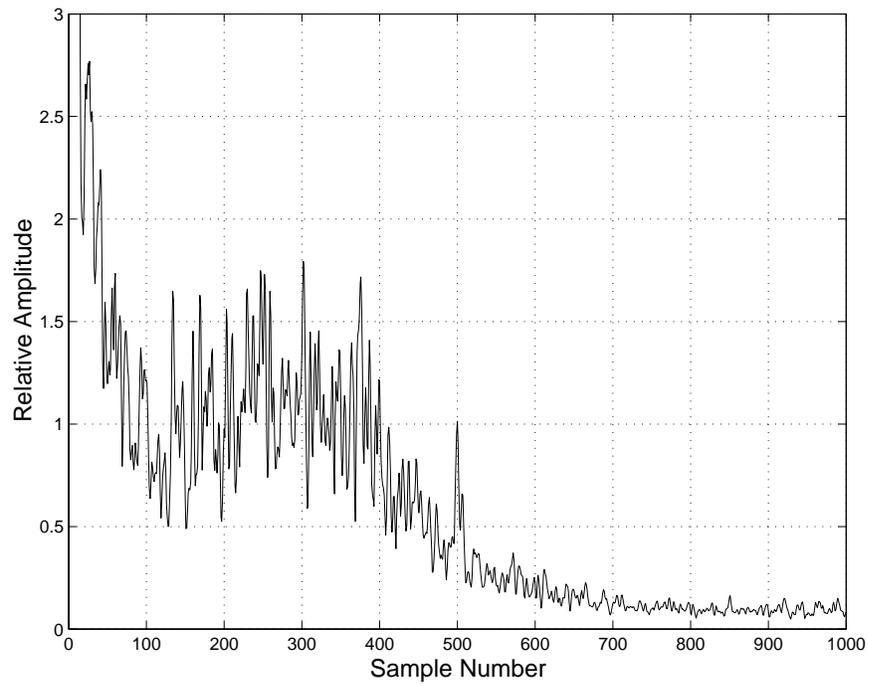
Figure 6.5. Spectral data before (top) and after (bottom) gain compensation.

100

Figure 6.6 shows the three major zones of the Greenland ice sheet: dry snow, percolation and wet snow. We made measurements over these zones and the results sare shown in Figures 6.7-6.9.
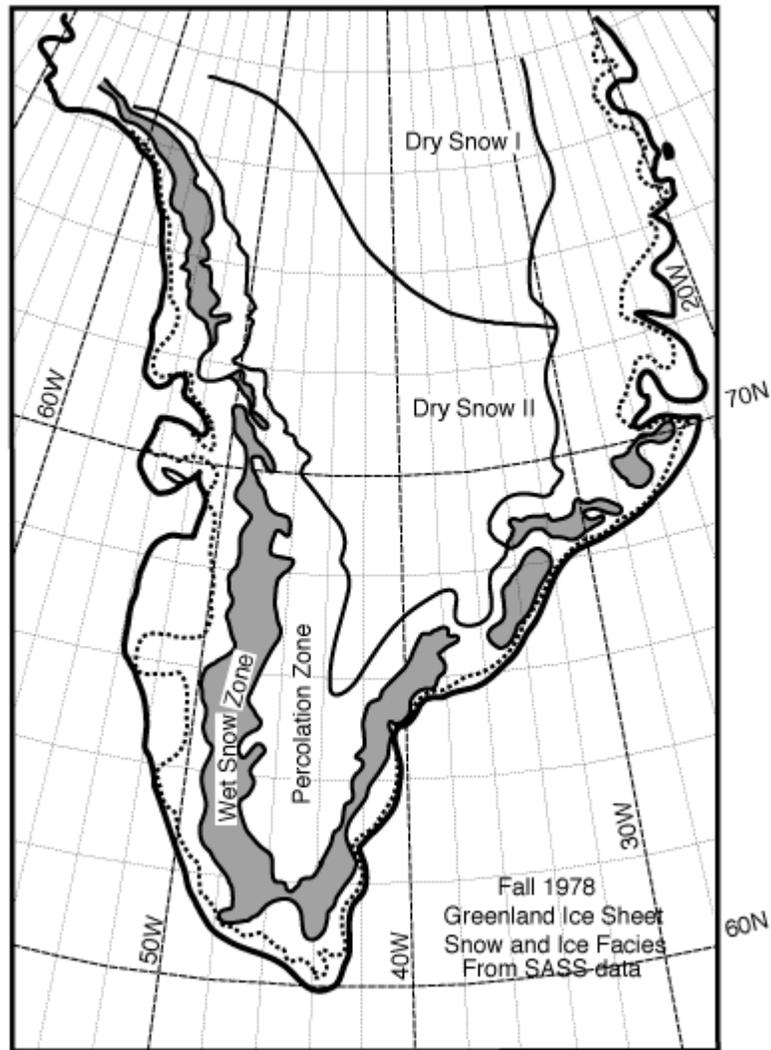
Figure 6.6. Dry snow, percolation and wet snow zones of the Greenland icesheet

[Long and Drinkwater, 1994].
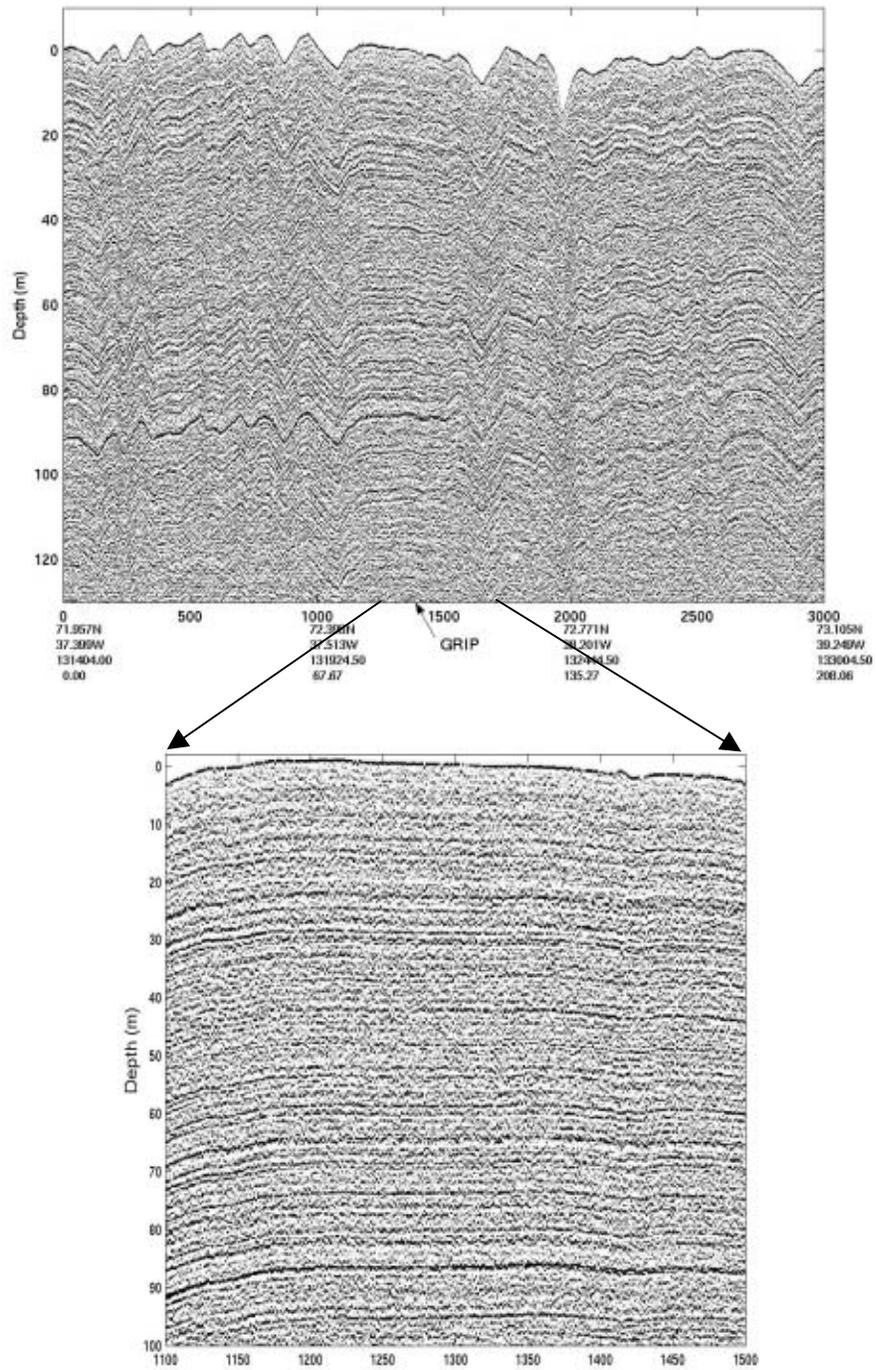
Figure 6.7. Internal layers observed at the GRIP camp, which is located in the dry snow region of the icesheet.

Figure 6.7 shows a 208 km flight line over the GRIP camp. The GRIP camp is located at 72° 35' N, 37° 38' W in the dry snow region of the ice sheet. The dry snow zone is defined as the region where there is negligible melting or percolation [Benson, 1962]. The depth shown in the figure has been corrected for variation in the velocity of the electromagnetic wave due to the non-uniform density. The layers in this region are very well defined and can be observed up to a depth of 130 m, which is more than our design goal of 100 m. We have enlarged a portion of the figure to show the excellent delineation of the layers in the GRIP region. The resolution of our measurements is less than a meter.
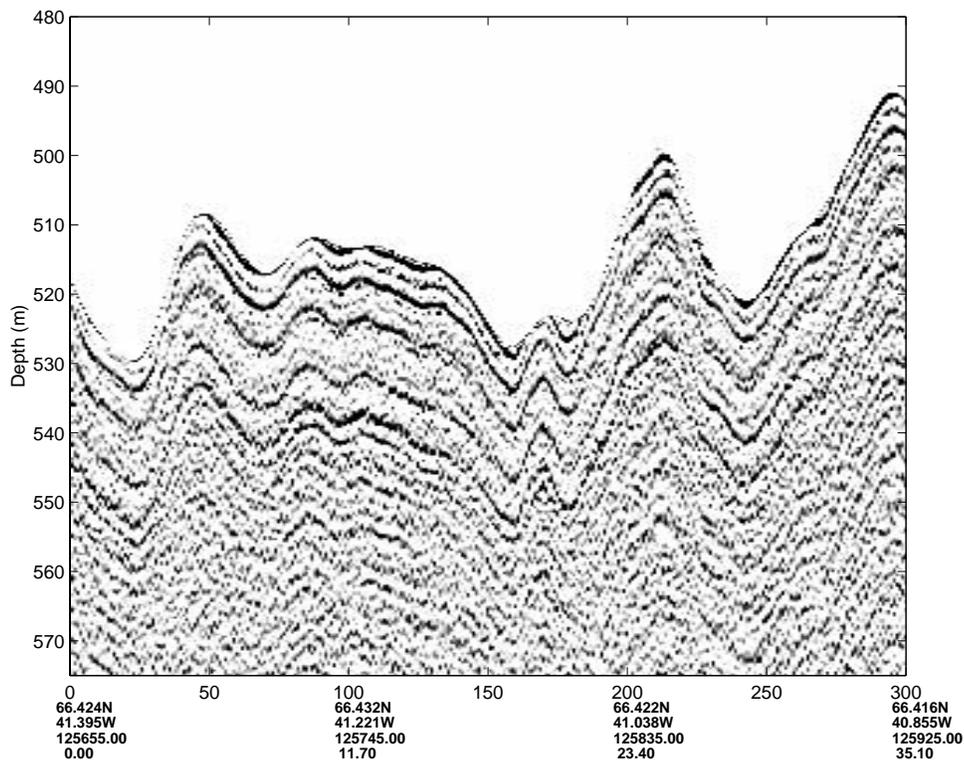
Figure 6.8. Internal layers observed at the percolation zone of the icesheet.

The layers that are observed in Figure 6.8 are from the percolation region of the ice sheet. This area is characterized by meltwater percolating into the snowpack. The depth shown on the figure is relative to the height of the aircraft, as we do not have density data in this region to correct for the velocity of the wave. There are only a few layers that can be observed here compared to the dry snow region. This is due to the existence of meltwater, which makes the medium lossy. Also, the meltwater often refreezes in the snowpack, creating a strong dielectric contrast and preventing the transmission of signals further into the ice sheet. There are several strong reflections that can be observed in the top 30 m. These reflections are probably due to the refreezing of the meltwater when transitioning from the summer to winter seasons.
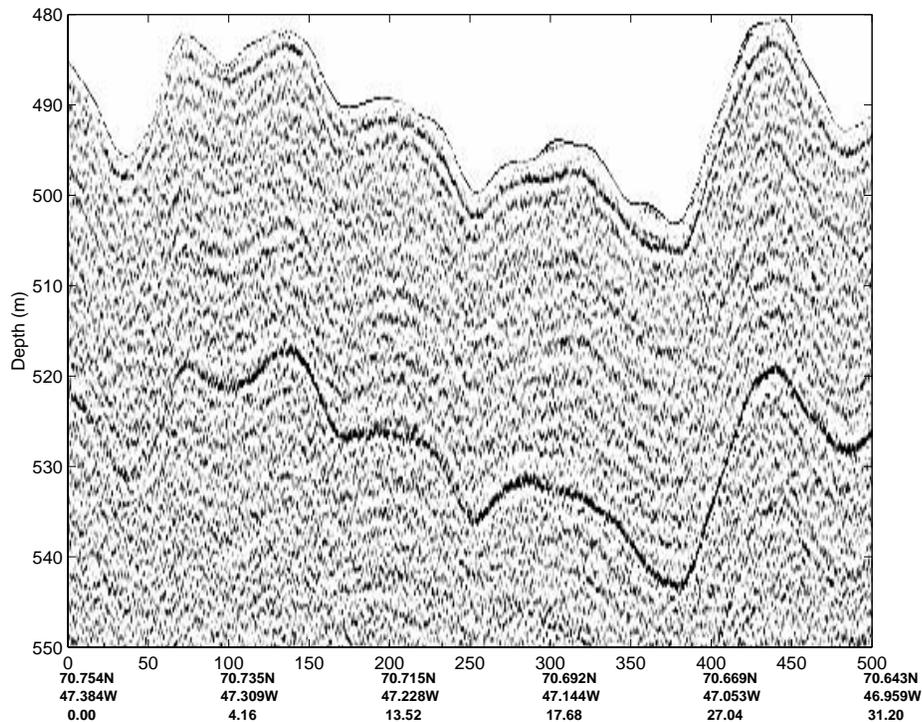
Figure 6.9. Internal layers observed at the wet snow zone of the icesheet.

Figure 6.9 shows the layers that were observed in the wet snow zone. The wet snow zone is characterized by surfaces with wet or saturated snow at a temperature of 0° C. Again, the depths are plotted relative to aircraft height since density data are unavailable in this region. As expected, there are very few layers that can be observed since penetration of the waves is severely limited by the presence of wetness on the surface. However, we do observe a strong reflection at about 35 m below the surface, which could be from a dense ice firn. We are also able to observe layers to a depth of about 50 m. However, they are not as clearly defined as those in the dry snow zone because these data were collected when the system was not well tuned.

6.4 Evaluation of Prototype System

The results from our measurements show that it is indeed possible to map the near-surface internal layers using an airborne radar system. We believe that the quality of the data can be further improved by addressing some of the problems that we discovered with the system during the test flights. The airborne system was initially designed to operate in the step-pulse mode, where the received signal would be digitized directly in two channels [Eakin, 2001]. One channel would have a high gain for the weaker returns from within the ice, and the second channel would have a low gain to receive the strong signals from the antenna feed-through and near-surface reflections.

However, because the digital system failed two weeks before the experiment, we had to redesign and reconfigure the entire system to operate in FM-CW mode.

The maximum sampling rate for digitizing the received signals from a maximum range of 800 meters was 16 MHz. The existing digital system was capable of sampling at 50 MHz rate, which was the reason for configuring the radar to operate in FM-CW mode. Reconfiguring the system over a period of two weeks resulted in a system that was less than optimum and needed frequent repairs and adjustments in the field.

Leakage from the transmit antenna to the receive antenna was a severe problem in FM-CW systems since it reduced the sensitivity of the radar. We used a fourth-order band-pass filter [Wong, 2001] to suppress the antenna feed through. This band-pass filter was not thoroughly evaluated, in particular its transient behavior, before going to the field, and we discovered in the field that the filter's large settling time resulted in ringing that saturated the amplifiers. We constructed a simple high-pass filter in the field and reduced amplifier gain to solve this problem. This reduced radar sensitivity. In summary, the following problems were identified with our prototype system:

1) Transient response of the band-pass filter following the mixer. The filter transient response was not optimized to minimize ringing. The overshoot resulting from filter ringing caused amplifier saturation.

2) Inadequate isolation between transmitter and receiver sections of the radar.

3) Insufficient receiver dynamic range. To minimize ringing we replaced the four-pole band-pass filter with a single-pole high-pass filter, which resulted in lowering the attenuation of the antenna feed-through signal.

4) Inadequate knowledge of the level of antenna feed-through signal. We did not have the opportunity to determine the isolation between transmit and receive antennas before the experiment in Greenland.

In the following chapter, we will show simulations of the band-pass filter response and the improved filter design. During our return flight, we measured the S-parameter of the antenna feed through using a network analyzer. This measurement is used in our simulations so we can optimize the filter design to suppress the antenna feed through. The packaging of the system is also improved to isolate the transmitter, receiver and IF sections better.

6.5 Summary

This chapter described the design of a prototype airborne system to map the near-surface internal layers of the Greenland ice sheet. We described the experiments that were carried out during the May 2001 field season and showed results from three distinct regions on the icesheet, namely the dry snow, percolation and wet snow regions. The excellent delineation of the layers that were observed with our system demonstrates that we can indeed map the near-surface internal layers with an airborne

radar system. We identified the problems with the system and these will be addressed

in the next chapter.

Chapter 7

AN IMPROVED AIRBORNE SYSTEM

In the previous chapter, we described some of the problems we had with the airborne system during data collection in May 2001. In this chapter, we will describe the system improvements made to solve these problems. We will show the results of system simulations that were carried out on EEsof® and compare them with laboratory measurements of the system. We could not test the system with antennas at the University of Kansas due to interference from television stations that were operating in the same frequency band. We developed a target simulator to enable us to test the system under conditions similar to those of airborne measurements over the ice sheet. The target simulator was designed with the aid of EEsof® and constructed using optical and microwave delay lines to generate the effects of antenna feed through, return from air-firn interface and returns from the internal layers.

7.1 System Description

Figure 7.1 shows the improved radar design. There were several changes made to the system from the prototype design. The 1 GHz clock is now used directly to upconvert the 100-400 MHz signal to 600-900 MHz. This is accomplished by taking the lower sideband of the upconverted signal. We have eliminated the divide-by-two circuitry needed to upconvert the chirp signal. Aside from reducing the number of components that were used to generate the 600-900 MHz chirp, this did

not result in any additional improvements in system performance. A band-pass filter is used to reject the upper sideband and leakage signals from the 100-400 MHz chirp and 1 GHz clock. The signal from the upconverter is then amplified to an appropriate level to drive the power amp. A portion of this signal is coupled to the local oscillator port for the mixer to downconvert the received signal to IF. The power amplifier amplifies the transmit signal to 2 W before it is attenuated to 1 W by a 3-dB attenuator. The attenuator reduces any mismatch between the amplifier output, the band-pass filter and the antenna. The signal is then propagated to free space via a band-pass filter and a TEM horn antenna. The band-pass filter serves to reject all out-of-band components before transmission.
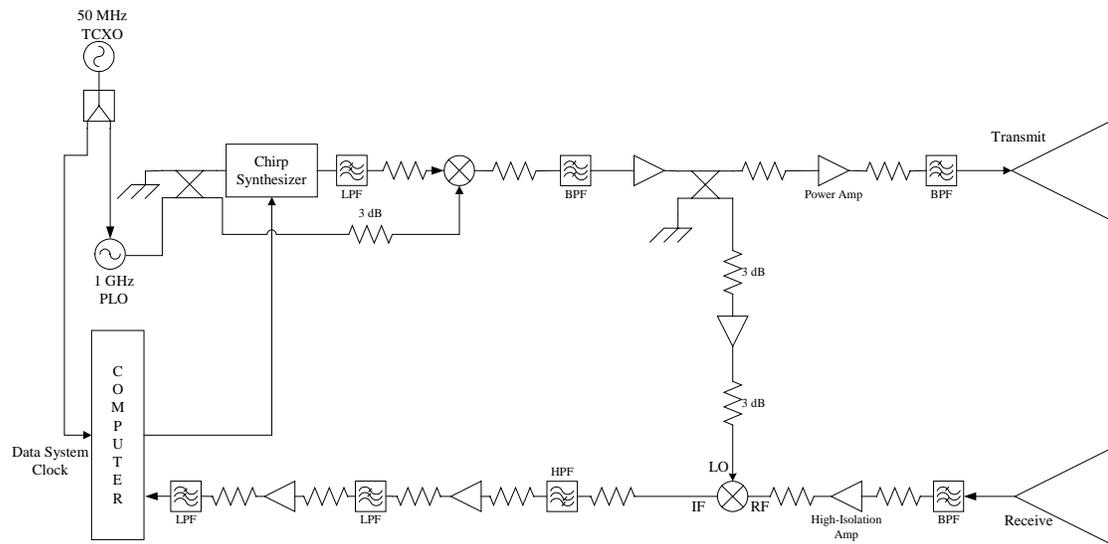
Figure 7.1. Block diagram of improved airborne radar system.

The receive signal is filtered to ensure that no out-of-band signal is coupled into the receiver since strong signals can saturate the receive amplifier and reduce the

sensitivity of the system. A low-gain (10 dB), high-isolation amplifier, which has 50-dB of reverse isolation, is used as the first-stage amplifier. We require a low gain at this stage since the high feed-through signal from the transmit antenna will saturate the mixer if higher gains are used. The high reverse isolation reduces the local oscillator signal coupled into the RF port of the mixer being transmitted via the receive antenna. The received signal is downconverted to IF. The IF signal is filtered using a third-order Gaussian high-pass filter to attenuate the antenna feed through. During last year's field season we noted that the antenna feed-through signal appeared at 500 kHz. The high-pass filter is designed to attenuate this leakage signal by 60 dB with a fast settling time. An amplifier with a medium-high output power (20 dBm) is used to amplify the IF signal. We require a fairly high output to avoid saturation by the upper sideband signal that is generated during the mixing process. The signal is then low-pass filtered to reject the upper sideband signal and the LO leakage signal. The IF signal is further amplified to use the full A/D dynamic range. The signal is finally filtered with an anti-aliasing filter to keep the input noise from folding over into the desired IF range.

7.2 Design of an Optimum High-pass Filter

During the last field season we noticed that the antenna feed-through signal was saturating the IF amplifiers even though a fourth-order band-pass signal was placed between the mixer and the first IF amplifier to suppress this signal. As explained in the previous chapter, the filter's large settling time caused excessive

ringing, which saturated the amplifier. Designing an effective filter requires knowledge of the amount of rejection required at a particular frequency or range of frequencies. To find out the amount of rejection that was needed we must determine the magnitude of the antenna feed through. We did this by measuring the scattering parameters (S-parameters) between the transmit and receive antennas using a network analyzer while the aircraft was flying at its cruising altitude of ~6000 m. We time-gated the antenna feed-through signal to ensure that the measurement is not affected by any other reflection. Figure 7.2 shows the transmission parameter that we measured between the transmit and receive antennas. This measurement indicates, in the worst case, the received signal will be 31 dB below the transmitted signal. As such, since we are transmitting 30 dBm of signal power, we can expect –1 dBm at the front end of the receiver. This level is about 55 dB above the expected signal level from the air/firn interface. Thus, we would like to have about 60 dB of rejection at the frequency where the spectral component of the antenna feed through appears. The required specification for our filter is shown in Table 14.
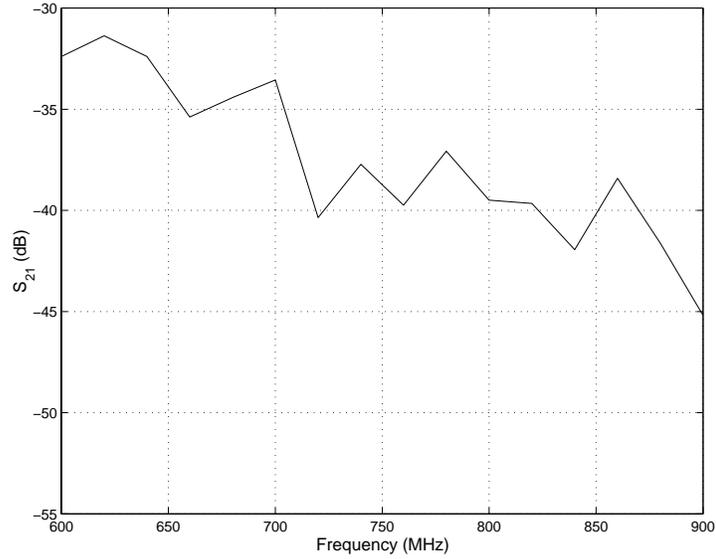
Figure 7.2. Transmission parameter (S_{21}) between the horn antennas.

Table 14. High-pass filter specifications.

Frequency (MHz)	Attenuation (dB)
0.5	60
10	3

The high-pass filter that is desired is one that settles quickly and thus provides a minimum overshoot. A class of filters known as the Gaussian filters has the ideal time-domain response with no overshoots. However, an ideal Gaussian filter requires an infinite number of elements and thus is impractical for physical realization [Dishal, 1959]. Dishal has given approximations to the Gaussian filter that can be used to build these filters.

A third-order Gaussian filter was designed and fabricated in the laboratory [Athial, 2001]. Figure 7.3 and Figure 7.4 show the comparison between the EEsof® simulation and the measured response. The measured results do meet the specifications in Table 14.
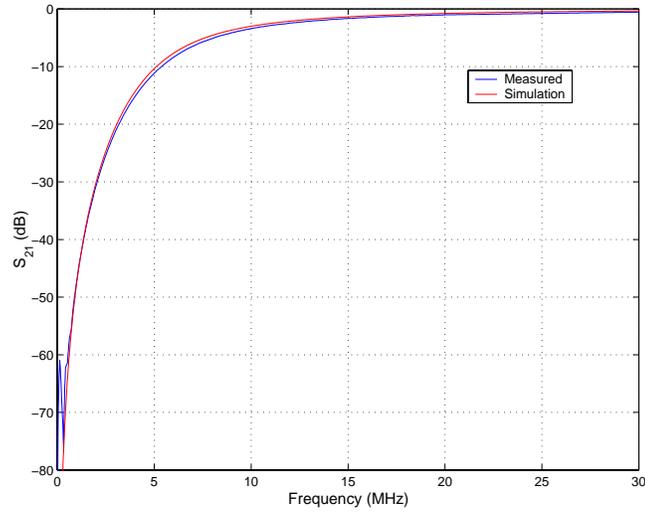
Figure 7.3. Comparison between measured and simulated response of Gaussian high-pass filter.
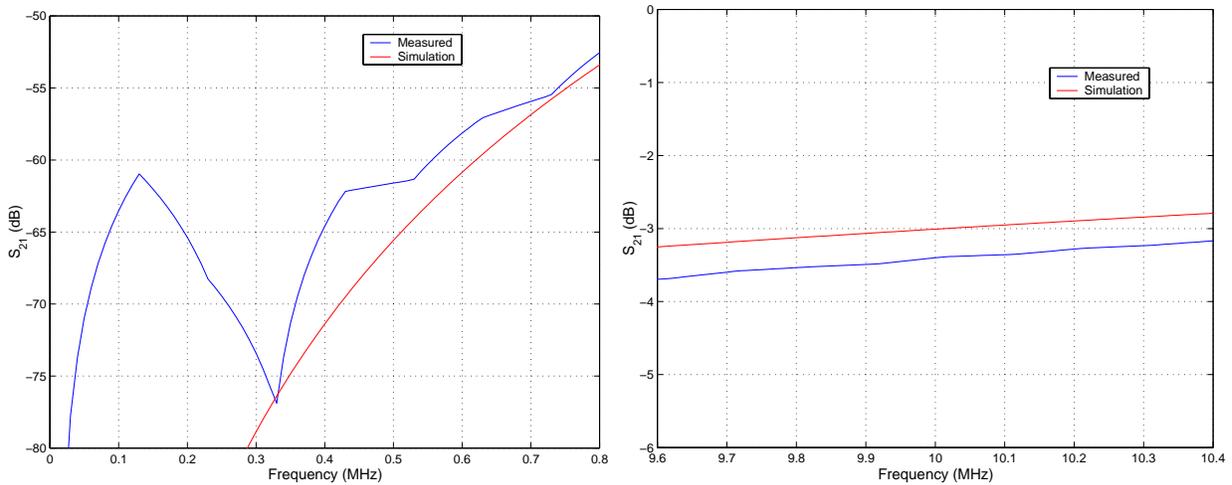
Figure 7.4. A zoom-in of the Gaussian filter's attenuation at 500 kHz (left) and 10 MHz (right).

The above figures clearly illustrate the versatility of EEsof® in simulating circuits. The match at the 3 dB cutoff at 10 MHz is only off by 0.5 dB. At 500 kHz, the frequency at which we expect the antenna leakage, we do have a 60 dB rejection. The increased mismatch between the measured and simulated response can be attributed to the uncertainty in the measurement of the signal level, since the signal-to-noise ratio is low at these levels. Figure 7.5 shows the transient response of the filter. An excellent match is again demonstrated between the simulated and measured responses.
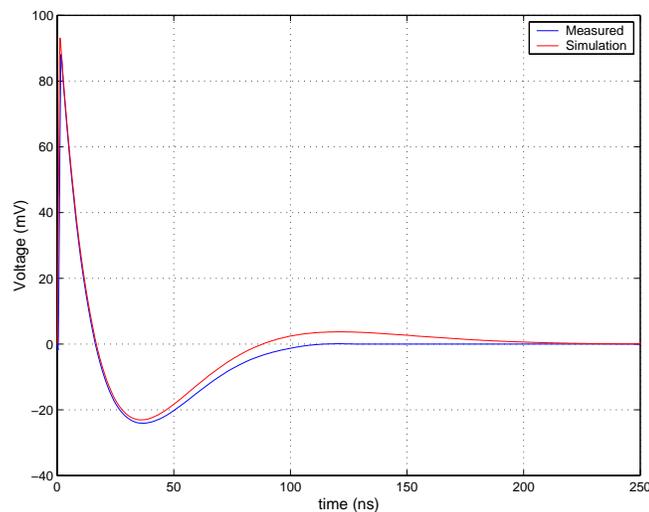
Figure 7.5. Comparison between measured and simulated responses to a 0.2 V step input.

7.3 System Simulation

To optimize the radar's performance, we used EEsof® to simulate the system response. Accurate simulations can be performed by incorporating the scattering parameter models of components that are to be used in the radar. A number of manufacturers of RF components provide S-parameter models of their parts on

websites. For components for which there were no models, we measured them in the laboratory using a network analyzer. Since we were modifying an existing system, we had most of the components we intend to use on hand. The S_{11}, S_{21}, S_{12} and S_{22} scattering parameters of the components were measured with a network analyzer, which had been interfaced with EEsof®. The interface between EEsof® and the network analyzer was accomplished using National Instrument's general-purpose interface bus (GPIB) card. The parameters are written to a file and stored on the hard drive. The scattering parameters were measured over a 30 kHz to 2 GHz frequency range. We used this wider frequency range instead of the 600-900 MHz range of our system to enable EEsof® to obtain a more accurate impulse response of the components. Further, these parameter files will be stored in a database that can be accessed by students here for future radar design.

We also digitized the output of the STEL-9949 digital chirp synthesizer to be used as the source during the simulation. The oscilloscope that was used to digitize the chirp signal had a 8 bit A/D converter. Hence the dynamic range of our simulation will be about 48 dB if the full dynamic range of the oscilloscope was used. Referring to Figure 7.1, we measured the signal at the output of the amplifier that is just before the coupler. We measured it at this point to get a better use of the oscilloscope's dynamic range.

EEsof® can model the non-linearities in the amplifiers and mixers by allowing the designer to specify the 1 dB compression and the third-order intercept

(TOI) points. These points are usually specified with respect to the output power for amplifiers and input power for mixers. The 1 dB compression point for a mixer is the input power at which the output reduces by 1 dB from the linear relationship between the input and output power levels (see Figure 7.6). The TOI point is the imaginary point at which the output level of the third-order intermodulation products would be equal to the desired output power if the device were linear. The 1 dB compression and TOI points inform the radar designer of the power levels at which to operate a device for a desired spurious free dynamic range. Further discussions and measurement techniques of these parameters can be found in Henderson [1997] and Anritsu [2000].
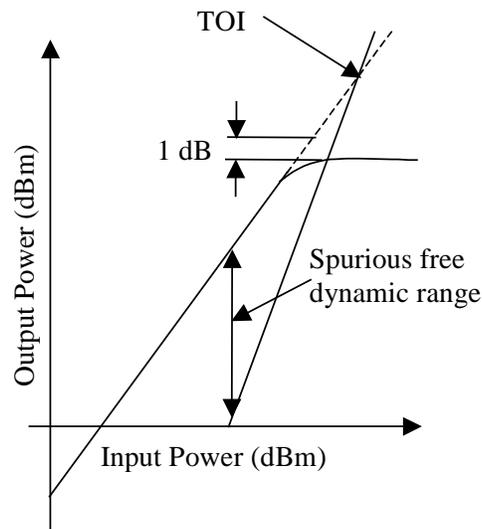
Figure 7.6. Illustration of 1 dB compression and third-order intercept points.

The system shown in Figure 7.1 was simulated in EEsof® excluding the power amplifier, which was not available at the time of simulation. Figure 7.7 shows the simulation setup in EEsof®. The transmitter, receiver and IF sections have been

117

labeled in the figure. The S-parameter of the transceivers and fiber-optic delay line were measured and used in our simulation. The cylindrical objects in the figure are called Data Access Components (DAC). RF and IF components are linked to their respective S-Parameter files via this object. The input waveform file is also accessed via this component. The simulation was carried out for 100 μs, which is the sweep duration of our radar. The time step that we used was 0.5 ns, which enables us to sample frequencies up to 1 GHz. The result of our simulation and measured response is shown in Figure 7.8.
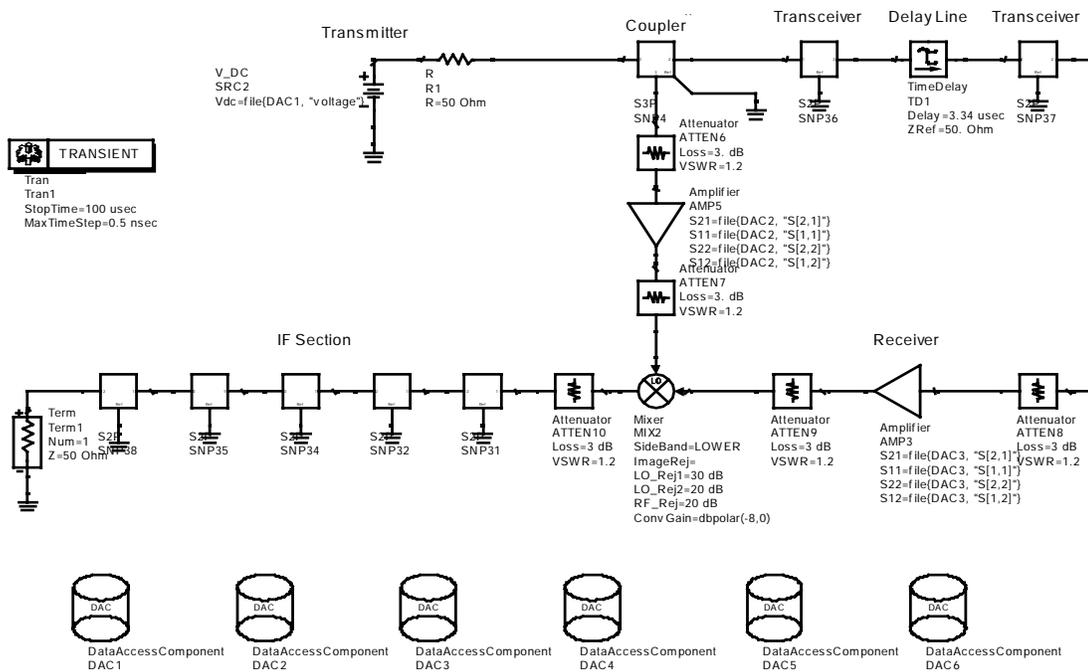
Figure 7.7. FM-CW radar system setup in EEsof®.
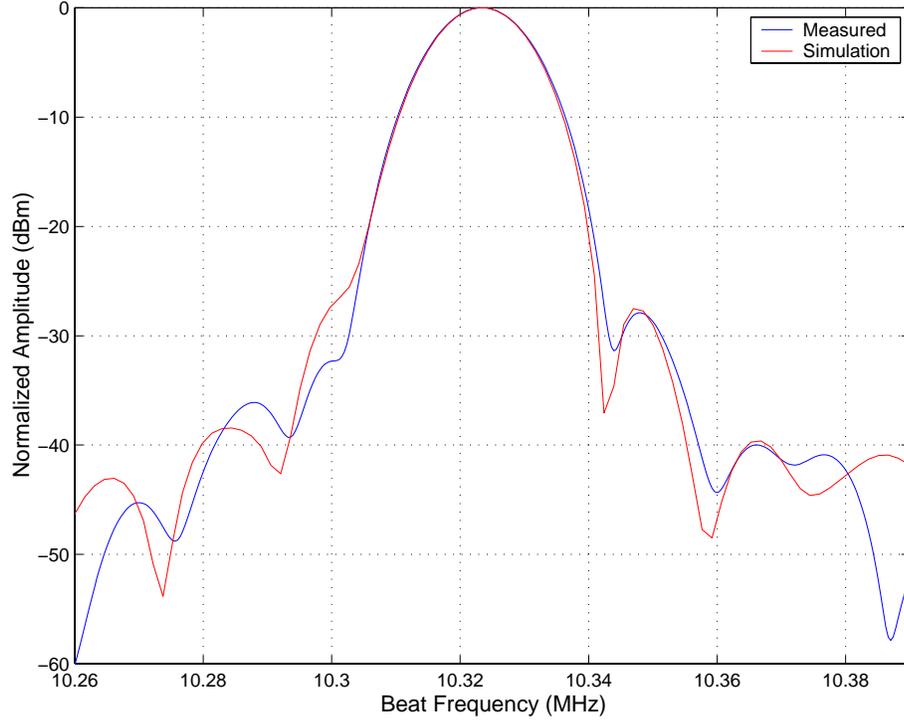
Figure 7.8. Comparison between measured and simulated delay line response.

There is an excellent agreement between the measured and simulated data for the main lobe, but there is slight disagreement between the two for sidelobes. These mismatches can be attributed to the fact that not all the adapters and cables that were used in the actual system were characterized on EEsof®. The excellent match in pulse response between the measured and simulated response will enable us to develop accurate system models and explore deconvolution techniques [Robinson and Treitel, 1980] to remove the system response from the received signal.

7.4 Target Simulator

Before the 2000 field season, we attempted to test our radar system outdoors by pointing a UHF Yagi antenna at external targets such as buildings and trees. However, interference from TV stations and cell phones operating in the UHF band prevented us from doing so. Likewise, attempts to test the radar outdoors will cause degradation in service for cell and cordless telephone users in the surrounding area. In lieu of this problem and to provide a good calibration mechanism for the radar, a target simulator was designed and developed as an undergraduate honors research project [Plummer and Pharatasarathy, 2002].

The target simulator mimics the antenna feed-through path, reflection from the air/firn interface and reflections from the internal layers. The simulator was first designed using ideal components in EEsof®. Figure 7.9 shows the EEsof® simulation setup along with an illustration of the aircraft and the various paths that are being simulated. The color codes map the paths being simulated to the components that simulate the path. The green path simulates the antenna feed-through signal. We used a semi-rigid microwave delay line of 167 ns to match the actual path length. The blue path simulates the 1000 m two way path length between the aircraft and the air/firn interface. This was simulated using a fiber-optic delay line with optical/RF transceivers to interface the RF and optical sections. Fiber-optic cables are ideal for simulating large path lengths due to its low loss, small size and light weight. The yellow path simulates the multitude of reflections from layers within the ice. This was

accomplished using a feedback loop. A short cable was used in this path to simulate

the 0.5 m spacing between the reflections from the internal layers.
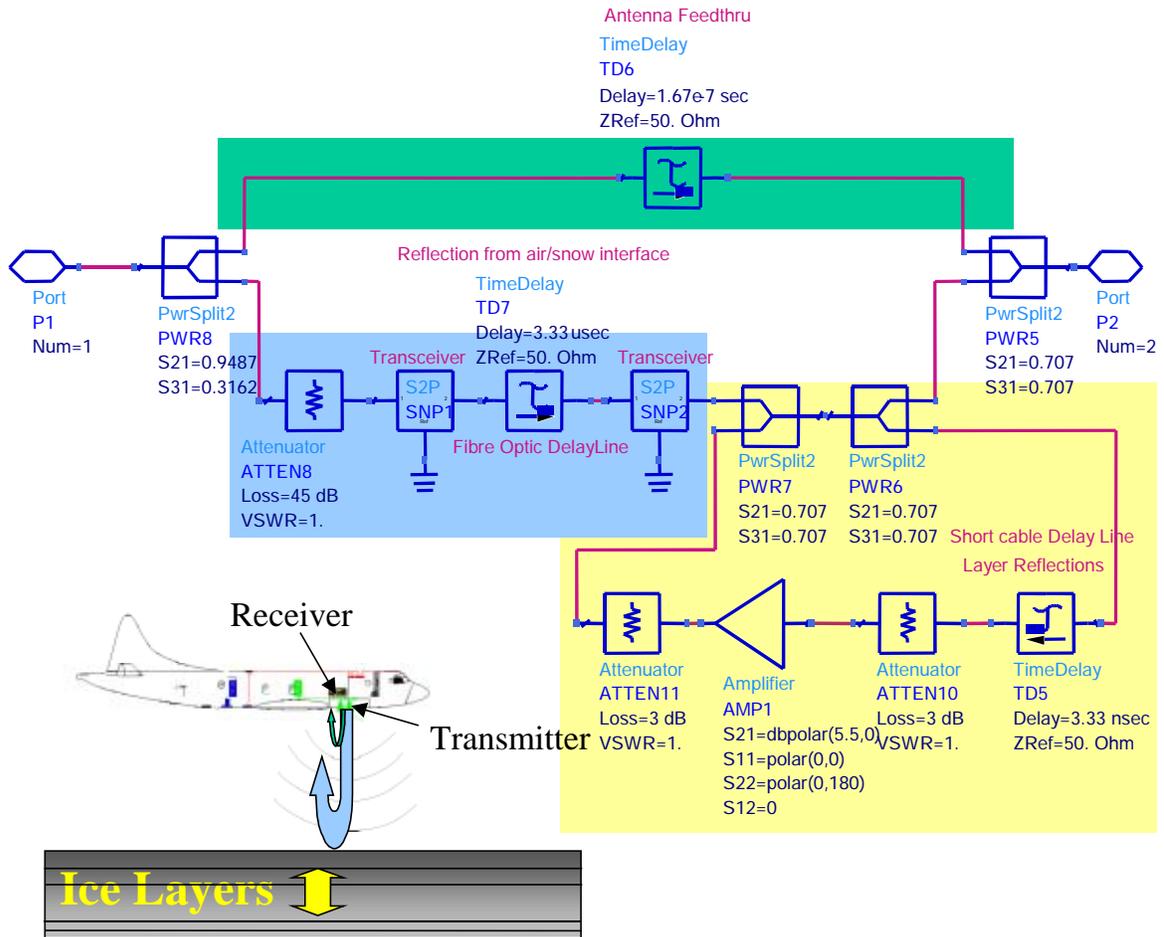
Figure 7.9. Block diagram of target simulator and the effects that are being simulated.

Once the component parameters were optimized, off-the-shelf components

were purchased. The scattering parameters of these components were measured using

a network analyzer and simulated in EEsof®. The simulator was constructed in the

laboratory and the overall response of the system was measured using a network analyzer. The simulation result is compared with the measured response in Figure 7.10.
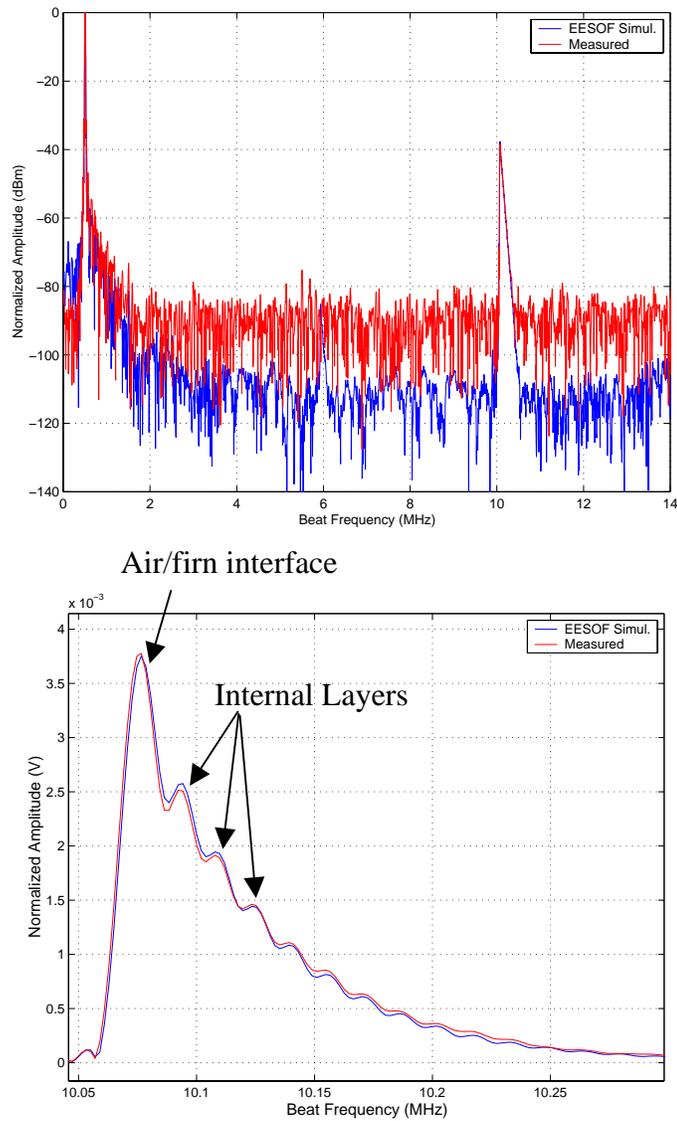
Figure 7.10. Comparison between simulated and measured response of target simulator.

The top figure shows the reflection profile for the entire path. The first signal represents the antenna feed-through signal, which is about 40 dB above the air/firn interface. The 40 dB difference can be easily adjusted to suit the field conditions by changing the attenuator that is located just before the input transceiver. The signals following the antenna feed through are the reflections from the air/firn interface and from the internal layers. We clearly see the excellent match between the measured response and the EEsof® simulation in the zoomed figure below.

The FM-CW radar system that we constructed was tested with the target simulator and the results are shown in Figure 7.11.
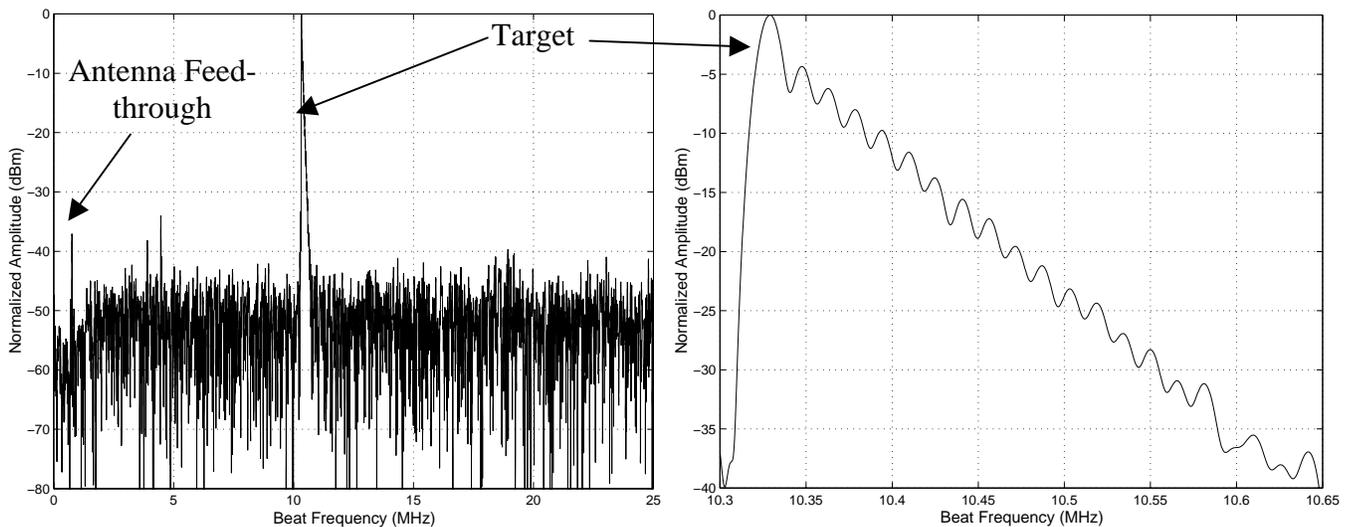
Figure 7.11. Results of FM-CW radar test with target simulator.

The results show excellent suppression of the antenna feed through. The antenna feed through was 40 dB above the target response before the IF section. The final output is 40 dB below the target response. The 80 dB suppression is due to the

60 dB rejection by the Gaussian filter and an additional 20 dB suppression by the DC blocks in the amplifiers. The bottom figure shows excellent resolution of the layering that we are able to observe with the simulator.

7.5 Isolation

To provide better isolation between the transmitter, receiver and IF sections, we constructed a box that partitions and shields these sections. We constructed two boxes. Part of the transmitter and receiver were placed in the second box and will be placed in a rack right above the horn antennas that are located in the bomb bay. This will shorten the path length between the transmit and receive antenna and push the antenna feed through further into the stop band. Low-loss cables are used to connect the transmit and receiver sections mounted in the rack to the transmit and receive antennas, respectively. Figure 7.12 shows how the various sections are isolated from each other. Box 1 will be located at the rack mount and Box 2 will be located close to the antennas above the bomb bay. We also replaced the low quality cables that were used last year with high-isolation RF cables, which provide more than 100 dB of isolation.
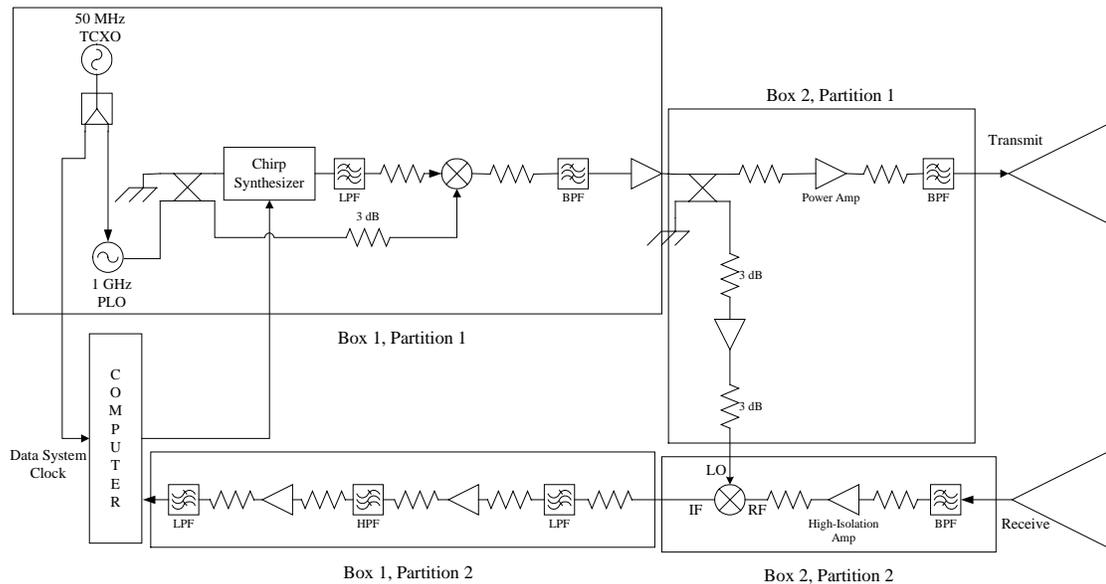
Figure 7.12. Isolating the transmit, receive and IF sections.

7.6 Summary

In this chapter, we described the improvements that were made to the prototype system. We addressed the problem of filter ringing that was saturating the amplifier during the last field season by designing a Gaussian high-pass filter with very fast settling time and little overshoot. We addressed the lack of isolation by building two boxes to shield transmit, receive and IF sections from each other. We placed the front end of the transmitter and receiver near the antennas to reduce the path length between the two and thus push the antenna feed through further into the stop band. We performed EEsof® simulation on the system and showed an excellent match between the measured and simulation response for a delay line test. We constructed a target simulator, which mimics the antenna feed-through, air/firn

reflection and reflections from within the firn. The target simulator was also designed with the aid of EEsof® and excellent match was again achieved between simulation and measured responses. We tested our improved system with the target simulator, and the results show that we are able to suppress the antenna feed through and obtain excellent layering details. We believe our radar has been improved by an order of magnitude and we expect the quality of the data from the upcoming field experiment to be similarly superior to the results obtained from the previous year.

Chapter 8

SUMMARY AND RECOMMENDATIONS

Accumulation rate of the polar ice sheets is an important parameter that is required for mass balance computation of the ice sheet. The present accumulation map has relatively large uncertainty in many areas due to sparse sampling in these regions. Accumulation rates are currently determined using ice cores and pits. Ice core retrieval is an expensive, tedious and, at times, dangerous process. It is thus prudent to seek remote sensing techniques to assist in the interpolation between ice core data to reduce the uncertainty associated with the sparse sampling. The crux of this dissertation was to explore the feasibility of employing a high-resolution airborne radar to map the near-surface isochronous layers in the Greenland ice sheet. We have shown that it is indeed possible to map the near-surface internal layers with high resolution from an aircraft. We present below a summary of the work that was done to arrive at an operational airborne radar that is ready for routine measurement of internal layers over the polar ice sheets.

In Chapter 3, we looked at the factors that cause dielectric discontinuities within the ice sheet. The primary cause of discontinuities at the near surface of the firn is density changes. These density changes in the dry snow zone are due to pressure exerted by annual accumulation of snow over the firn. Mapping of these layers is the primary aim of this work. The other causes of dielectric discontinuities

are those due to changes in conductivity and crystal orientation. The conductivity changes are usually due to acidic deposits from volcanic eruptions. Major volcanic eruptions such as the Laki in 1783 and Tambora in 1815 are often used for absolute dating of deeper ice cores. Changes in crystal orientation fabrics have been attributed to shear strain along isochrones. They, however, occur at depths where there are no density changes and hence are of little interest to our work since we are only interested in the near-surface reflections. We used the transmission line model in the CAD tool EEsof® to determine the reflection coefficients that can be expected for discontinuities due to air/firn interface and those due to conductivity changes.

In Chapter 4, we applied surface and volume scattering models to observe the off-nadir backscatter due to finite beamwidth of the horn antennas in the cross-track direction. These backscatter signals have the potential for masking the reflections from internal layers. We computed the reflection coefficient due to density changes from an ice core record at the NGRIP site and compared it to that due to surface and volume scattering. The physical parameters for the surface-scattering and volume-scattering models were obtained from published data in the dry snow zone. Our results showed that the reflections from the internal layer were about 10 to 15 dB and 5 to 10 dB above the surface clutter at 600 MHz and 900 MHz, respectively. The volume scattering was 15 dB below that due to surface scattering and thus has little effect on the return from internal layers.

Based on the results of simulations in Chapter 3, we described in Chapter 5 the design of a surface-based ultra-wideband FM-CW radar system that operates from 170 to 2,000 MHz. The purpose of the surface-based system was to determine the optimum frequency range for mapping the internal layers. This system was tested during the 1998 and 1999 field seasons at NGRIP. We showed that we were successful in mapping internal layers up to a depth of almost 300 m. A number of the layers were identified to within ±2 m of the layers obtained from ice-core data. We computed the accumulation rate based on the radar mapping of the layers and determined its uncertainty to be around 4%. We also analyzed the frequency content of a signal reflected from a layer within the firn. The results showed that the optimum frequency range for operating our radar is from 500 to 1,000 MHz.

In Chapter 6, we described the design of a 600-900 MHz airborne radar. The frequency was selected such that it did not interfere with communication and navigational equipments onboard the aircraft. Two TEM horns were installed adjacent to each other in the bomb bay of the aircraft to serve as the transmit and receive antennas. The system was initially designed to operate in the chirped and stepped-frequency pulse modes to avoid the problem of antenna feed through. The digital system that was being developed to accommodate these modes, however, failed two weeks before the experiment and hence we reverted to a FM-CW operation to use with the existing digital system. The band-pass filter used to suppress the antenna feed through had a large settling time that resulted in ringing and saturation of the IF amplifiers. We designed a single-pole high-pass filter in the field to avoid

the ringing and this, in turn, meant that we had to reduce the amplifier gain and thus produced less sensitivity. During our return flight from the field, we measured the isolation between the transmit and receive antenna with a network analyzer to aid us in the design of a better IF filter for the new system. During the experiment we also noted that there was inadequate isolation between the transmit and receive sections of the radar.

Chapter 7 described the design of an improved FM-CW radar system for routine mapping of internal layers over the Greenland ice sheet. The CAD tool EEsof® was used to design and optimize the system performance before construction. A third-order Gaussian high-pass filter was designed to provide the desired rejection while minimizing the ringing effect. The entire system was simulated on EEsof® and this performance was compared with delay-line measurements made with the actual system. An excellent match was obtained between the two mainlobes and first sidelobe. The slight mismatch in distance between the minor reflections can be attributed to the fact that not all the adapters and cables that were used in the actual system were characterized on EEsof®. During the last field season, we had difficulties testing our system with antennas due to interference from communication equipment operating in the UHF band. To enable us to test the radar system effectively, a target simulator was designed as an undergraduate honors research project. The simulator was constructed using RF and optical delay lines with a RF/optical transceiver to interface the RF and optical sections. The target simulator was designed to simulate the antenna feed-through signal and reflections from the

air/firn and internal layers. The multiple internal layers were generated by means of a feedback loop using a short cable. We tested our new system with the target simulator and obtained the desired suppression of the antenna feed through. The multiple layers were observed to be very well defined. We constructed boxes with partitions to shield the transmitter, receiver and IF sections adequately. The front end of the transmitter and receiver were placed in a separate box to be positioned close to the bomb bay where the antennas are located. This serves to shorten the path length between the transmitter and receiver and hence push the antenna feed-through signal further into the stopband of the high-pass filter.

Our system sensitivity improved by an order of magnitude and is ready for routine mapping of internal layers over the polar ice sheets. The current system is optimized for data collection over the dry snow region where the surface is not as rough as in the percolation and wet snow zones where surface clutter could pose a problem. We showed that we were able to map up to about 50 m in these regions even with a sub-optimum system. However, if deeper layers need to be observed in these regions or if weak reflections from volcanic layers need to be tracked, we will need to implement a clutter cancellation scheme. There are a couple of ways this can be done. The following section discusses some techniques that are worth considering.

8.1 Digital Beamforming to Null Clutter

To improve the resolution in the cross-track direction we recommend that the TEM horn antennas be replaced with an array of bow-tie antennas as shown in Figure

8.1. In addition, the array could be implemented such that beamforming [Steyskal, 1987] can be performed to null out clutter that is masking reflection from a layer of interest. Figure 8.2 shows how the null is placed to enable detection of the internal layer.

In beamforming, the amplitude and phase of each stick of the bow tie will be recorded. In traditional beam-steering arrays, only the phase is manipulated to steer the beam. However, amplitude and phase control will enable us to better manage the side lobe levels and steer the nulls. Each stick can be weighted appropriately with complex weights (amplitude and phase) to produce a pattern that nulls out the clutter that masks the desired return.
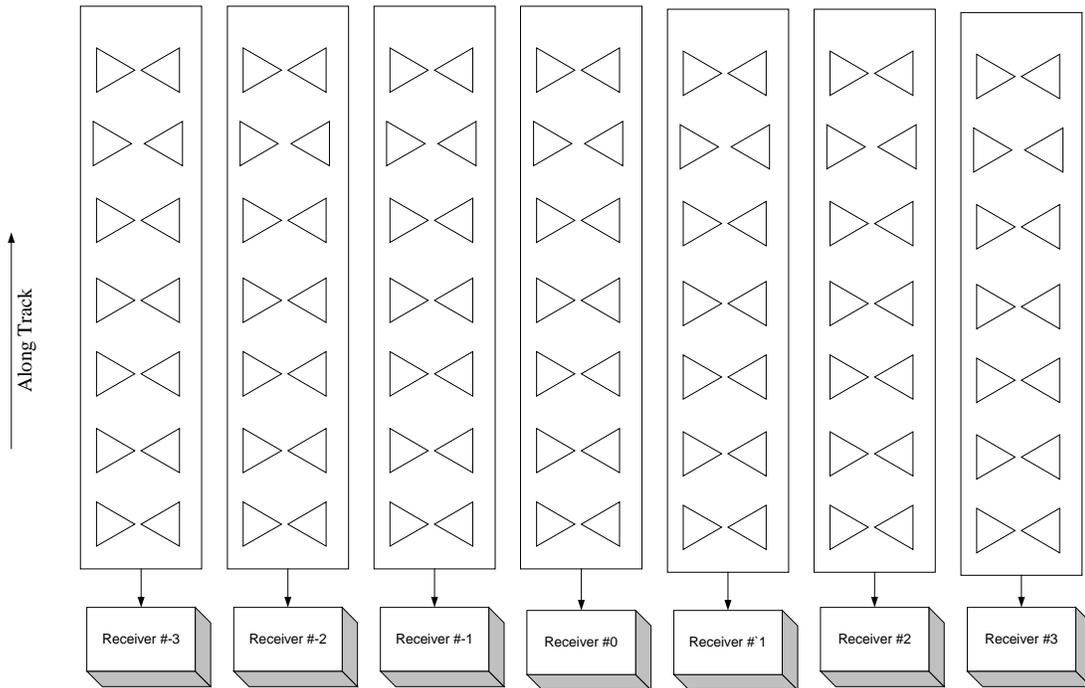
Figure 8.1. Bow-tie array to form beams digitally.
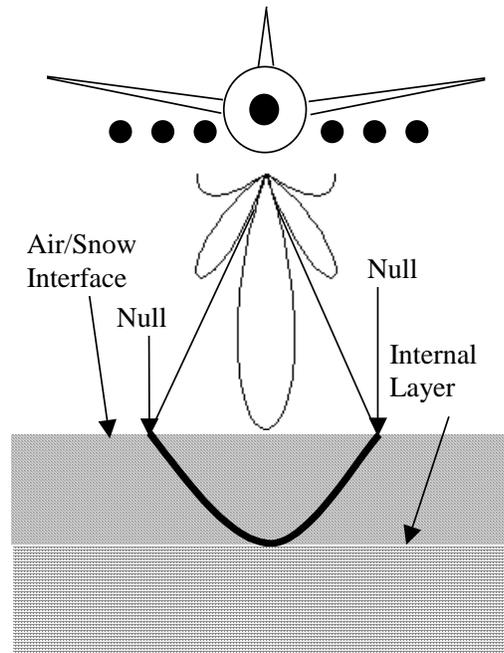
Figure 8.2. Digital beamforming to null out undesired clutter.

8.2 Model-Based Signal Processing

Model-based signal processing (MBP) has been used extensively in sonar for detection of acoustic sources [Candy, 2000]. MBP uses noise, system and propagation models to generate the expected signature from a target (Figure 8.3). The noise model consists of the uncertainty in the model parameters, interference signal, etc. The propagation model contains a priori information about the firn. We can use data from ice cores to generate the propagation model. We can also include surface and volume characteristics of the firn in this model to estimate the effects of clutter. We can generate the system model using CAD tools such as EEsof® or by calibrating the radar with known targets. It would be better to obtain an external target for calibration

so antenna effects are also included in the model. We can first compare the measured

surface return with that from the simulated response. The model parameters can then

be adjusted to fit the measured data. Once a match is achieved, we can subtract the

surface return from the measured data to reveal the internal layer data that can be seen

be our radar. We can then iteratively subtract each layer until the radar response for

all the layers that can be observed by the radar are obtained.

Raw Data

Firn Model

Noise Model

System Model

Estimate
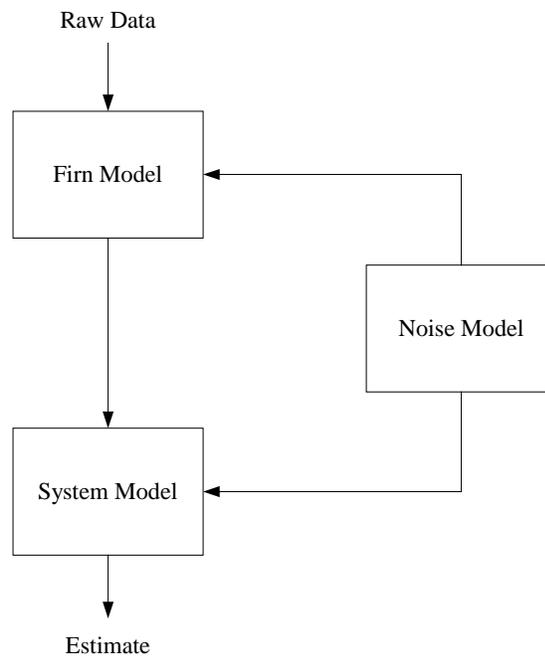
Figure 8.3. Model-based signal processing.

REFERENCES

Agilent Technologies, Advanced Design System 2001, http://www.agilent.com/eesof-eda/, 2001.

Akins, T., Design and Development of an Improved Data Acquisition System for the Coherent Radar Depth Sounder, M.S. Thesis, Electrical Engineering and Computer Science, The University of Kansas, Lawrence, KS, 1999.

Anritsu, Intermodulation Distortion (IMD) Measurements Using the 37300 Series Vector Network Analyzer Application Note/GIP-G, Morgan Hill, California, 2000.

Athial, G., Private communication, Lawrence, KS, 2001.

Bailey, J. T., S. Evans, and G. de Q. Robin, Radio echo soundings of polar ice sheets, *Nature*, vol. 204, pp. 420-421, 1964.

Bales, R. C., J. R. McConnell, E. Mosley-Thompson, and G. Lamorey, Accumulation map for the Greenland ice sheet: 1971-1990, *Geophysical Research Letters*, vol. 28, no. 15, pp. 2,967-2,970, 2001a.

Bales, R. C., J. R. McConnell, E. Mosley-Thompson, and B. Csthao, Accumulation over the Greenland ice sheet from historical and recent records, *Journal of Geophysical Research*, vol. 106, no. D24, pp. 33,813-33,826, 2001b.

Benson, C. S., Stratigraphic Studies in the Snow and Firn of the Greenland Ice Sheet, Research Report 70, US Army Cold Regions Research and Engineering Laboratory (CRREL), Hanover, NH, 1962.

Bogorodsky, V. V., V. I. Pozdnyak, G. V. Trepov, and A. M. Shremet'yev, Radar sounding measurements of the thickness of annual snow strata in the

Antarctic, *Doklady Akademii Nauk SSSR* [Trans.: *Doklady of the Academy of Sciences of the U.S.S.R. Earth science sections*.], vol. 264, no. 4, pp. 909-911, 1982.

Bogorodsky, V. V., C. R. Bentley, and P. E. Gudmandsen, *Radioglaciology*, D. Reidel, Dordrecht, Holland, 1983.

Candy, J. V., Model-based signal processing in the ocean, *Oceanic Engineering Society Newsletter,* vol. 35, no. 3, 2000.

Cheng, D. K., *Field and Wave Electromagnetics*, 2nd ed., Addison-Wesley, Reading, MA, 1989.

Clausen, H. B., Private communication, NGRIP, Greenland, 1998.

Cumming, W. A., The dielectric properties of ice and snow at 3.2 centimeters, *Journal of Applied Physics*, vol. 23, no. 7, 1952.

Dahl-Jensen, D., N. S. Gundestrup, K. Keller, S. J. Johnsen, S. P. Gogineni, C. T. Allen, T.S. Chuah, H. Miller, S. Kipfstuhl, and E. D. Waddington, A search in north Greenland for a new ice-core drill site, *Journal of Glaciology*, vol. 43, no. 144, pp. 300-306, 1997.

Davis, C. H., C. A. Kluever, B. J. Haines, C. Perez, and Y. Yoon, Improved elevation change measurement of the southern Greenland ice sheet from satellite radar altimetry, *IEEE Transactions on Geoscience and Remote Sensing*, vol. 38, no. 3, pp. 1367-1378, 2000.

Dishal, M., Gaussian-response filter design, *Electrical Communication*, vol. 36, no. 1, pp. 3-26, 1959.

Dyurgerov, M. B., and M. F. Meier, Year-to-year fluctuations of global mass balance of small glaciers and their contribution to sea-level changes, *Arctic and Alpine Research*, vol. 29, no. 4, pp. 392-402, 1997.

Eakin, R. K., Design and Development of a One Gigasample per Second Radar Data Acquisition System, M.S. Thesis, Electrical Engineering and Computer Science, The University of Kansas, Lawrence, KS, 2001.

Ellerbruch, D. A., and H. S. Boyne, Snow stratigraphy and water equivalence measured with an active microwave system, *Journal of Glaciology*, vol. 26, no. 94, pp. 225-233, 1980.

Etkins, R., and E. S. Epstein, The rise of global mean sea level as an indication of climate change, *Science*, vol. 215, pp. 287-289, 15 January 1982.

Fetterer, F. M., M. R. Drinkwater, K. C. Jezek, S. W. C. Laxon, R.G. Onstott, and L. M. H. Ulander, Sea ice altimetry, in *Microwave Remote Sensing of Sea Ice*, ed., F.D. Carsey (Washington DC, American Geophysical Union), Geophysical Monograph, vol. 68, pp. 111-135, 1992.

Forster, R. R., C. H. Davis, T. W. Rand, and R. K. Moore, Snow-stratification investigation on an Antarctic ice stream with an X-band radar system, *Journal of Glaciology*, vol. 37, no. 127, 1991.

Forster, R.R., K. C. Jezek, J. Bolzan, F. Baumgartner, and S. P. Gogineni, Relationships between radar backscatter and accumulation rates on the Greenland ice sheet, *International Journal of Remote Sensing*, vol. 20, no. 15, pp. 3131-3147, 1999.

Fujita, S., and S. Mae, Causes and nature of ice-sheet radio-echo internal reflections estimated from the dielectric properties of ice, *Annals of Glaciology*, vol. 20, pp. 80-86, 1994.

Fujita, S., H. Maeno, S. Uratsuka, T. Furukawa, S. Mae, Y. Fujii, and O. Watanabe, Nature of radio echo layering in the Antarctic ice sheet detected by a two-frequency experiment, *Journal of Geophysical Research*, vol. 104, no. B6, pp. 13,013-13,024, 1999.

Fujita, S., T. Matsuoka, T. Ishida, K. Matsuoka, and S. Mae, A summary of the complex dielectric permittivity of ice in the megahertz range and its application for radar sounding of polar ice sheets, in *Physics of Ice Core Records,* ed., by T. Hondoh, pp. 185-212, Hokkaido University Press, Sapporo, Japan, 2000.

Fung, A. K., and H. J. Eom, Coherent scattering of a spherical wave from an irregular surface, *IEEE Transactions on Antennas and Propagation*, vol. AP-31, no. 1, pp. 68-72, 1983.

Fung, A. K., *Microwave Scattering and Emission Models and Their Applications*, Artech House, Boston, 1994.

Gogineni, S., T. Chuah, C. Allen, K. Jezek, and R. K. Moore, An improved coherent radar depth sounder, *Journal of Glaciology*, vol. 44, no. 148, 1998.

Gross, G.W., I. C. Hayslip, and R. N. Hoy, Dielectric relaxation spectrum of ice measured with linear blocking electrodes, *Geophysics*, vol. 45, no. 5, pp. 914-927, 1980.

Gudmandsen, P., Layer echoes in polar ice sheets, *Journal of Glaciology*, vol. 15, no. 73, 1975.

Hammer, C. U., Past volcanism revealed by Greenland ice sheet impurities, *Nature*, vol. 270, pp. 482-486, 1977.

Hammer, C.U., Acidity of polar ice cores in relation to absolute dating, past volcanism, and radio-echoes, *Journal of Glaciology*, vol. 25, no. 93, pp. 359-372, 1980.

Harrison, C. H., Radio echo sounding of horizontal layers in ice, *Journal of Glaciology*, vol. 12, no. 66, pp. 383-397, 1973.

Henderson, B. C., Mixers: Part 1, characteristics and performance, *97-98 RF and Microwave Designer's Handbook*, pp. 469-475, Watkins-Johnson Company, Palo Alto, CA, 1997.

Herron, M. M., and C. C. Langway, Jr., Firn densification: An empirical model, *Journal of Glaciology*, vol. 25, no. 93, pp. 373-385, 1980.

Intergovernmental Panel on Climate Change (IPCC), Climate Change 2001: Impacts, Adaptation, and Vulnerability (Summary for Policy Makers), Geneva, Switzerland, February 13-16, 2001.

Izuka, K., A.P. Freundorfer, K.H. Wu, H. Mori, H. Ogura, and V.K. Nguyen, Step-frequency radar, *Journal of Applied Physics*, vol. 56, no. 9, pp. 2572-2583, 1984.

Kanagaratnam, P., S. Gogineni, N. Gundestrup, and L. Larsen, High-resolution radar mapping of internal layers at the North Greenland Ice Core Project, *Journal of Geophysical Research*, vol. 106, no. D24, pp. 33,799-33,812, 2001.

Kipfstuhl, S., Private communication, NGRIP, Greenland, 1998.

Kohler, J., J. Moore, M. Kennett, R. Engeset, and H. Elvehøy, Using ground-penetrating radar to image previous years' summer surfaces for mass-balance measurements, *Annals of Glaciology*, vol. 24, pp. 153-159, 1997.

Krabill, W., E. Frederick, S. Manizade, C. Martin, J. Sonntag, R. Swift, R. Thomas, W. Wright and J. Yungel, Rapid thinning of parts of the southern Greenland ice sheet, *Science*, vol. 283, pp. 1,522-1,524, 5 March 1999.

Krabill, W., W. Abdalati, E. Frederick, S. Manizade, C. Martin, J. Sonntag, R. Swift, R. Thomas, W. Wright, and J. Yungel, Greenland ice sheet: High-elevation balance and peripheral thinning, *Science*, vol. 289, pp. 428-430, 21 July 2000.

Larsen, L., Private communication, Lawrence, KS, 1999.

Lebedev, G. A., G. A., G. V. Trepov, and V. I. Poznyak, Results of radio-echo soundings of annual snow layer depth in Antarctica, *Proceedings of URSI Commission F*, Hyannisport, Massachusetts, 1990.

Leuschen, C., Surface-penetrating Radar for Mars Exploration, PhD. Dissertation, Electrical Engineering and Computer Science, The University of Kansas, Lawrence, KS, 2001.

Long, D. G., and M. R. Drinkwater, Greenland ice-sheet surface properties observed by the Seasat-A scatterometer at enhanced resolution, *Journal of Glaciology*, vol. 40, no. 135, pp. 213-230, 1994.

Looyenga, H., Dielectric constants of heterogeneous mixtures, *Physica*, vol. 31, pp. 401-406, 1965.

McConnell, J. R., G. Lamorey, E. Hanna, E. Mosley-Thompson, R. C. Bales, D. Belle-Oudry, and J. D. Kyne, Annual net snow accumulation over southern Greenland from 1975 to 1998, *Journal of Geophysical Research*, vol. 106, no. D24, pp. 33,827-33,838, 2001.

Millar, D. H. M., Radio-echo layering in polar ice sheets and past volcanic activity, *Nature*, vol. 292, 441-443, 1981.

Moore, J.C., and J. G. Paren, A new technique for dielectric logging of Antarctic ice cores, *Journal. de Physique.*, vol. 48, no. C1, pp. 155-160, 1987.

Moore, J. C., Dielectric variability of a 130 m Antarctic ice core: Implications for radar sounding, *Annals of Glaciology*, vol. 11, pp. 95-99, 1988.

Ohmura, A., and N. Reeh, New precipitation and accumulation maps for Greenland, *Journal of Glaciology*, vol. 37, no. 125, pp. 140-148, 1991.

Paren, J. G., and G. de Q. Robin, Internal Reflections in Polar Ice Sheets, *Journal of Glaciology*, vol. 14, no. 71, pp. 251-259, 1975.

Paterson, W.S.B., *The Physics of Glaciers*, Butterworth-Heinemann, Oxford, England, 1998.

Perry, T. S., Capturing climate change, *IEEE Spectrum*, vol. 39, no. 1, pp. 58-65, 2002.

Plummer, T. and B. Pharatasarathy, Target simulation for internal layers of Greenland ice sheet, IEEE student paper contest, Electrical Engineering and Computer Science, The University of Kansas, Lawrence, Kansas, 2002.

Richardson, C., E. Aarholt, S-E. Hamran, P. Holmlund, and E. Isaksson, Spatial distribution of snow in western Dronning Maud Land, East Antarctica, mapped by a ground-based snow radar, *Journal of Geophysical Research*, vol. 102, no. B9, pp. 20,343-20,353, 1997.

Ridley, J. K., and K. C. Partington, A model of satellite radar altimeter return from ice sheets, *International Journal of Remote Sensing*, vol. 9, no. 4, pp. 601-624, 1988

Robin, G. de Q., S. Evans, and J. T. Bailey, Interpretation of radio echo sounding in polar ice sheets, *Philosophical Transactions of the Royal Society of London, Series A, Mathematical and Physical Sciences*, vol. 265, no. 1166, pp. 437-505, 1969.

Robin, G. de Q., C. W. M. Swithinbank, and B. M. E. Smith, Radio echo exploration of the Antarctic ice sheet, *International Association of Scientific Hydrology*, no. 86, pp. 97-115, 1970.

Robin, G. de Q., and D. H. M. Millar, Flow of ice sheets in the vicinity of subglacial peaks, *Annals of Glaciology*, vol. 3, pp. 290-294, 1982.

Robin, G. de Q., Radio-echo studies of internal layering of polar ice sheets, in *The Climatic Record in Polar Ice Sheets*, ed., G. de Q. Robin, pp. 89-93, Cambridge University Press, Cambridge, England, 1983.

Robinson, E. A., and S. Treitel, *Geophysical Signal Analysis*, Prentice Hall, Englewood Cliffs, NJ, 1980.

Saunders, W. K., CW and FM radar, in *Radar Handbook*, 2nd ed., M. I. Skolnik, ch. 14, McGraw-Hill, New York, 1990.

Saxton, J. A., Reflection coefficient of snow and ice at V.H.F., *Wireless Engineer*, vol. 27, no. 316, pp. 17-25, 1950.

Steyskal, H., Digital beamforming antennas, *Microwave Journal*, pp. 107-122, January 1987.

Stove, A. G., Linear FMCW radar techniques, *IEE Proceedings-F*, vol. 139, no. 5, pp. 343-350, 1992.

Thomas, R. H., Polar Research from Satellites, Joint Oceanographic Institutions, Inc., Washington DC, 1991.

Ulaby, F.T., R. K. Moore, and A. K. Fung, *Microwave Remote Sensing: Active and Passive,* vol. 2, Artech House, Norwood, MA, 1986.

van der Veen, C. J., and J.F. Bolzan, Interannual variability in net accumulation on the Greenland Ice Sheet: Observations and implications for mass balance measurements. *Journal of Geophysical Research,* vol. 104, no. D2, pp. 2009-2014, 1999.

van der Veen, C.J., Polar ice sheets and global sea level: how well can we predict the future?, in press, *Global and Planetary Change,* 2002.

Vickers, R. S., and G. C. Rose, High resolution measurements of snowpack stratigraphy using a short pulse radar, *Proceedings of the Eighth International Symposium on Remote Sensing of Environment*, vol. 1, pp. 261-267, Ann Arbor, Michigan, October 2-6, 1972.

Waite, A. H., Ice depth soundings with ultra-high frequency radio waves in the Arctic and Antarctic, and some observed over-ice altimeter errors, *U.S. Army Signal Research and Development Laboratory*, Technical Report 2092, 1959.

Wehner, D. R., *High-resolution Radar 2nd ed.*, Artech House, Norwood, MA, 1995.

Wong, W., Private communication, Lawrence, KS, 2001.